Influence Of Accretion Disk Size
On
Spectral And Timing Properties
Of
Stellar Mass Black Holes

Thesis
submitted for the degree of
Doctor of Philosophy (Sc.)
in
Physics (Theoretical)

by

Arindam Ghosh

Department of Physics
University of Calcutta
2019

to

my ailing father

and
my only sister

Acknowledgements

I am grateful to my Mentor and Thesis Supervisor, Professor Sandip Kumar Chakrabarti, for giving me fantastic and generic problems to ponder with a reasonable liberty. Without his continuous advises and revisions this Thesis could not have converged to a concise form.

I am indebted to the archives, `https://exoplanetarchive.ipac.caltech.edu`, `http://xte.mit.edu/asmlc/ASM.html` and `http://swift.gsfc.nasa.gov/results/transients/BlackHoles.html`, for public X-ray data and facilities furnished by NASA. The quick-look results provided by the ASM/RXTE team and Swift/BAT transient monitor results provided by the Swift/BAT team have been very much useful in extracting many interesting scientific findings which are discussed here.

During the tenure of my doctoral research, I learnt many things from several researchers, namely, Dr. Partha Sarathi Pal, Dr. Broja Gopal Dutta, Dr. Arnab Deb, Dr. Soumyakanti Bose, Dr. Suman Dutta, Dr. Ayan Bhattacharjee, Mr. Anuvab Banerjee and Mr. Prantik Nandi. I must thank Prof. A. R. Rao (TIFR, Mumbai), Dr. Anuj Nandi (ISRO, Bengaluru) and Dr. Dipak Debnath (ICSP, Kolkata) for similar reasons. In particular, I am beholden to Soumyakanti for always being there as a consistent friend.

I am indebted to Dr. Soumen Mondal and Dr. Ramkrishna Das, the faculty members in the Department of Astrophysics & Cosmology, S. N. Bose National Centre for Basic Sciences (SNBNCBS), where I pursued my doctoral research. Several long-time friends have inspired me constantly with strong encouragement and mental support during my crisis periods. A few of them are: Prof. Anindya Datta (Indraprastha University, New Delhi), Dr. Suparna Das (Central European University, Budapest), Dr. Anupam Mukherjee (Spring&River Technology Pvt. Ltd., Kolkata) and Dr. Sanmitra Ghosh (Jadavpur University, Kolkata). Finally, I am grateful to Mr. Milon Mukherjee, a renowned lawyer, Calcutta High Court, for his altruistic role in my life.

Abstract

When the massive component of a binary star system evolves faster and becomes a black hole, tidally deformed companion star often overflows through its Roche lobe to the primary. Some low angular momentum winds also take part in this journey. This gaseous flow encircles the compact primary and eventually accretes to it due to presence of viscosity in the differentially rotating flow. Conversion of gravitational energy release to thermal energy, along with viscous dissipation raises the temperature of the inflow enabling it to emit X-rays. There are two processes to emit X-rays. A geometrically thin Keplerian disk with high angular momentum and high viscosity radiates low energy (or soft) photons in a multi-colour black body distribution, whereas a geometrically thick sub-Keplerian halo (a region surrounding the disk vertically) having low angular momentum and low viscosity produces high-energy (or hard) photons obeying a power-law behaviour in their spectra due to repeated Compton scatterings. This is the paradigm of Two-Component Advective Flow (TCAF), theoretically established by Chakrabarti (1995, 1996). When the hot halo slows down close to the black hole due to its centrifugal barrier, a sudden reduction of radial kinetic energy results in heat which puffs up this flow. In TCAF paradigm, this CENtrifugal pressure supported BOundary Layer (CENBOL) represents the Compton cloud and converts soft photons into hard photons.

In high-mass X-ray binaries (HMXRBs), the basic way of accretion is wind-feeding; the predominant sub-Keplerian flow is nearly in-viscid, and the size of the Keplerian accretion disk is small. However, in low-mass X-ray binaries (LMXRBs), highly viscous and bigger accretion disk is formed due to Roche lobe overflow of matter from the companion star. In this scenario, a difference in time is expected between the two flow components on their arrival at the black hole in a XRB. This *arrival time lag* or *delay* (τ) is more likely to be prominent in LMXRBs than in HMXRBs. Satellite X-ray data of about a dozen of XRBs, which exhibit transience, persistence and class-variability in the lightcurves, are considered for a generic analysis in order to establish that the two flow components arrive at different times. The variation of the Keplerian disk size in different XRBs and also at different times in the same XRB is the cynosure.

In order to quantify τ, we have introduced a dynamic photon index (DPI, designated by Θ) which responds to both soft and hard fluxes of photon or energy. When cross-correlated with reference to Θ, these two radiative components are shown to be separated by a few days to a few weeks during the outbursts in LMXRBs. However, this time lag is negligibly small ($\tau \sim 0\ d$) in a HMXRB and also during its outburst-like flaring phases. Moreover, a longer delay ($\tau \gg 0\ d$) can be directly estimated from the behaviour of Θ with time. Such evidences directly confirm the existence of two accretion flow components as discussed in the TCAF theory. By virtue of its definition ($|\Theta| < 1.57$), Θ acts as a universal spectro-temporal parameter of reference for all XRBs by rescaling the usual power-law photon index (Γ) and the Comptonizing efficiency (CE). It follows a characteristic curve during outbursts and distinguishes their four spectral states both qualitatively and quantitatively. With Θ and TCAF in hand, we have analyzed 18 outbursts in 6 transient LMXRBs so as to classify all normal outbursts into two categories, based on the difference in several salient features, and identify anomalies of various degrees in other outbursts.

Since the Keplerian accretion disk size is most likely to be proportional to τ, LMXRBs and HMXRBs form large and very small disks respectively. Therefore, an orbital modulation due to the tidal effect is observed prominently from a distinct peak in the Fourier spectrum of the long-term lightcurve of a HMXRB, whereas, such a peak in a LMXRB is shown to be weak due to viscous effects in its large Keplerian disk.

Publications

- **Arindam Ghosh** and Sandip K. Chakrabarti ★ *Anomalous Outbursts of H 1743-322* MNRAS 485 4045 **(2019)**
- **Arindam Ghosh**, Indrani Banerjee and Sandip K. Chakrabarti ★ *Does Cyg X-1 have a small Accretion Disc?* MNRAS 484 5802 **(2019)**
- **Arindam Ghosh** and Sandip K. Chakrabarti ★ *Signature of Two-Component Advective Flow in several Black Hole candidates obtained through time-of-arrival analysis of RXTE/ASM Data* MNRAS 479 1210 **(2018)**
- **Arindam Ghosh** ★ *A Dynamic Photon Index Probes into TCAF* in Mukhopadhyay B., Sasmal S., eds, Exploring the Universe: From Near Space to Extra-Galactic, Astrophysics and Space Science Proceedings, Vol. 53, Ch. 24, p. 311, *Springer*, Cham, Switzerland **(2018)**
- **Arindam Ghosh** and Sandip K. Chakrabarti ★ *Smearing of mass accretion rate variation by viscous processes in accretion disks in compact binary systems* Ap&SS 361:310 **(2016)**

Contents

List of Figures

List of Tables

Chapter 1

Introduction

Compact objects, such as, white dwarfs (WDs), neutron stars (NSs) and black holes (BHs) are the remnants of stars which underwent stellar evolution when most of the matter or fuel (hydrogen or helium gas) of the progenitors was already expended. In general, the compact objects differ from the ordinary stars in the following fundamental way: they are devoid of any nuclear fuel to burn. Consequently, they cannot support themselves against gravitational collapse by generating thermal pressure and a contraction follows. The key factor which determines the nature of the end product or the dead star (WD, NS, and BH) is the mass of the progenitor. WDs are believed to be originated from stars having low mass ($M_\star \leq 4M_\odot$, where, $M_\odot$ is the solar mass) in which the internal pressure support is provided by the degenerate electron gas. A WD has a maximum mass of $\sim 1.4M_\odot$ (Chandrasekhar limit), beyond which the pressure of the electrons is no longer able to balance gravity, and the star continues to contract, eventually forming either a *neutron star* (NS) or a *black hole* (BH). If an evolved star, due to gravitational collapse, becomes so compressed that within the star itself electrons are forced into atomic nuclei and combine with protons to form neutrons, then it becomes a NS. The current model of a NS envisages that it has a gaseous surface a few metres thick below which there is a solid crust some 1 *km* in depth. Underlying this *hard surface* a superfluid layer consisting almost exclusively of neutrons is thought to be present. At the centre of a NS there is a hard core. A typical NS is about ≤ 10 *km* in diameter but has a mass of $\geq 1.5M_\odot$. NSs in binaries are commonly called pulsars when they rotate rapidly and have strong magnetic fields.

BHs are thought to originate from supernovae explosions in which the core mass left after the explosion is very large (several solar masses). It then continues to contract and a very strong gravitational field is produced. Eventually it reaches a point at which the field is large enough to prevent electromagnetic radiation leaving the object. The object is said to have become a BH. The boundary radius where the gravitational field reaches the critical value is the *event* *horizon*, and it is not possible to communicate with matter inside this boundary. This is why, observational evidence of objects thought to be BHs comes from their effects on surrounding matter. If a BH forms in a binary system, it will attract and capture (i.e., accrete) matter from this companion. The material carrying high angular momentum leaves the companion star and forms a rotating (accretion) disk around the BH, in which the matter becomes compressed and heated to such an extent that it emits X-rays, which are detected from the earth. In the Cygnus constellation there is an X-ray source, Cyg X-1, which consists of a supergiant star revolving around a small invisible orbital component with a mass $> 10M_\odot$, which was first designated to be a BH about half a century ago. About one-third of all the stars in our vicinity may likely belong to binary systems. In a black hole binary (BHB) system, the X-rays produced by the matter falling into the BH from the companion star releasing gravitational potential energy are the main observational perspective. Any astronomical source of X-radiation from outside the solar system is called an X-ray source (XRS). More than a hundred sources within our Galaxy have been observed as objects which emit most of their energy in the X-ray region of the electromagnetic spectrum and only a relatively small proportion of their energy is in the visible spectrum. Many of these XRSs appear to be members of binary systems consisting of one primarily visual star and one X-ray star gravitationally bound together. Such a system is called X-ray binary (XRB). Owing to the absorption of X-rays by the earth's atmosphere these XRBs are only visible by X-ray telescopes carried by space probes and satellites, though some high-energy X-rays can penetrate the upper atmosphere and are detectable by X-ray telescopes mounted on balloons.

XRBs have two basic categories, viz. low mass X-ray Binary (LMXRB) and high mass X-ray binary (HMXRB), depending on the mass of the donor or companion star. If $M_\bullet$ and $M_\star$ are respectively the compact and companion masses, then in HMXRBs, $M_\bullet < M_\star$ with $M_\bullet \sim 10M_\odot$ & $M_\star \sim 10M_\odot$, while in LMXRBs, $M_\bullet > M_\star$ with $M_\bullet \sim 10M_\odot$ & $M_\star \sim 1M_\odot$.

XRBs are the best systems to look for BHs. However, not all XRBs contain BHs. In order to prove that the compact object is a BH, one has to show that the radius of the object is smaller than its event horizon. This is difficult to do with direct imaging, even though in current years photon spheres (1.5 times the event horizon, for a non-rotating BH) of a gigantic BH, namely, M87, has been detected. The best indirect method is to determine its mass. Although some uncertainty lies in the equation of state of a NS and other factors such as spin, inclination angle, etc. but it is theoretically established that $3M_\odot$ is a safe upper limit for the mass of a NS. Therefore, an estimation of the mass $M_\bullet > 3M_\odot$ ensures a BH. There are also some other observational characteristics, viz. characteristic X-ray spectrum, variability up to $\mathscr{O}[100\ Hz]$, quasi-periodic oscillations (QPOs) in 100 $mHz - 450\ Hz$ range, the variability dependent on spectral stateS, by which the compact object can be believed to be a BH. BH mergers are postulated to be the cause of gravitational waves which are currently becoming an important probe for a direct detection and imaging of the BHs.

The theoretical study of BHs involves the use of general relativity. One problem is the fate of matter within the event horizon, which is supposed to be compressed to a single point (a *singularity*) of infinite density located at the centre of the event horizon. It has been shown that a BH can be characterized uniquely by three properties: its mass, angular momentum (spin) and electrical charge. Mathematical expressions have been derived for describing spacetime around BHs. These are the Schwarzschild solution (uncharged non-rotating BHs), the Reissner-Nordstrom solution (charged non-rotating BHs), the Kerr solution (uncharged rotating BHs), and the Kerr-Newman solution (charged rotating BHs). According to the prediction of general relativity, there is a singularity at the centre of a BH where the density of matter becomes infinite and the laws of physics break down. However, as the singularity is hidden within the event horizon, it cannot influence the outside universe, so the classical laws of physics can be used to describe processes outside the BH.

1.1 Stellar Mass Black Holes

A stellar mass black hole is a compact object in space that has collapsed under its own gravitational forces to such an extent that its escape velocity is the speed of light. As stated earlier, if the mass of an evolved stellar core is well above the Chandrasekhar limit (1.4 $M_\odot$) for a WD then neutron degeneracy pressure is unable to prevent contraction until the gravitational field is sufficiently strong to prevent the escape of electromagnetic radiation. The boundary of the BH, i.e. the event horizon, is the spherical surface in space of a particular radius at which the gravitational field reaches its critical value. This critical radius is called the Schwarzschild radius $r_g = 2GM_\bullet/c^2$, where G is the gravitational constant, c is the speed of light and $M_\bullet$ is the BH mass. So, if the star collapses to such an extent that its radius is less than r_g (radius of the event horizon) the escape velocity becomes equal to the speed of light and the star becomes a BH. Events occurring within this horizon (i.e., in the interior of the BH or at $r < r_g$) cannot be observed from outside. However, the physical processes away from the event horizon of a Schwarzschild BH can be satisfactorily described by a pseudo-Newtonian potential given by (Paczyński & Wiita 1980),

$$V(r) = -\frac{GM_\bullet}{r - r_g}, \tag{1.1}$$

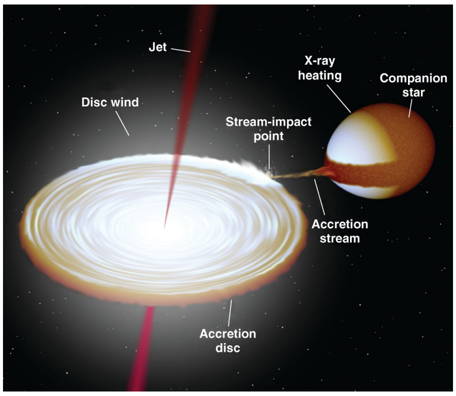

Figure 1.1: Formation of accretion disk around a BH due to the flow of stellar matter from its companion star is schematically shown. Angular momentum of matter prohibits a direct free-fall (Credit: NASA/R. Hynes).

although all the respective flow components have the same behaviour when studied in full general relativity. For a typical BH of mass $M_\bullet = 10M_\odot$ in an XRB, $r_g \simeq 30\ km$. Stellar-mass BHs (with a typical mass of $M_\bullet \sim 10M_\odot$) are known to exist in many XRBs in the Milky Way and many more BH candidates with $M_\bullet \simeq 3M_\odot - \mathscr{O}[10M_\odot]$ are thought to be representative of a very large population of about $10^8 - 10^9$ BHs in the Galaxy. They are observed as members of XRBs consisting of BHs.

The stellar mass BHs studied in this Thesis are known by the following astronomical names: Cyg X-1 & Cyg X-3 (HMXRBs); GX 339–4, H 1743–322, GRS 1915+105, XTE J1650–500, XTE J1550–564, 4U 1543–47, GRO J1655–40, GRS 1758–258, 1E 1740.7–2942 & H 1705–25 (LMXRBs).

1.2 Accretion onto a Black Hole

The simplest possible accretion scenario involves a spherically symmetric steady flow of matter onto a central object from its surrounding interstellar medium. This is known as the *Bondi flow* (Bondi 1952), where the relative cross-radial motion between the central object and the radial accretion flow is negligible. The angular momentum and magnetic field of the accreted medium may also be neglected in such an ideal flow (Chakrabarti 1990). It is further assumed that the viscosity does not play any role in accreting matter and the mass accretion rate is constant throughout the flow. If such a radial accretion flow is considered for any BH, the flow velocity reaches the speed of light at the horizon with vanishing density. Since higher velocity means lower density in a spherical flow, the emitted radiation is weak and high quasar luminosity cannot be explained by this type of flow.

Accretion in an XRB is a process by which matter settles around a central compact object (primary) as illustrated in Fig. 1.1. For a LMXRB, the lighter companion star (secondary) is tidally deformed and reaches the giant state overflowing its Roche lobe, the boundary within which the material is bound by its gravity, as schematically represented in Figs. 1.2 & 1.3

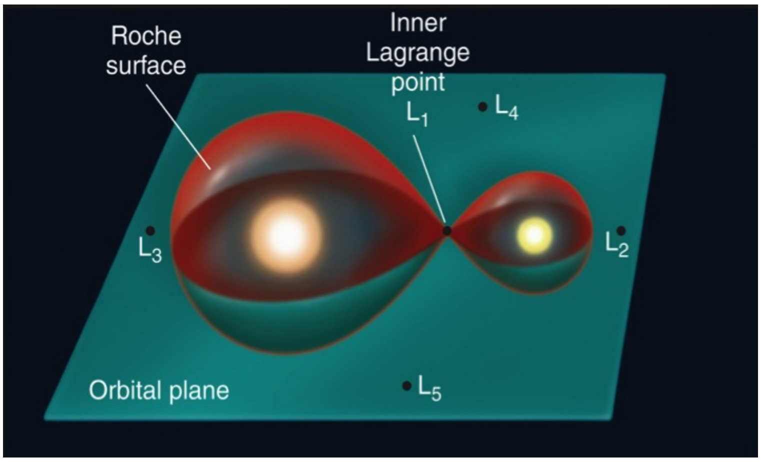

Figure 1.2: Roche lobe configuration of equipotential surfaces (*figure-of-eight*) of a binary star system is shown schematically. L_1 is the inner Lagrange point of contact between the potential surfaces of two stars. Matter can flow through this point. For LMXRBs, where one star is a BH, this is the main way of accretion. Matter can most easily leave the system in the form of winds from L_2 and L_3, the Lagrange points on the opposite sides of the primary and the secondary stars. For HMXRBs, these winds are mainly the source of accretion to a BH. L_4 and L_5 are the Lagrange points, which are at right angles to the line joining the binary, form equilateral triangles with the centres of the stars (Credit: NASA/R. Hynes).

(see captions for details). The gas flows from the companion star toward the central object. Angular momentum conservation prevents a straight radial flow, an accretion disk is formed instead. The matter carries high angular momentum and, after leaving the companion star, spirals around the BH in Keplerian orbits and forms a rotating accretion disk due to viscosity (Fig. 1.1). Gravity causes diffuse matter in the disk to spiral towards the BH while the matter in the accretion disk is in a perfect equilibrium between the gravity and the centrifugal force. Gravitational and viscous forces compress and raise the temperature of the settled matter to such an extent that it emits electromagnetic radiation in the X-ray part of the spectrum. On the other hand, similarly formed accretion disks of normal stars radiate in the infrared (IR), while those around NSs radiate in the X-rays and γ-rays. However, in a HMXRB, the accretion disk is formed around the BH primarily due the stellar winds of the heavier companion star, as depicted in Fig. 1.3.

1.2.1 Energy due to Accretion

On its way to the BH, accreted matter loses its potential energy and angular momentum and radiates more efficiently. The efficiency of this radiation can rise to 6% of the rest mass of

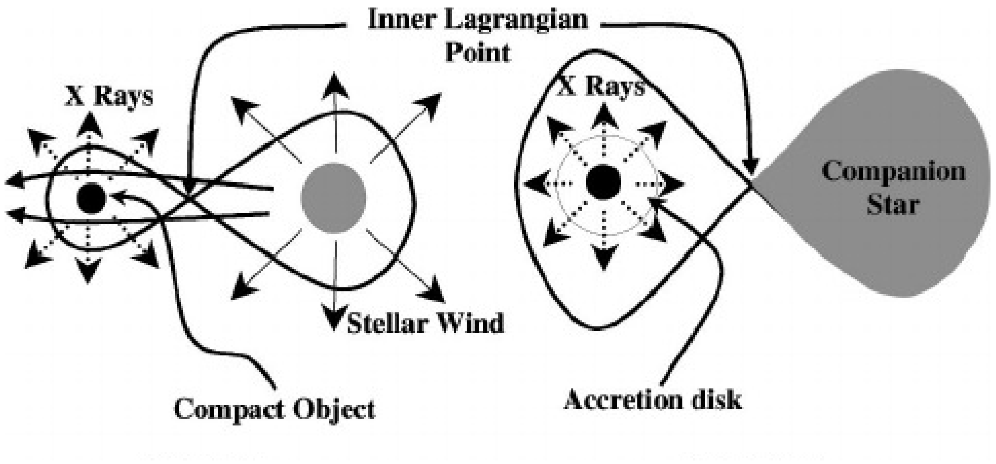

Figure 1.3: Primary way of accretion in a HMXRB (left) is wind-feeding while that for an LMXRB (right) is due to Roche lobe overflow from the companion star (Credit: Moret et al. 2003).

the infalling matter for a Schwarzschild BH while up to 40% for a Kerr BH (depending upon its spin parameter). However, the actual efficiency depends on quantities such as viscosity and the cooling processes inside the disk. This energy is released in the entire electromagnetic spectrum and the success of a disk model depends on its ability to describe the way this energy is distributed in various energy bands. The temperature distribution, the density distribution and the disk geometry determine the overall nature of the resulting spectrum. The outer boundary conditions, viz. the specific angular momentum, the energy and the rate of infalling matter also influence the radiation properties significantly.

The extraction of gravitational potential energy from accreting matter is known to be the main source of power in many types of luminous astrophysical sources. For a body of mass M and radius R, the gravitational energy released by the accretion of a mass Δm onto its surface is $\Delta E_{acc} = \frac{GM\Delta m}{R}$ and most of it is expected to be released in the form of electromagnetic radiation. The luminosity produced by the accretion process is $L_{acc} = \frac{GM\dot{m}}{R} \simeq \eta\dot{m}c^2$, where η is the efficiency for converting the rest mass energy into radiation and $\dot{m}$ is the accretion rate (the mass accreted per unit time). If matter could be accreted onto a BH infinitesimally slowly, $\eta = 1$, which is obviously an unrealistic assumption. However, the current consensus is that, for typical accreting BHs, $\eta \sim 0.1$, i.e. the efficiency is about 10%. This can be compared with the rest mass to energy efficiency of nuclear fusion of H into He which is only $\eta = 0.007$, i.e. less than 1%. It is therefore apparent that the accretion around BHs is the most efficient way to convert rest mass into luminosity and the mechanism is indeed widely believed to power among the most luminous sources of radiation in the universe. A BHB comprising a BH and a normal star may act as an XRS due only to the accretion process. Such a BH can be detected by the analysis of information carried by the X-rays emitted.

However, there is a limit on the luminosity that can be extracted from accretion. For simplicity, we consider a spherically symmetric accretion process in which the accreting matter is mainly fully ionized hydrogen (a good approximation in reality). The radiation produced through the accretion mechanism gives rise to radiation pressure which acts as a repulsive force on the free electrons via Thomson scattering. The attractive electrostatic Coulomb force means that the free electrons, which are repelled from the compact object and effectively stop accreting, will drag the protons with them. The radiation pressure pushes away the electron-proton pairs against the gravitational interaction which is responsible for the accretion process. If the luminosity of the accretion mechanism is such that the force on the electron–proton pairs is greater than the gravitational one, accretion stops altogether and we have rather an outflow of matter driven by radiation pressure. This balance sets the limit of maximum luminosity that can be extracted due to accretion. This is called the Eddington luminosity, which is defined by

$$L_{Edd} = \frac{4\pi G M_{\bullet} m_p c}{\sigma_T} \simeq 1.3 \times 10^{38} \, \frac{M_{\bullet}}{M_{\odot}} \, erg \; s^{-1}, \tag{1.2}$$

where $M_{\bullet}$ is the BH mass, m_p is the proton mass, and σ_T is the Thomson cross-section. The luminosity of the Sun is

$$L_{\odot} = 3.828 \times 10^{33} \; erg \; s^{-1} \simeq 4 \times 10^{26} \; W. \tag{1.3}$$

This means that

$$L_{Edd} \simeq 3 \times 10^{4} \, \frac{M_{\bullet}}{M_{\odot}} L_{\odot}. \tag{1.4}$$

So, accretion potentially provides almost four orders of magnitude more power than the nuclear reactions occurring in the Sun for a BH of the same mass.

Although the assumption of spherical accretion and isotropic radiating source fails in an accretion disk, which takes in matter along an equatorial plane, and radiates preferentially in directions perpendicular to that plane, but the Eddington limit is considered to be a useful benchmark even for non-spherical accreting systems. Moreover, objects of a given mass can have higher luminosity (e.g., nova and supernova), but then an outflow of material is unavoidable. Because of non-sphericity, an exact application of Eddington limit is not possible, and it is known that the disks may in fact emit super-Eddington luminosity without being disrupted.

1.2.2 Accretion Disks

Accretion disks are the basic and fundamental structures which are formed around the central objects when matter is collected from the companion. These are supposed to be geometrically thin structures orbiting the central BH (or, other compact objects like NS) which allow the accreting matter to lose its angular momentum and therefore to be accreted. Since circular orbits have the least energy for a given angular momentum, the gas slowly spirals inwards through a series of (approximately circular) Keplerian orbits (Fig. 1.1) transferring angular momentum outwards.

The binding energy of a gas element of mass Δm in a Keplerian orbit grazing the surface of the compact accretor (of size R) is $GM_\bullet \Delta m/2R$. As the mass element starts its spiral motion at large distances with negligible binding energy, the total luminosity of a disk (in a steady state) must be $L_{disk} = GM_\bullet \dot{m}/2R$ which is half of the available energy. In other words, an accretion disk acts as an efficient machine in the gravitational potential well of the central compact object for extracting large amount of energy. This process partially converts the orbital kinetic energy into heat which gives rise to radiation. Keplerian rotation implies differential rotation, i.e., matter at different neighbouring radii moves with a different angular velocity since

$$\omega_K(r) = \sqrt{\frac{GM_\bullet}{r^3}}. \tag{1.5}$$

Due to the presence of chaotic thermal or turbulent motions, viscous stresses are generated in the disk. As a consequence, there is a local loss of mechanical energy dissipating into internal heat.

The standard theory of disk accretion was first formulated by Shakura & Sunyaev (1973) and the disk model is known as *SS73 disk*. The model considers a geometrically thin gaseous disk flow executing Keplerian motion around the BH. Pressure supports the disk against the vertical component of gravity. Viscous torque acting on different annuli of the disk results in a loss of angular momentum. The accreting matter, shredding angular momentum gradually, spirals towards the BH. This torque ($\Gamma_{r\phi}$) is responsible for transporting the angular momentum outwards and thus making the accretion possible and is assumed to be proportional to the total vertically averaged pressure of the gas in the disk, p_{av}, i.e.,

$$\Gamma_{r\phi} = \alpha_{SS}\ p_{av}, \tag{1.6}$$

where, $\alpha_{SS} < 1$ is known as the viscosity parameter. The angular momentum distribution of matter is purely Keplerian. Thus, the radial velocity (v_r) is negligible compared to the orbital velocity, v_ϕ. Therefore, the Keplerian orbital velocity is

$$v_\phi = r\omega_K(r) = \sqrt{\frac{GM_\bullet}{r}}. \tag{1.7}$$

However, in presence of a significant viscosity, the gas is assumed to possess a small inward radial drift velocity v_r enabling the matter to be accreted. In the absence of pressure, the angular momentum of the gas element at the same radius r is obtained as

$$\lambda_K = \sqrt{GM_\bullet r}. \tag{1.8}$$

For a steady-state disk, the total luminosity radiated away from the accretion disk due to viscous dissipation is given by

$$L_{disk} = \frac{GM_\bullet \dot{m}}{2r_{in}} = \frac{1}{2}L_{acc}, \tag{1.9}$$

where, r_{in} is the boundary of the inner edge of the disk away from the BH at the centre. Therefore, 50% of the gravitational energy is radiated away from the accretion disk. The drawback of this model is that the disk is terminated at the marginally stable orbit of radius $r_{ms} = 3\ r_g$ with angular momentum $\lambda_{ms} = 1.8\ (\frac{2GM_\bullet}{c})$ and the inner boundary condition on the horizon cannot be applied. However, this disk model gives an insight that matter has to deviate from the Keplerian orbit to maintain the inner boundary conditions.

If the disk is optically thick, each element of the disk radiates roughly as a black body and the emitted spectrum will be the superposition of black bodies with temperature T(r) emitted from a narrow annulus at r and integrated over the whole disk surface. The maximum temperature achieved in a standard accretion disk around a BH can be expressed as a function of total emitted luminosity (L_{disk}):

$$T(r) \simeq 1.1 \times 10^8 \left(\frac{L_{disk}}{L_{Edd}}\frac{M_\odot}{M}\right)^{1/4} \left(\frac{2r}{r_g}\right)^{-3/4} K. \tag{1.10}$$

Thus, the overall radiation from such a disk exhibits a multi-colour black body spectrum, which is the sum of spectra of black bodies with a radial temperature distribution of $T(r) \sim r^{-3/4}$. The maximum temperature is clearly reached for the smallest radius, i.e., at the inner edge r_{in} of the accretion disk. This is generally assumed to coincide with the *innermost stable circular orbit* (ISCO) around the BH, beyond which matter plunges into the event horizon ballistically. The ISCO radius is $r_{ISCO} = r_{ms} = 3\ r_g$ for a non–rotating Schwarzschild BH.

1.2.3 X-ray Emission from Accretion Disks

The radiation from the accreting matter is mostly dominated in X-ray wavelengths ($0.01 - 10\ nm$, corresponding to $10^{16} - 10^{19}\ Hz$ frequency range or $100\ eV - \mathscr{O}(100\ keV)$ energy range). The energy distribution is the sum of emission from a large population of particles undergoing a series of transition among energy levels with different electric or magnetic moments. These energy levels are either discrete or continuous and determine the shape of the observed spectra. A continuum emission of X-rays can be either thermal or non-thermal. Thermal radiation is emitted by matter in thermodynamic equilibrium when the medium particles follow the

Maxwell-Boltzmann statistical distribution; *non-thermal* radiation is emitted otherwise. Thermal emission mechanism can be distinguished as black body radiation, bremsstrahlung, line emission, and Comptonization. Non-thermal emission, such as non-thermal Comptonization, cyclotron radiation, synchrotron radiation, etc. is important in an environment consisting of high-energy particles. However, in this Thesis, we are interested in X-rays which originate from the following two radiative processes:

Black body radiation: This arises from an optically thick medium in thermodynamic equilibrium (i.e., when the photons have an equilibrium energy distribution corresponding to the same temperature). This ensures that the population (atomic, ionic or molecular) of all excited states in the system is given by Saha-Boltzmann statistics. The emitted radiation from the medium follows Planck distribution. For BHs, most of the black body radiation is emitted from the hot and optically thick plasmas of the accretion disk and is observed as continuous energy spectra.

Comptonization: In Compton scattering process, a high-energy photon encounters an electron and transfers its partial energy to the electron. Conversely, a high-energy electron can also transfer its energy partially to a low-energy photon. This inverse Compton scattering is a very efficient radiative process for generating high-energy photons in the accretion flow. If a similar interaction takes place between ensembles of photons and electrons then the energy distribution of both the photons and electrons will be modified. This process is known as the Comptonization. It is observed that the high-energy spectrum ($\geq 10\ keV$) of a typical BH system in hard states obeys a power law, which is purely a characteristic of the Comptonization process. However, with the presence of non-thermal electrons in the plasma, the process of Comptonization will be modified with respect to the thermal case. The effect of non-thermal electrons on Comptonization will produce a high-energy tail that is well above the thermal cut-off at $\sim 400\ keV$. The high-energy tail arises from the superposition of individual spectra of non-thermal electrons.

1.2.4 Photon Index (Γ) and Spectral State Transition

The accretion disk thermal spectrum is not the only component in the observed spectra from accreting BHs. In particular, a power-law spectral component is omnipresent in the X-ray spectra of BHBs. If the photon flux per unit energy i.e., $photons\ cm^{-2}s^{-1}keV^{-1}$, is described in the form of a power law,

$$f(E) \propto E^{-\Gamma}, \tag{1.11}$$

the spectrum is said to have a power-law form with photon index or slope Γ. The typical thermal emission $\sim 1\ keV$ is usually observed when the source is bright. Here, the proportionality constant gives the normalization N ($photons\ keV^{-1}cm^{-2}s^{-1}$ at 1 keV) are the two parameters of the model. Historically, this is called a soft state (SS) or a high state for which $\Gamma > 2$. On the contrary, a hard state (HS) or a low state, with a photon index $\Gamma < 2$, is generally observed when the source is faint. A SS is observed with a high luminosity $> L_{Edd}$ and the corresponding spectrum comprises both thermal component and power-law component often steeper ($\Gamma \sim 2.5$) than the hard power-law. These two spectral states are shown in Fig. 1.4. In the next section, we briefly discuss the theoretical perspective of the origin of these two radiative components.

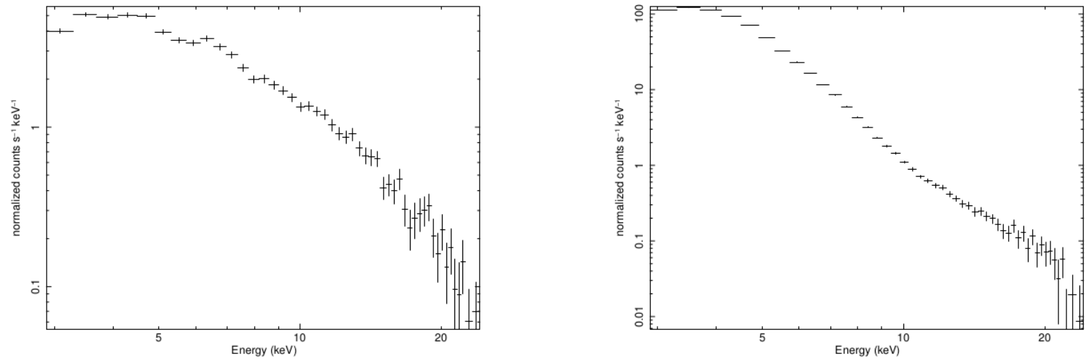

Figure 1.4: Typical X-ray spectra of a BHB system showing a black body continuum (left) in the SS ($\Gamma > 2$) followed by a power-law tail (right) in the HS ($\Gamma < 2$).

1.3 Two-Component Advective Flow (TCAF)

The standard accretion disk (or SS73 disk) is an optically thick but geometrically thin Keplerian flow, which dissipates gravitational energy through viscosity and radiates multi-colour black body (soft) X-ray photons. Another mechanism behind the X-ray emission from accretion disks around BHs is though a hot electron cloud, i.e., the Compton cloud. This intercepts soft photons from the Keplerian disk and emits non-thermal X-ray photons obeying a power law in the spectra. Several models, available in the literature, which use a hot electron cloud or a *static corona* in order to produce the power law component of the spectrum (Sunyaev & Titarchuk 1980, 1985; Zdziarski 1988; Haardt & Maraschi 1993; Haardt et al. 1994; Meyer & Meyer-Hofmeister 1994; Narayan & Yi 1994; Liu et al. 1999, 2002; Meyer et al. 2000; Taam et al. 2008; Zhang et al. 2009; Poutanen et al. 2018). Such models make various assumptions about the disk and the corona and often successfully explain specific observational aspects. In the Two Component Advective Flow (TCAF) solution, which is a self-consistent

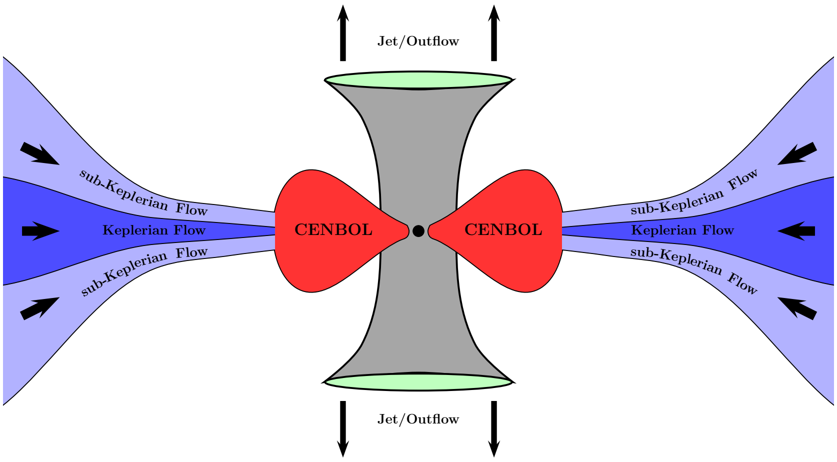

Figure 1.5: TCAF paradigm: A geometrically thin viscous Keplerian disk with high angular momentum and high opacity radiates multi-colour black body (or soft) photons, whereas a geometrically thick sub-Keplerian advective halo having low angular momentum (i.e. $\lambda < \lambda_K$, the Keplerian angular momentum) and low opacity produces outflows and winds along with high-energy (hard) photons representing a power law behaviour in the spectrum due to repeated inverse Compton scatterings from the CENBOL (Compton cloud). Nearly inviscid halo travels inwards in free-fall timescale (t_{ff}), whereas the Keplerian disk component flowing in viscous timescale ($t_{vis} > t_{ff}$) reaches the CENBOL much later. Before entering the BH (at the centre of Fig. 1.5), the flow has to be supersonic so as to pass through at least one sonic point (Mach number $M = \frac{v_{flow}}{v_{sound}} = 1$). The post-shock flow rushes into the BH in infall timescale ($t_{in} \ll t_{vis} \sim \frac{t_{ff}}{\alpha_{SS}}$, where α_{SS}=*SS73* viscosity parameter). A possible shock may oscillate, depending on the physical parameters, giving rise to QPOs (adopted from Chakrabarti & Titarchuk 1995).

theoretical paradigm resulted from the works of Chakrabarti (1995, 1996) and Chakrabarti & Titarchuk (1995, or CT95), the latter component is the result of a relatively hotter, optically thin but geometrically thick, sub-Keplerian halo which sandwiches the Keplerian disk and dissipates its potential energy through repeated inverse Comptonization. In TCAF paradigm, the two flow components are due to differential viscosity in the vertical direction. Equatorial regions with viscosity parameter higher than the critical values will form a Keplerian standard disk (Chakrabarti 1990, 1996), while the rest would remain sub-Keplerian (i.e. $\lambda < \lambda_K$, the Keplerian angular momentum). In outer regions, when the flow is sub-sonic ($v_{flow} < v_{sound}$), it is roughly Keplerian. After the flow becomes super-sonic ($v_{flow} > v_{sound}$), the flow becomes sub-Keplerian and passes through a standing or oscillatory shock induced by centrifugal force and becomes subsonic again – which enters through the inner sonic point (where Mach number

$M = \frac{v_{flow}}{v_{sound}} = 1$) to become super-sonic ($M > 1$). The region ($\sim \mathscr{O}[10r_g]$) between the shock and the event horizon is known as the "CENtrifugal pressure dominated BOundary Layer", acronymmed/abbreviated as CENBOL. It represents the Compton cloud and releases most of the observable X-rays in a Galactic black hole accretion. Soft photons from the Keplerian disk in the pre-shock flow are intercepted by the sub-Keplerian post-shock flow and are reprocessed due to inverse Comptonization (Chakrabarti 1996). If the post-shock matter remains hot, the BH exhibits a harder spectrum, whereas if the post-shock region is cooled down by the soft photons, a soft spectrum follows. There could be a sub-Keplerian region just before the shock as well since with low viscosity and accretion rate a Keplerian disk recedes from a BG and it is not necessary that the shocks form right at the region where a transition from Keplerian to sub-Keplerian flow takes place. Thus, the post-shock flow may have both thermal and non-thermal distribution of particles because of acceleration of particles across the shock (Mandal & Chakrabarti 2005). This would decide the hard photon spectral distribution.

Figure 1.5 shows schematically the main constituents of TCAF. The highly viscous Keplerian disk is immersed inside a low angular momentum halo component. The jets and outflows in this picture are produced primarily from CENBOL. The CENBOL is bounded outside by the shock at X_s. The CENBOL (and the base of the jet, as indicated in Fig. 1.5) intercepts soft-photons from the Keplerian disk and re-radiates them after Comptonization. The jets are accelerated by combinations of the hydrodynamic, magnetic and radiative forces. The collimation is possibly done by the toroidal field lines which are ejected from the disks due to buoyancy effects. From numerical simulations, Giri & Chakrabarti (2013) have shown that this TCAF configuration is indeed stable. Thus, spectral studies relying on the stability of TCAF configuration are realistic.

Free parameters in TCAF are the mass accretion rates corresponding to the Keplerian disk ($\dot{m_{disk}}$) and the sub-Keplerian halo ($\dot{m_{halo}}$) components, the shock location (X_s), and the shock compression ratio (R). Soft photon flux mainly depends on the disk rate, but the hard flux depends on all three parameters. The variation in X-ray fluxes emitted from the disk and the halo, and in spectral index directly reflects the change in the mass accretion rates of the two components close to the BH. Although viscosity is not explicitly required to fit an instantaneous spectrum, for studies of time evolution, its effects must be considered as the disk matter is ushered in by viscous processes. If the viscosity were constant for both the flows, the time variation at the outer edge would have been reflected at the inner edge of the disk after a constant viscous time delay. However, a SS73 disk requires a higher transport rate of angular momentum to maintain the Keplerian distribution, and thus is expected to have a higher viscosity parameter (the overall disk pressure is low). On the other hand, the advective component having low angular momentum requires very little viscosity for accretion (the ion pressure is high). As a result, out of the two flow components, the advective halo component arrives earlier than the Keplerian viscous component.

The viscous timescale in a standard Keplerian disk flow, t_{vis}, can be written as (Frank, King & Raine 2002)

$$t_{vis} = \frac{r^2}{\alpha_{SS} v_s z}, \tag{1.12}$$

where, α_{SS} is the SS73 viscosity parameter ($\alpha_{SS} < 1$), v_s is the speed of sound, z is the vertical height of the disk at a radial distance r away from the BH. The vertical height of the disk at any radial distance is calculated by balancing the vertical component of gravitational force with the gas pressure (Chakrabarti 1989). If any of these four quantities in Eq. 1.12 varies, t_{vis} will change. t_{vis} could remain constant for relatively smaller disks, provided the unknown viscosity parameter α_{SS} or pressure does not fluctuate appreciably. This is likely to be the case for HMXRBs. If the above equation is true, then a high value of α_{SS} in bigger disks, such as in LMXRBs, may result in small t_{vis}. However, both α and viscous stress can vary spatially and temporally. On the contrary, t_{vis} for a nearly inviscid sub-Keplerian flow (halo) is roughly comparable to the free-fall time t_{ff}. Therefore, a difference (lag or delay) in two timescales is expected. Since there is no possibility for t_{vis} to be less than t_{ff} in the sub-Keplerian flow, this time difference is defined as

$$\tau = t_{disk} - t_{halo} \approx t_{vis} - t_{ff}. \tag{1.13}$$

This is known as the *arrival time delay* or *time lag*. Thus, $\tau > 0$ will imply a Keplerian disk lagging behind the sub-Keplerian halo. If $\tau = 0$, it means that the inner disk moves simultaneously with the halo. This may happen before the outbursts observed in transient LMXRBs. Therefore, outbursts can be considered as excellent natural laboratories in revealing the evidence of two types of flow components by estimating the arrival time delay or lag (τ) and its effect on the geometry and spectral properties of accretion in BHBs.

In this Thesis, by using long-term satellite X-ray data, we have shown directly a clear evidence of two accretion flow components in several BHBs, either HMXRBs or LMXRBs. As the basic way of accretion in HMXRBs is wind-feeding, the accretion flow is predominantly sub-Keplerian which is nearly inviscid and the size of accretion disk is small. However, in LMXRBs, highly viscous and bigger accretion disk is formed mainly due to Roche lobe overflow. Both ways of accretion depend on the nature and behaviour of the companion star. In this scenario, a difference in time is obvious between the two flows arriving at the BH. This *arrival time* *lag* (*delay*) is of the order of viscous timescale ($\tau \approx t_{vis}$). Therefore, it is more likely to be detectable in LMXRBs than in HMXRBs. The time lag gives an estimation of the radial stretch or the size of the disk in its equatorial plane, particularly, when an outburst in LMXRBs or a transient phase (flare) in HMXRBs is about to take place. Crucial spectral properties are also inferred from such estimates. On the other hand, the influence of the original orbital motion of the companion long before accretion is smeared out by viscosity of the Keplerian disk in LMXRBs, but is retained by a nearly inviscid sub-Keplerian flow in HMXRBs. This aspect also provides a general idea about the size of the Keplerian disk in these two classes of XRBs.

In the next section, we briefly describe the methods of X-ray data analysis employed behind our findings. Results are discussed in Chapter 3 and Chapter 4 before summarizing in Chapter 5 at the end.

Chapter 2

Analysis of Satellite X-ray Data

We have used satellite X-ray data of several XRBs and analyzed their long-term (few years to about a decade) lightcurves in various energy bands. An overview of the satellites and the analysis procedures adopted for our study is briefly described in the following.

2.1 Rossi X-ray Timing Explorer (RXTE) satellite

Most of the observational results, to be presented later in this thesis, are obtained from the public data, archived by National Aeronautics and Space Administration (NASA), of Rossi X-ray Timing Explorer (RXTE) satellite, named after Itallian experimental physicist Bruno Rossi. The RXTE was launched on December 30, 1995 from Cape Carnival, Florida, United States, near the Atlantic coast and it remained active for about 16.5 years until it ceased science operations on January 3, 2012. RXTE had a mass of 3200 kg. The RXTE observed X-rays from BHs, NSs, X-ray pulsars and X-ray bursts. Detectors of RXTE had a time resolution of $1 \mu s$ and a signal sensitivity of 0.1 $mCrab$ and background sensitivity of 90 $mCrab$ over a broad energy range of $2 - 250$ keV. This enabled RXTE to probe temperatures, magnetic fields and other fundamental physical properties close to the observed compact objects as well as their geometry, nature and characteristics. In addition to the timing properties, the broad band spectral capability made RXTE an ideal instrument in analyzing the X-ray properties of the BHs for a long time observation. RXTE was placed into a low earth circular orbit with an altitude of 580 km and in a 23° inclination having a period of about 92 minutes. The satellite was to pass through the South Atlantic Anomaly (SAA) region during 6 out of $14 - 15$ daily orbits. During the SAA-passage, the instruments were put in safe mode for a protection from highly charged particle flux. One of the major advantages of RXTE was its maneuverability; the spacecraft could slew onto a source at $6^\circ/min$, allowing it to respond quickly to the X-ray sources, especially to the outbursts in transient LMXRBs. The mission was controlled by

NASA's Goddard Space Flight Center (GSFC), Greenbelt, Maryland. X-ray data recorded by the following two instruments aboard RXTE are used for our analysis.

2.1.1 All-Sky Monitor (ASM)

The All-Sky Monitor (ASM) instrument of RXTE operated in $1.5 - 12$ keV energy range and monitored around the sky scanning 80% of each satellite orbit. RXTE/ASM had three wide-angle Scanning Shadow Cameras (SSCs), each of which contained a Position-Sensitive Proportional Counter (PSPC). The total collecting area was 90 cm^2. The X-ray intensity and direction measurements are derived from the displacements and strengths of the shadow patterns cast by the X-ray sources with the camera's field of view (FOV). The detectors have a spatial resolution of $3' \times 15'$. Each camera has a FOV of $6^\circ \times 90^\circ$ and detection sensitivity of up to 2.265 SSC counts/second ~ 30 $mCrab$). The cameras mounted to a platform could rotate about its axis, dwelling at each sky position for 90 s. In this way about 80% of the sky passed through the FOV of ASM during each orbit. RXTE/ASM consists of three energy bands, viz. $A = (1.5 - 3\ keV)$, $B = (3 - 5\ keV)$ & $C = (5 - 12\ keV)$, along with the sum-band $S = (1.5 - 12\ keV)$. This allowed the ASM to monitor the overall $1.5 - 12$ keV intensity of few hundreds of XRSs.

2.1.2 Proportional Counter Array (PCA)

The Proportional Counter Array (PCA) aboard the RXTE satellite was built by NASA's Goddard Space Flight Center (GSFC). PCA consisted of five aligned nearly identical detectors, called proportional counter units (PCUs) with a total collecting area of 6500 cm^2. The PCA was sensitive to $2 - 60$ keV energy band with 18% energy resolution at 6 keV. However, only PCU2 unit remained active till 2012.

2.2 *Swift* satellite

Swift was launched into a low-Earth circular orbit at 600 km on November 20, 2004 and has still remained active. Its inclination is 20.6°. The largest instrument on-board *Swift* is the Burst Alert Telescope (BAT) with a CdZnTe detector having detecting area of 5200 cm^2, which can view approximately a sixth of the entire sky at one time. It is operating over $15 - 150$ keV energy range. However, the X-ray data of $15 - 50$ keV energy band are availble publicly. Swift/BAT records regularly about 10 data points per day of a given XRB and is reasonably good for a long-term timing analysis of our interest.

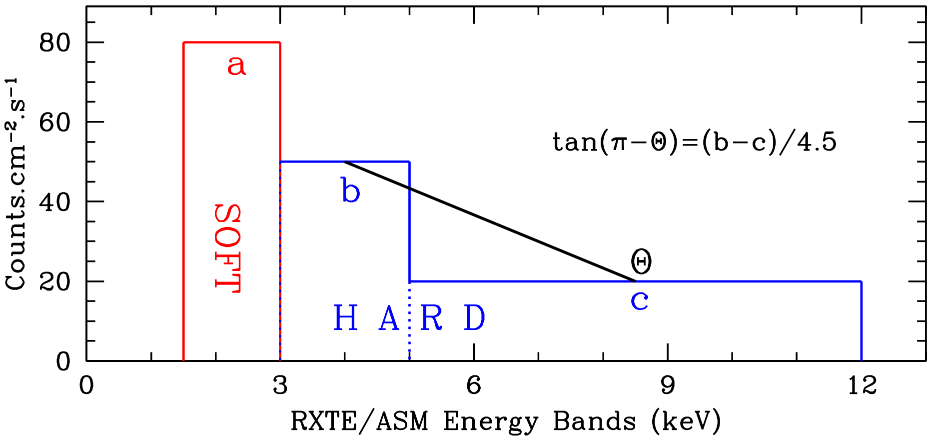

Figure 2.1: Θ is the slope of the hard region (power-law tail of *logarithmic scale*) of the spectrum drawn in *linear scale* from the tri-channel RXTE/ASM data. It is a *spectro-temporal dynamic photon index* susceptible to infinitesimal variation in both fluxes of photon and energy. By definition, $-1.57 < \Theta < 1.57$. In practice, $-1.57 < \Theta \leq 0$ since $c \leq b$ for equal energy binning (Credit: Ghosh 2018).

2.3 Analysis with RXTE/ASM data

It is realized that the spectral properties of all types of XRBs could not be properly understood unless those are studied for a long period of time ($\sim$ few years) in a proper manner, instead of fitting short-term ($\mathscr{O}[1000s]$) data of different satellites at irregular intervals with various models and arranging them on a truncated time line for an incomplete timing analysis. However, as RXTE/ASM recorded X-ray data ($1.5-12\ keV$) continuously for a long time with reasonably good numbers of data points ($\sim$ 20 per day) in *dwell-by-dwell* lightcurves in addition to the lightcurves with daily orbital average counts (i.e. 1 data point each day), a careful usage of ASM data would be the most suitable for the purpose. Despite the presence of negative counts due to background subtraction and stringent energy binning, these data are still proved to be useful for their continuous availability for a long duration of time. During outbursts, these negative counts become very less in number. Three energy bands, viz. $A = (1.5-3\ keV)$, $B = (3-5\ keV)$, $C = (5-12\ keV)$, and also the sum-band $S = (1.5-12\ keV)$ of ASM comprise both low-energy (soft) and high-energy (hard) photons, which are important in understanding both the radiative process and the flow dynamics associated with the accretion around BHs. Let a, b & c be respectively the number of photons per $cm^{-2}s^{-1}$ in A, B & C bands with mean energies of $E_A = 2.25\ keV$, $E_B = 4\ keV$ & $E_C = 8.5\ keV$ respectively.

2.3.1 Soft Flux and Hard Flux of Photons or Energy

In general, it is customary to assume that A-band, having absorbtion, represents soft photon flux a or soft energy flux aE_A pertaining to the energy range $1.5-3$ keV. On the other hand, B and C bands together represent the total Comptonized hard ($3-12$ keV high-energy) photon flux of $(b+c)$ or hard energy flux of (bE_B+cE_C). However, sum-band photons per $cm^{-2}s^{-1}$, $s=(a+b+c)$, are also used wherever necessary.

2.3.2 Hardness Ratio (HR) and Comptonizing Efficiency (CE)

There are two popular Hardness Ratios (HRs), designated in the literature by HR-1 (or HR1) and HR-2 (or HR2), associated with ASM data. HRs are commonly used for an initial guess on the degree of hardness (or softness) of the spectral states. These are defined in terms of a, b & c as

$$\text{HR-1} \equiv \text{HR1} = \frac{b}{a} \quad \& \quad \text{HR-2} \equiv \text{HR2} = \frac{c}{b}. \tag{2.1}$$

Both HR1 & HR2 represent *instantaneous fractional change of photons* between the pairs $b \leftrightarrow a$ & $c \leftrightarrow b$ respectively and both are generally expected to vary with time in a similar manner. HRs are used wherever necessary. The Comptonizing efficiency, denoted by CE (Pal & Chakrabarti 2015), is a measure of the inverse-Comptonization process. CE is defined to be the ratio of the number of hard photons to the number of soft photons injected into the CENBOL or Compton cloud (Ghosh & Chakrabarti 2018) as

$$CE = \frac{(b+c)}{a} \equiv \text{HR1}(1+\text{HR2}). \tag{2.2}$$

As CE includes information about both HRs, more emphasis has been given to this spectral parameter.

2.3.3 Dynamic Photon Index (DPI, Θ)

However, for the purpose of our work, we have used a *dynamic photon index* (DPI), denoted by Θ (Ghosh & Chakrabarti 2018, 2019). We shall see later that it behaves like a useful *spectro-temporal* parameter. The DPI is defined as

$$DPI \equiv \Theta = \tan^{-1}[\frac{(c-b)}{4.5}]. \tag{2.3}$$

Here, the scale factor of 4.5 arises from the difference in mean energies of C & B bands, i.e. $(E_C - E_B) = 4.5$ keV. This is illustrated by a schematic diagram in Fig. 2.1. We have used DPI extensively in our analysis. Θ behaves like a proxy of (i) HRs, (ii) usual photon index (Γ), (iii) spectral index, and (iv) CE at each instant of time for any source in any spectral state. However, Θ is most effective in the outbursts of transient LMXRBs.

Now, Θ represents the real slope at the harder photons of the spectrum using the *linear values* and not the logarithmic values of photon counts or photon energies. Therefore, Θ is expected to be more sensitive to instantaneous variations in all fluxes. With the usual definition of the power-law photon index Γ given by, $f(E) \sim E^{-\Gamma}$, a slope of $\Gamma \leq 2$ would indicate a harder state while $\Gamma > 2$ would indicate a softer state. This is the slope in the plot of $logf(E)$ vs. $logE$. Thus,

$$\frac{dlogf(E)}{dlogE} = -\Gamma. \tag{2.4}$$

However, we use $tan\Theta = \frac{df(E)}{dE} = -\Gamma\frac{f(E)}{E}$ to define the spectral state, since ASM count can be negative and log scale cannot be used. We have,

$$f \sim (-\frac{tan\Theta}{\Gamma})^{\beta}, \tag{2.5}$$

where, $\beta = \frac{\Gamma}{\Gamma+1}$. By definition, Θ has boundaries at $\pm\frac{\pi}{2}$, i.e. $-1.57 < \Theta < 1.57$. However, $tan\Theta$ is mostly negative in reality because $c < b$ is expected for data bins with equal energy, which is not the case in the ASM data. It may be noted here that in softer states, $f(E)$ is large and $\Gamma \rightarrow 4$; $\beta \rightarrow 0.8$, hence, $\Theta \rightarrow -1.57$. In harder states, it is expected that $f(E)$ is low and $\beta \rightarrow 0$; $f(E)$ tends to be a constant with $\Theta \geq 0$. The width of the C band is the largest among the ASM bands, so $c > b$ is possible and Eq. 2.3 may give $\Theta > 0$.

2.3.4 HR1, HR2, CE & DPI (Θ)

HR1 and HR2 represent *instantaneous fractional change of photons* between the count pairs $b \leftrightarrow a$ & $c \leftrightarrow b$ respectively while CE, having contained these fractional changes, represents a physical parameter which indicates the rate at which soft (black body) photons are converted into hard (power-law) photons via inverse Comptonization. However, all three can be arbitrarily negative due to the negative counts in RXTE/ASM data. On the other hand, DPI (Θ) represents *instantaneous relative change of photons* (comparable to a differential variation of photon fluxes) between the count pair $c \leftrightarrow b$. It becomes extremum at most to ± 1.57 due to its definition. Θ scans the relative change in the Comptonized photons in $3 - 12$ keV range and thus represents the rate of Comptonization. Ideally, Θ more or less mimics CE. So, it is a more useful parameter in understanding timing and spectral properties of all BHBs in a generic manner. Furthermore, HR2 and Θ would change almost similarly due to the quantities (i.e. the counts) involved in their definition. However, lower and upper limits of HRs (and so CE) can be arbitrarily low and high, whereas, the limits of Θ will be confined always within $\pm\frac{\pi}{2}$ for all BHBs. We shall see that Θ is the most important physical parameter of all four and it generically carries spectral information of various kinds in all the BHBs studied here.

2.3.5 Modified Lightcurves and Fourier Spectra

In order to observe both the long-time and the short-time behaviour of several XRBs, daily average data and dwell-by-dwell data (~ 20 data points per day) of RXTE/ASM for more than a decade are used. RXTE/ASM did not record X-ray data continuously from any particular source. Hence, there are gaps in the data, especially, due to the annual solar constraints. The unevenness of data interval is filled up by using a FORTRAN code for interpolating data at the equal time intervals (e.g. $0.05d$, $0.1d$, $1d$, etc.) of our choice or requirement. Apart from using these modified lightcurves directly (in Chapter 3), we have also invoked an *out-layer detection* procedure by using XMGRACE and FORTRAN codes for long-term (several years) lightcurves by a *robust scaling* (in Chapter 4). This scaling process further modifies the lightcurves about the running-average of the actual lightcurves. Using the PERL script ASCII2FLC, the FITS files of the lightcurves are created. High Energy Astrophysics Science Archive Research Center (HEASARC) available at the RXTE Guest Observer Facility (GOF) provides the XRONOS software package of NASA for the data reprocessing. In order to produce power density spectra (PDS) of the aforesaid lightcurves (FITS files) in Fourier space and cross-correlation (CC) between various quantities POWSPEC task (with norm -1) and CROSSCOR task (without any norm) are used respectively. NASA Exoplanet Archive, available online, is exploited for computing Lomb-Scargle periodograms (LSPs) and phase diagrams corresponding to the periods in them from the scaled lightcurves. Peaks observed in PDS are fitted with the standard Lorentzian model in order to determine centroid frequencies. The centroid frequency is considered to be a main characteristic of the peak arising due to many factors. The quality (Q) factor (i.e. ratio of the centroid frequency to the full width at half maximum (FWHM) of the Lorentzian, errors (χ^2 values and degrees of freedom), the area under a fitted peak when zoomed above the red noise level (integrated rms power for a peak), and the statistical significance of the observed peaks are estimated using the commands like FIT ERR, UNCER, STATISTICS, etc. available in NASA's FTOOLS package. For LSPs, we choose different fixed period step sizes (e.g. $0.0005d$) depending on the nature of the data and the periodicity that we wish to focus on. Standard conversion tables of the χ^2 distribution, p-values and Gaussian probabilities give the statistical significance in terms of the standard deviation (σ) of Gaussian distribution.

2.4 Analysis with *Swift*/BAT data

Swift/BAT $15-50$ keV orbital and daily-mean lightcurves for several years, either actual or modified (by the scaling procedure described earlier), have also been used. Fourier spectra of these lightcurves are produced by using POWSPEC task for generating PDS (keeping norm=−1) while periodograms and phase diagrams of periods are computed online by using NASA Exoplanet Archive as described before.

2.5 Analysis with RXTE/PCA data

For a particular XRB (Cyg X-1), we have also used high-energy X-ray data of RXTE/PCA. NASA/HEASARC's software packages HEASOFT (version HEADAS 6.18) and XSPEC (version 12.9.0) are used for the purpose. The reduction and analysis of PCA spectra involve following steps: data selection, background estimation, response-matrix generation and extraction of spectra with the FTOOLS & XSPEC packages. The *Standard2* data mode is used for all pointed observations. In order to generate the PCA spectral files, i.e. PHA files, we have used the SAEXTRCT task with applying the different filters as input (e.g. GTI information, time interval, energy channel selection etc.). Another important input for this background estimation is the SAA-passage history file. The RUNPCABACKEST task is run to produce the background data file. This task requires the *Standard2* data file, filter file, background models etc. as input. Background model varies from the bright sources to faint sources (<40 counts/sec/PCU) and from one Epoch to another Epoch. Lightcurves and spectra are extracted using the SAEXTRACT task while PCARSP creates the PCA response file (RSP file), which is the product of the Ancillary Response File (ARF) and Redistribution Matrix Function (RMF). For each data ID, the spectra from $2.5-25$ keV PCA spectra are extracted from PCU2 data and fitted with local additive model FITS files, generated from TCAF solution as described in Debnath, Chakrabarti & Mondal (2014). Data collected for elevation angles greater than 10^o, for offset less than 0.02^o, and those acquired during the SAA-passage, are excluded. *Standard2* mode Science Data of PCA (FS4a*.gz files) with $16s$ spectral binning are used. PCA breakdown correction and dead-time correction are done. Systematic error of 1% is included. In order to obtain the best fit, the interstellar absorption of the hydrogen column densities N_H in the unit of 10^{22} cm^{-2} (Grinberg et al. 2015) is taken for the absorption model *phabs*. In order to fit a spectrum using TCAF-fitting model, one needs to provide four input parameters of accretion flow, viz. two mass accretion rates $\dot{m_{disk}}$ & $\dot{m_{halo}}$, shock location X_s and shock compression ratio R. The accretion rates are in units of the Eddington rate ($\dot{M_{Edd}} = 1.4 \times 10^{17} M_\bullet \; gs^{-1}$), the location of the shock is in units of Schwarzschild radius (r_g), and R is dimensionless. The black hole mass $M_\bullet$ is also obtained in units of the solar mass $M_\odot$ from each fit as well. The unknown normalization factor is supplied and adjusted until it becomes nearly constant for all the observations while keeping the reduced χ^2 to a minimum.

2.6 Black Hole Binaries (BHBs) under consideration

The following twelve stellar mass BHBs are studied in this thesis:

- Transient LMXRBs: GX 339-4 & H 1743-322 (exhibiting multiple outbursts) and XTE J1650-500, XTE J1550-564, GRO J1655-40 & 4U 1543-47 (with sporadic outbursts)
- Persistent HMXRBs: Cyg X-1 & Cyg X-3
- Persistent LMXRBs: GRS 1758-258 & 1E 1740.7-2942
- Other LMXRBs: H 1705-25 & class-variable GRS 1915+105

Chapter 3

Direct Evidence of Two Component Accretion Flows around Black Holes

In this Chapter, we explore the general characteristics of arrival time lag τ between $t_{disk} \approx t_{vis}$ and $t_{halo} \approx t_{ff}$, respectively attributed to the Keplerian flow and the sub-Keplerian flow of TCAF paradigm (discussed in Chapter 1) from an extensive analysis of RXTE/ASM data for a long period of time. Our primary aim is to show that both flow components, whence they are segregated, move independently in the aforesaid timescales toward the black hole. Perturbative changes in specific accretion rates, $\dot{m}_{disk}$ and $\dot{m}_{halo}$, can originate simultaneously at a large radial distance interior to the outer edge (r_{out}) and take different amounts of time to reach the inner edge (r_{in}). An increase in $\dot{m}_{halo}$ would harden the spectra without changing the hard photon (power law) flux or soft photon (black body) flux significantly. As soon as the disk matter arrives at $X_s \sim r_{in}$ (i.e. the CENBOL surface) the CENBOL (Compton cloud) is cooled down quickly and the spectra become softened. In order to study this aspect Smith et al. (2002a) analyzed both RXTE/ASM ($3-12\ keV$) and RXTE/PCA ($2.5-25\ keV$) lightcurves for a common time frame of $\sim 5\ yr$ and normalized them by a suitable scaling. The normalized hard photon flux and its first order time derivative were correlated with respect to an empirical power law index, or PLI=$\frac{1.449}{\mathrm{HR2}}+0.698$ with HR2=c/b. Without having incorporated soft flux separately (but indirectly via PLI through inverse Comptonization of soft photons as seeds), they estimated time lags of $\mathscr{O}[10d]$ between PLI and hard photon flux in LMXRBs, viz. GRS 1758-258 and 1E 1740.7-2942, whereas no significant time lag ($\sim 0d$) was observed in HMXRBs, viz. Cyg X-1 and Cyg X-3. They interpreted these results in terms of two flow components as described in the TCAF paradigm and argued that a single component flow (e.g. Narayan & Yi 1994) or the persistent thin disk (Mineshige 1996) would be inappropriate.

Using RXTE/ASM tri-band data, we study several XRBs, belonging to three spectral categories, viz. transient, persistent and class-variable, in order to find the evidence of two accretion flows by estimating the time lag or delay ($\tau = t_{disk} - t_{halo}$) between them. As the Keplerian flow is responsible for the emission of soft (black body) photons while hard (power law) photons are controlled mainly by the sub-Keplerian halo, these two fluxes of photons (or energy) are correlated via the dynamic photon index, DPI or Θ, for finding a relative time lag, τ_r, between the two radiative components. However, the classic cross-correlation (CC) between them, i.e. CC(Hard, Soft), cannot give the time lag of our interest since the hard flux is not dependent on the soft flux alone but is a function of the size and the density of CENBOL as well. Two accretion rates do not independently emit two radiative components either. Both fluxes start rising when viscous matter starts moving into the disk. Therefore, we use Θ which gives the rate of enhancement of one component with respect to the other. As Θ varies continuously with the hard flux and also with the soft flux indirectly, we can compute its correlation with both fluxes and obtain the viscous time lag between them.

3.1 Relative Arrival Time Delay or Lag (τ_r):

If $t_{CC(\Theta,Soft)}$ and $t_{CC(\Theta,Hard)}$ are the outputs of cross-correlation (CC) of Θ with $Soft$ flux and $Hard$ flux of photons ($counts\ cm^{-2}\ s^{-1}$) or energy ($keV\ cm^{-2}\ s^{-1}$) respectively, then the relative arrival time lag between the two fluxes is given by (Ghosh & Chakrabarti 2018, 2019)

$$\tau_r = t_{CC(\Theta,Soft)} - t_{CC(\Theta,Hard)} \rightarrow \tau. \tag{3.1}$$

$\tau_r > 0$ implies that the disk radiation (black body) lags behind the halo radiation (power law). If $\tau_r = 0$, both evolve simultaneously.

τ or τ_r can be found directly from lightcurves if soft photon flux peaks later than the hard photon flux and the difference in their peaking instants of time gives our desired quantity approximately. Another way of finding the same is to compute the mass accretion rates from TCAF fits with high energy X-ray data and detect their peaking time difference (Debnath et al. 2014; Mondal et al. 2014; Jana et al. 2016; Molla et al. 2016; Ghosh, Banerjee & Chakrabarti 2019, hereafter GBC19). All these ways are feasible in finding the time lags in transient LMXRBs which exhibit outbursts either frequently or irregularly. But, Θ itself is a probe to estimate such timescales in outbursts. In the next section, we investigate if the physical picture given by TCAF paradigm is accurate and show how our observational results give a clear and unifying understanding of the temporal and spectral properties associated with them.

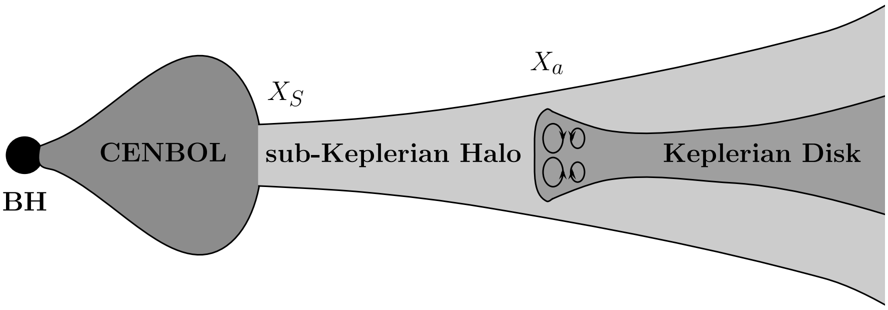

Figure 3.1: Quiescence before an outburst: When viscosity is lower than a critical value ($\alpha < \alpha_c$), the Keplerian disk matter cannot move inward but keeps piling up at a radial distance, X_a, known as *accumulation radius*. X_a is far away from the shock location, X_s, which determines the CENBOL boundary. The inner region is dominated by the sub-Keplerian flow and a hard state (HS) is observed in the spectrum (adapted from Chakrabarti, Debnath & Nagarkoti 2019).

3.2 Understanding Outbursts using TCAF Paradigm

Most of the time, BHBs show low and almost constant X-ray luminosity identified as a quiescence state for which $\Gamma < 2$ or $\Theta \geq 0$. Here, a Keplerian disk may be absent or may be formed far away ($\sim$ 1000 r_g) from the BH as the viscosity of accreting matter is low. An advective sub-Keplerian flow, due to its low angular momentum, does not require viscosity for accretion and it becomes predominant in quiescent states. On the contrary, if the viscosity is low at some radial distance away from the BH as the origin, the Keplerian disk matter with high angular momentum will not be able to move anymore towards the BH. The matter would be accumulated in an annular region at a large radial distance, X_a. This distance ($\mathscr{O}[100\ r_g]$) is far away from the CENBOL boundary at X_s and is termed as **accumulation radius** or **pile-up radius**. This is illustrated in Fig. 3.1.

When the Keplerian flow becomes highly viscous due to convective viscosity (α), which exceeds a critical viscosity parameter (α_c) (Chakrabarti 1990, 1996), a rapid inflow of disk matter prevails and an outburst ensues. Fig. 3.2 shows that the region between X_a and X_s is filled with Keplerian disk matter during such an outburst. Farther away from X_a and towards r_{out}, there is a two component flow with a Keplerian disk at the Centre and a sub-Keplerian matter. Observationally, an outburst is identified as a sudden rise in photon flux (or luminosity) in a typical form of Poisson distribution in the lightcurves, above the average photon counts of the quiescent phase (HS) as background. Such an outbursting XRB is called *transient*. This gives rise to a soft state (SS) at the peak of the outburst, for which $\Gamma > 2$ or $\Theta \to -1.57$. In a transient XRB, when high viscosity triggers an outburst the time lag between the two flow

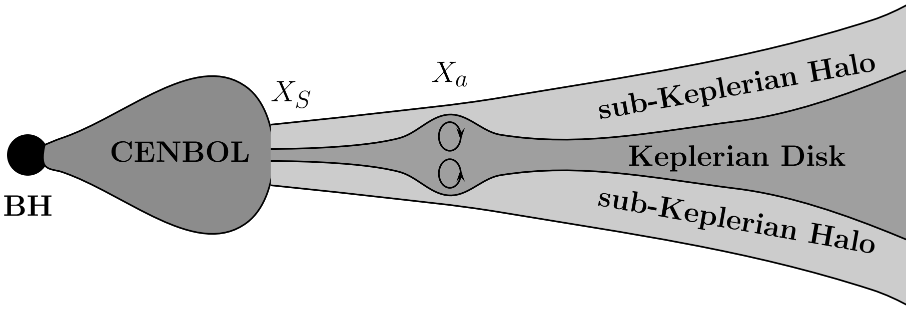

Figure 3.2: Onset of an outburst: When $\alpha > \alpha_c$, the Keplerian disk matter leaves X_a and moves in viscous timescale toward the CENBOL boundary at the shock location X_s. The time taken to reach X_s from X_a is called *arrival time delay* or *lag* (τ). The region between X_a and X_s is filled with disk matter during an outburst and this stretch gives the size of the accretion disk. The inner region is dominated by the Keplerian flow and a soft state (SS) is observed at the peak of the outburst when the CENBOL collapses (adapted from Chakrabarti, Debnath & Nagarkoti 2019).

components directly depends on the accumulation radius, X_a, from which they rush to the CENBOL (at X_s) in respective timescales before falling into the BH. Therefore, the stretch of $\Delta X = X_a - X_s$ approximately gives the Keplerian disk size which can be proportional to τ or τ_r. Thus, the arrival time lag and hence the disk size can be different in different outbursts, even in the same transient source.

3.2.1 RXTE/ASM Observation of 10 Outbursts in 5 Transient LMXRBs

Let us now present the results obtained from the hard ($3 - 12$ *keV*) photon flux, the soft ($1.5 - 3$ *keV*) photon flux and their responses to DPI (Θ) during ten outbursts observed in

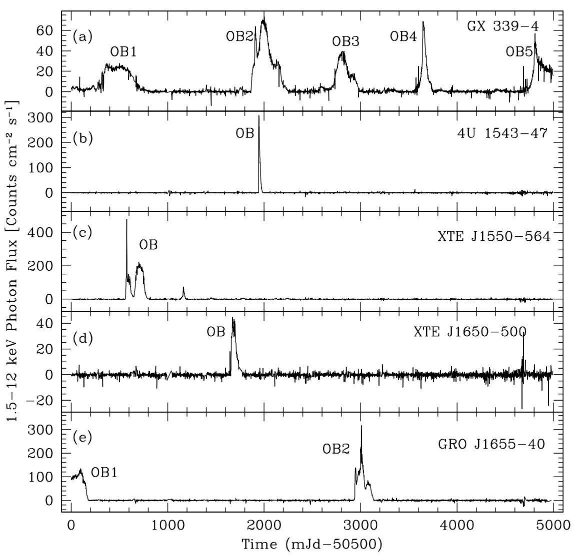

Figure 3.3: $1.5 - 12$ *keV* lightcurves of 5 transient LMXRBs with RXTE/ASM daily average data are shown. The outbursts are indicated by 'OB', followed by serial numbers for multiple OBs. OB1–OB5 of GX 339-5 in (a) are comparable to one another in terms of luminosity. However, from (b)-(d) it is evident that the luminosity of a sporadic outburst can be arbitrary (Ghosh & Chakrabarti 2018).

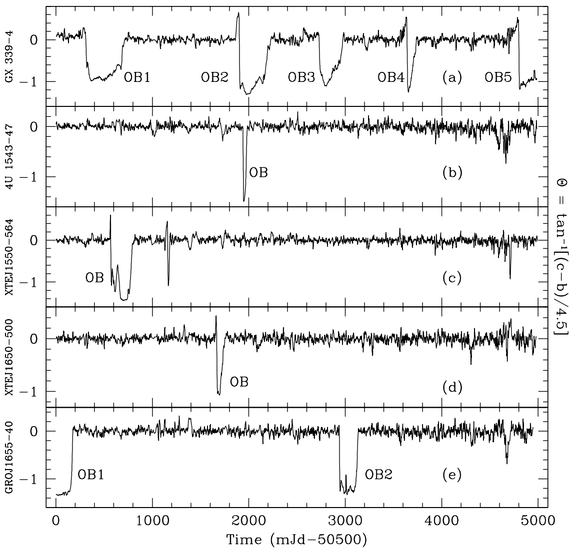

Figure 3.4: Weekly running-mean Θ (DPI) in the five transient sources is shown corresponding to Fig. 3.3. Well-like curves are indicative of outbursts (OBs). Θ drops drastically at the commencement of each outburst and rises again at its end. CE and HRs would also show similar troughs during the OBs, but elsewhere, their values would go up or down to arbitrarily large values (Ghosh & Chakrabarti 2018).

five transient XRBs, viz. GX 339-4, 4U 1543-47, XTE J1550-564, XTE J1650-500 & GRO J1655-40. Total ($1.5 - 12$ keV) photon fluxes for 5000 days (from 50500 to 55500 modified Julian day (MJD or mJd)) of these five sources, as recorded by RXTE/ASM on daily basis, are drawn in Fig. 3.3. However, weekly running average data are used in Fig. 3.4 to show the clear variation of Θ with time. Strong wells represent all the outbursts characteristically. Outbursts are denoted by OB in Figs. 3.3 & 3.4. Five successive outbursts of GX 339-4 are marked serially as OB1 to OB5 while two outbursts in GRO J1655-40 are marked as OB1 & OB2 and will be mentioned accordingly in the subsequent figures. All ten outbursts (OBs) are zoomed with daily average data in Fig. 3.5, where Θ (continuous/black) and CE (dotted/red) are plotted simultaneously. High values of CE are ignored. Both quantities are seen to vary similarly in all cases; both fall drastically soon after the commencement of all OBs and rise again at their culmination. This is due to the fact that the spectral state is hard and CE is the highest because of a large CENBOL at the onset of the rising phase as well as at the end of the declining phase of a typical outburst. Figure 3.5 hints at the potential of Θ that it cannot be just an empirical quantity but a physical parameter, which uniquely accomodates all outbursts in its restricted domain ($-1.57 < \Theta < +1.57$) both quantitatively and qualitatively.

3.2.2 Behaviour of DPI (Θ) during a typical Outburst

A typical outburst is characterized by four spectral states, viz. hard state (HS), hard-intermediate state (HIMS), soft-intermediate state (SIMS), and soft state (SS). Such an outburst typically evolve through the following spectral states: HS→HIMS→SIMS →SS→SIMS→HIMS→HS. This is schematically illustrated in Fig. 3.6 in terms of Θ. Θ should attain its highest value at the beginning (HS) and at the end (HS) of the outburst. By its mathematical definition,

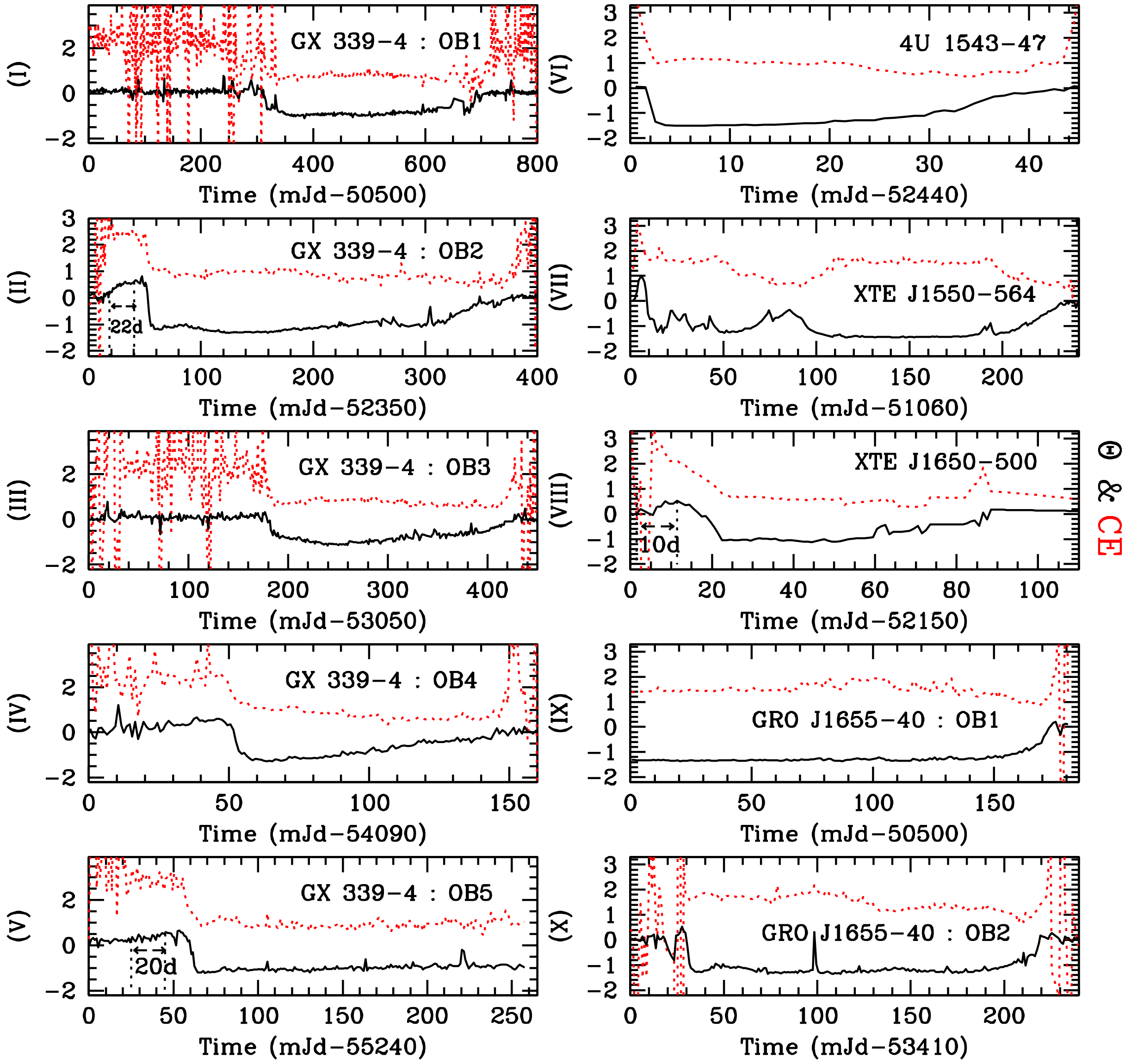

Figure 3.5: Both Θ (continuous) and CE (dotted) are drawn with daily mean data during ten outbursts of Figs. 3.3 & 3.4. High CE-values are not shown. Both Θ and CE, varying similarly, attain their highest values at the beginning and at the end of each outburst. For few outbursts, a HS→*harder state* spectral transition occurs prior to the softening. The time elapsed during this transition is approximately τ_r (as marked in II, V and VIII). Such a time lag of $\sim 5d$ is also present in (VII) (Ghosh & Chakrabarti 2018).

$-1.57 < \Theta < +1.57$. However, in reality, $\Theta \geq 0$, $\Theta_{\pm} \sim -0.5$ and $\Theta \rightarrow -1$ can be assigned to HS, HIMS/SIMS & SS respectively. Θ_{max} fluctuates about ≥ 0 in the HS while Θ_{min} may not go below -1.50 in the SS at the peak outburst. This justifies its theoretical limits. Therefore, the well-like Θ-curve of Fig. 3.6 represents all outbursts qualitatively and quantifies all spectral states in its common envelope. Such an outburst is called a *normal outburst*.

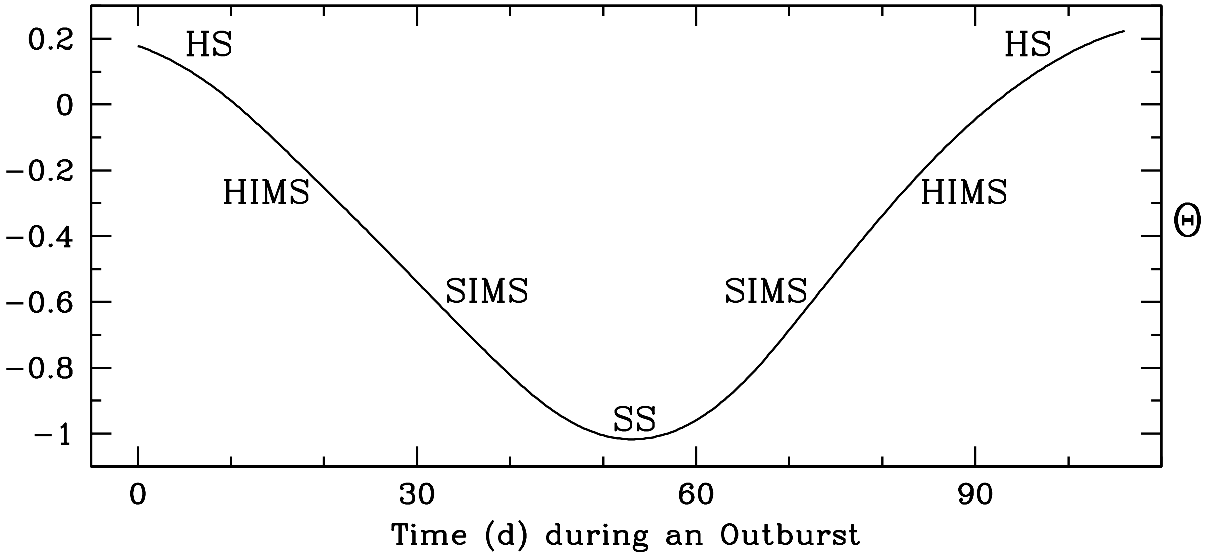

Figure 3.6: Schematic curve of Θ during a typical outburst accommodates hard state (HS), hard-intermediate state (HIMS), soft-intermediate state (SIMS), and soft state (SS) as shown. Spectral transition must undergo HS→HIMS→SIMS →SS→SIMS→HIMS→HS. Such an outburst is said to be *normal*. Θ is maximum (≥ 0) at the commencement (HS) and at the culmination (HS) of a normal outburst while the minimum Θ (> -1.57) is observed at the peak outburst (SS). $\Theta_{\pm} \sim -0.5$ in HIMS/SIMS (Ghosh 2018; Ghosh & Chakrabarti 2019).

Anomaly in a Θ-curve: Any significant deviation from the pattern of Θ-curve will indicate an *anomalous outburst*. Appearance of an extra SS or HS in this curve would imply an *anomaly* via a multiplicity (twin, trine, etc.) in the outburst. For example, the OB in XTE J1550-564 is clearly a twin outburst (Figs. 3.3c & 3.5(VII)). An interim HS at $\sim 100d$ (from MJD 53410) in OB2 of GRO J1655-40 (Fig. 3.5X) is also a similar anomaly. Therefore, lightcurves (for e.g. Figs. 3.3c & 3.3e) may or may not reveal such a twin. Several other anomalies, which may not be evident from the lightcurves but from Θ, are possible (Ghosh & Chakrabarti 2019).

3.2.3 Estimation of τ_r from Θ alone: An Excess of Spectral Hardening

As far as RXTE/ASM data are concerned, an increase of halo matter can increase c ($5-12$ keV) counts more over b ($3-5$ keV) counts without affecting the hard flux of photons ($b+c$) or mean energy (bE_B+cE_C) and the soft fluxes (a counts and mean energy aE_A) abruptly. In such a case, the spectrum gets hardened until the disk matter leaves the accumulation radius X_a and rushes inward. Then Θ gradually rises from its HS-value ($\Theta_{HS} \sim 0$) to the highest value ($\Theta_{hi} > 0$, e.g. $\Theta_{hi} = 0.5$) indicating a `harder state` or `super-hard state` (SHS). As soon as the disk matter reaches the CENBOL and increases the soft flux, power law tail gets steeper. Due to this softening, $\Theta \to 0$ again and decreases thereafter toward its lowest value in the SS. In the `harder (super-hard) state`, Θ attains its highest possible value ($\Theta_{hi} \equiv \Theta_{SHS} > \Theta_{HS}$) and drops thereafter when the softening starts. The time elapsed during this *spectral hardening* (i.e. `HS`→`harder state` or `HS`→`SHS` transition) at the commencement of the outburst is actually our desired τ_r. This can be estimated from Θ-behaviour alone if X_a is far away, i.e. τ_r is long or the disk is big in size. Θ initially fluctuates for some time along a *plateau* (see Figs. 3.5(I, III & IV) and later, Fig. 3.22), where Θ is roughly constant (≥ 0), before achieving the generic SS quickly. When τ_r is long, the Θ-curve will show a *bump* on the plateau. Figures 3.5(II & VIII) clearly show such bumps indicating time lags of 22d and 10d respectively for OB2 in GX 339-4 and OB in XTE J1650-500. A time lag of $\sim$ 5d is evident also from such a bump in 3.5(VII) for XTE J1550-564. There is a possibility that $\Theta = \Theta_{hi}$ is maintained for some more time, $\tau(\Theta_{hi})$ (few days to a week), in lieu of $\tau(\Theta_{HS} \to \Theta_{hi})$, when the hard flux also continues to retain its already achieved peak (in the lightcurve) until the soft flux grows enough to control the spectrum prior to its peaking. Therefore, Θ will scan all such intervals. Let us write the overall time lag as

$$\tau(\Theta_{HS} \to \Theta_{hi}) + \tau(\Theta_{hi}) \equiv \tau_r. \tag{3.2}$$

However, $\tau(\Theta_{HS} \to \Theta_{hi})$ does not ensure the occurrence of the occasional lag $\tau(\Theta_{hi})$. On the other hand, if X_a is nearby, τ_r is small and a small disk is obvious, then Θ initially fluctuates rapidly for some time about the plateau (see Figs. 3.5(I & III) and Fig. 3.22 later), where $\Theta \geq 0$, before achieving the generic SS directly. In such cases, $\tau_r \to 0d$ is implicit from this almost smooth and horizontal plateau of the Θ-curve. This negligible lag means that both disk and flow reach from X_a to Xs almost simultaneously. This will result in two concurrent peaks in the lightcurves of soft and hard fluxes. This is in contrast with the appearance of bumps over the plateau when $\tau_r \gg 0d$ is roughly equal to the time span of such a bump. So, Θ is a dynamic spectro-temporal parameter which minutely traces any outburst like an indicator and reveals both temporal and spectral characteristics.

τ_r is to be computed from the cross-correlation (CC) of Θ with the soft and hard fluxes, i.e. CC(Θ, Soft) & CC(Θ, Hard) by using Eq. 3.1. $\tau(\Theta_{hi})$ can be obtained from CC(Hard, Soft) and/or from the behaviour of the peaks in the lightcurves, hard flux will show a blunt/flat peak (see Figs. 3.7(d1) & 3.8(c1)).

3.2.4 Computing τ_r from CC(Θ, Hard) & CC(Θ, Soft)

Figures 3.7 & 3.8 respectively show five successive outbursts of GX 339-4 and four other outbursts of the four sources, viz. 4U 1543-47, XTE J1550-564, XTE J1650-500 and GRO J1655-40 in terms of daily average lightcurves for soft and hard photon fluxes, Θ (exploiting the same vertical scale used for the photon fluxes but ignoring their unit), and CC-profiles. In each case, hard and soft fluxes are respectively drawn by dotted/blue and continuous/red lightcurves. Dotted/blue and continuous/red curves represent the CC-profiles of Θ with hard and soft fluxes respectively. Θ and flux-flux correlation curves are drawn in dot-dashed/black. OB1 of GRO J1655-40 with an outcome of $0d$ lag is not included here (its declining phase is shown in Figs. 3.3e, 3.4e & 3.5(IX)). In view of Figs. 3.5(II, V, VIII), 3.7(b1, e1) & 3.8(c1), it is evident that when τ_r is high, as obtained from the results of CC(Θ,Hard) & CC(Θ,Soft) in Figs. 3.7(b2, e2) & 3.8(c2), it is reflected from the Θ-behaviour alone. In particular, OB2 of GX 339-4 shows prominently a lag of $22d$ (see Figs. 3.5(II) or 3.7(b1)), which is consistent with the time lag of 19d computed from CCs in Fig. 3.7(b2). In Fig. 3.5(II), Θ rises from its HS value ($\Theta_{HS} \sim 0$) at the commencement of OB2 to a harder state value ($\Theta_{hi} \sim 0.6$); the time elapsed in such a spectral hardening is the desired time lag. The time lag of $\sim 5d$, as was evident from 3.5(VII) for the twin OB of XTE J1550-564, contradicts with the corresponding outcome ($1 \pm 1.4d$) in Fig. 3.8(b2) because CC-curves were not computed separately for its first part.

3.2.5 Extracting Time Lags from Lightcurves and CC(Hard, Soft) Curves

For normal outbursts, lightcurves corresponding to soft and hard fluxes implicitly indicate the arrival time delay, in particular, for $\tau_r \sim 0d$, as both will show peaks at similar time. But, if $\tau_r \gg 0d$, then the soft flux could peak a few days later than the hard flux peaks. The time difference between such two prominent peaks (τ_{lc}) can be estimated directly from two lightcurves. From Fig. 3.8(c1) showing the outburst in XTE J1650-500, $\tau_{lc} \sim 10d$, which agrees with the outcome of $\tau_r = 10d$ from both Θ and its CCs with the fluxes. On the other hand, Fig. 3.7(e1) indicates, $\tau_{lc} \sim$ a few days. This, however, is very less as compared to the computed $\tau_r \sim$ a few weeks. In such a case, if two accretion rates, $\dot{m}_{halo}$ and $\dot{m}_{disk}$, for such an outburst are known from TCAF-fits or otherwise, then $\dot{m}_{disk}$ most likely shows a peak belated with respect to $\dot{m}_{halo}$ by $\tau_{\dot{m}}$. But, it is obvious that $\tau_{lc} \approx \tau_{\dot{m}} \neq \tau_r$ (see later Figs. 3.20b-c and Fig. 3.21 in §3.3.3).

The classic and a direct method of cross-correlation (CC) between the hard flux and the

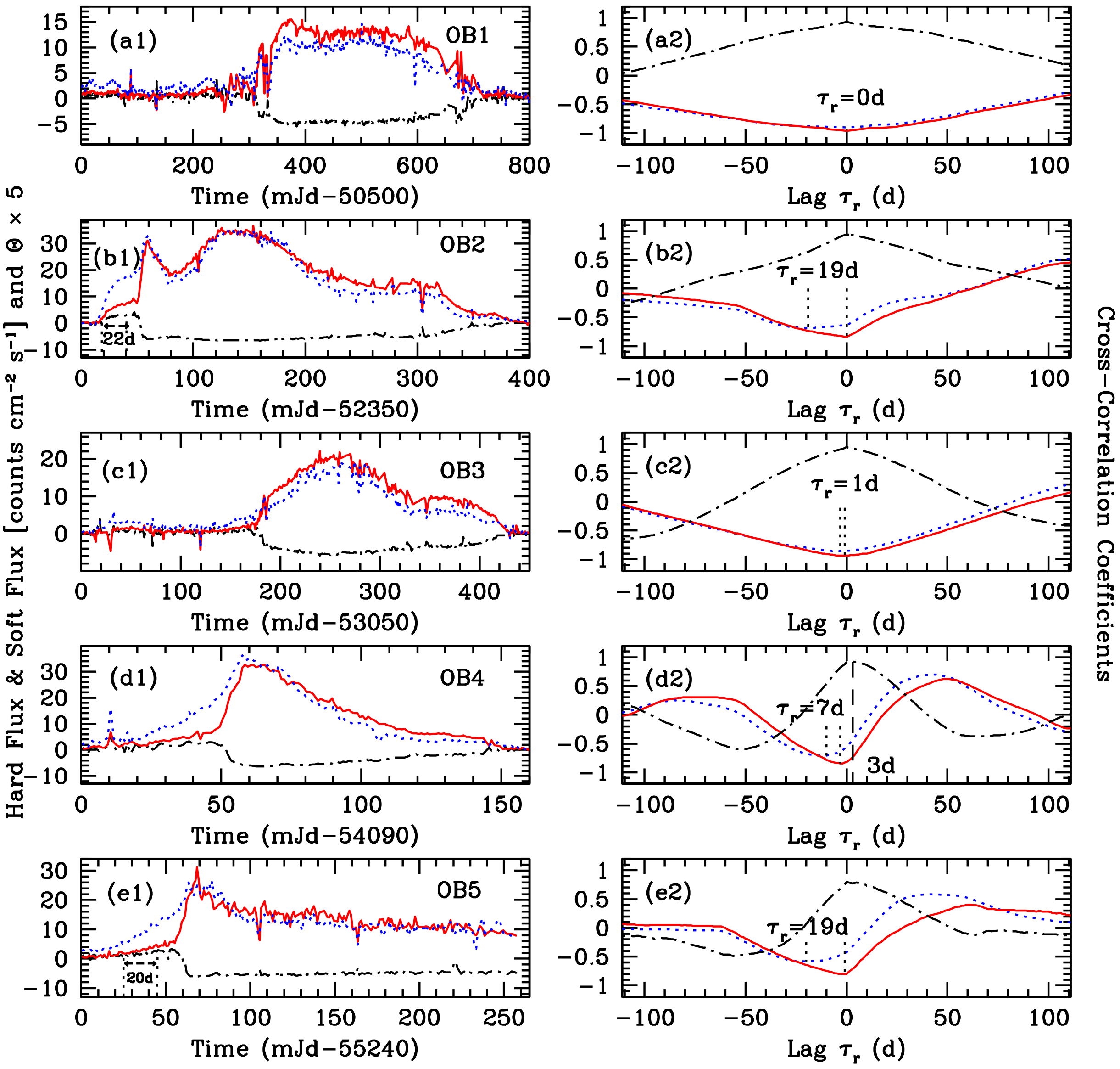

Figure 3.7: Five successive outbursts of GX 339-4: (*Left*) Both photon fluxes along with amplified Θ (ignoring the unit for the fluxes but exploiting the same vertical axis scale) drawn with daily average data. (*Right*) Corresponding CC curves are plotted. Continuous/red and dotted/blue curves are pertaining to soft flux and hard flux in terms of lightcurves and CC-profiles with Θ respectively, while dot-dashed/black curves refer to Θ and CC(Hard, Soft). τ_r-values, obtained from CC(Θ, Soft or Hard), are marked in each box. CC(Hard, Soft) results in $\tau_r = 0d$ in (a2), (b2), (c2), and (e2), whereas a lag time of $3d$ is marked in (d2). Time stamps labeled in (b1) & (e1) are the approximate times of an extra spectral state transition (HS → `harder (super-hard) state`) estimated from Θ alone. As expected, these are consistent with τ_rs marked in (b2) & (e2) respectively (Ghosh & Chakrabarti 2018).

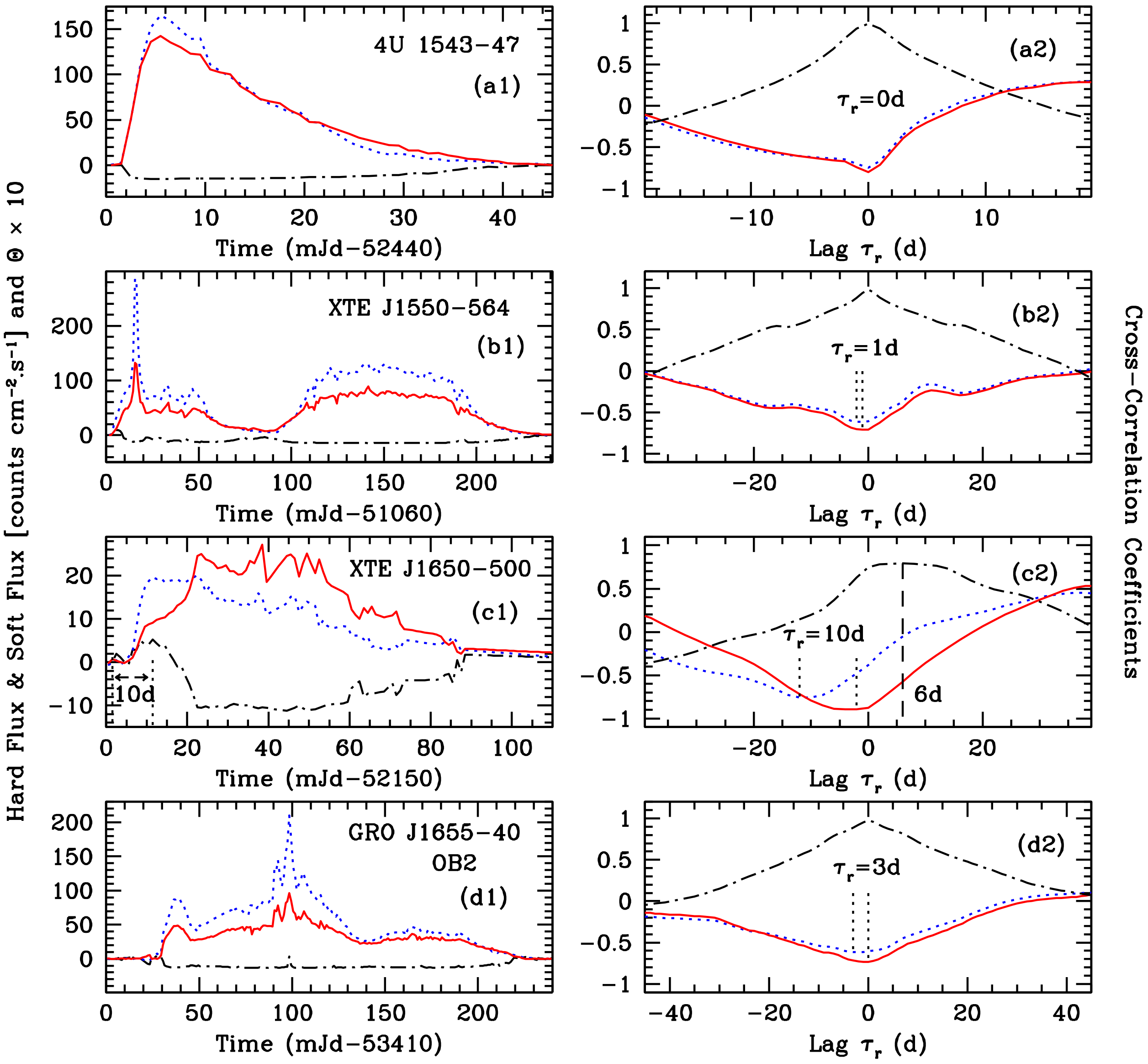

Figure 3.8: Sporadic outbursts in 4U 1543-47, XTE J1550-564, XTE J1650-500 & GRO J1655-40: (*Left*) Daily average lightcurves and amplified Θ (exploiting the same vertical scale but ignoring the unit of the fluxes) are shown. (*Right*) Corresponding correlation profiles are shown. Line types or colour stamps are the same as in Fig. 3.7. τ_r-values, obtained from CC(Θ, Soft or Hard), are marked in each box. CC(Hard, Soft) gives $\tau_r = 0d$ in (a2), (b2), and (d2), but a lag time of $6d$ is indicated in (c2). The timescale marked in (c1) is the approximate duration of HS → `harder (super-hard) state` spectral transition and is consistent with the outcome in (c2). Both indicate similar time lags (Ghosh & Chakrabarti 2018).

soft flux, i.e. CC(Hard, Soft), is not the best thing to do for computing the time lag, even if the lightcurves indicate $\tau_{lc} > 0d$ as the peaking time interval. This is because the hard flux does not depend on the soft flux alone. It also depends on the properties of the Compton cloud (CENBOL) such as its size and its optical depth. Furthermore, both fluxes start to rise at the beginning of an outburst. So, in general, no significant lag between these two fluxes can be expected to be seen from CC(Hard, Soft). But, CC(Hard, Soft) could result in $\tau(\Theta_{hi})$ (the second term in Eq. 3.2), when $\Theta = \Theta_{hi}$ is maintained in the harder state for a significant time (when the soft flux is still rising for achieving its peak) and the hard flux also roughly maintains its already achieved peak value during the rising phase of the soft flux. $\tau(\Theta_{hi}) = 6d$ and $\tau(\Theta_{hi}) = 3d$ are obtained from CC(Hard, Soft) for the outburst in XTE J1650-500 and for OB4 in GX 339-4 as evident from Figs. 3.8(c1-c2) & 3.7(d1-d2) respectively.

However, qualitatively, CC(Hard, Soft) profiles are important. These curves show peaks mostly at $\tau_r = 0d$ with symmetric spreads on both sides if CCs with Θ also result in $\tau_r \to 0d$ for an outburst with sufficiently long ($\sim 100d$, say) duration. Otherwise, i.e. when $\tau_r \gg 0d$, CC(Hard, Soft) curves will lose this symmetry and seldom reveal a lag $> 0d$. Such a symmetry has a direct connection with the *hysteresis* property of the physical process controlling the fluxes. In general, if any two physical quantities show an asymmetric peak in their CC-profile then there must be some common dissipative mechanism which generates, or at least, governs them. In our context, we shall see later that the aforesaid two cases are also important in classifying the outbursts.

3.2.6 Hysteresis Loops with Θ & CE

We have seen from Fig. 3.5 that both Θ and CE vary similarly in all ten outbursts except that CE can go up or down to very large values while Θ is always confined in a limited range of ± 1.57. This is why we have considered only Θ for computing τ_rs and use it to interpret our results. Qualitatively, both Θ and CE behave similarly. To illustrate this further, their values at mean, maximum and minimum are plotted with τ_r for all outbursts in Fig. 3.9. All quantities are seen to vary similarly, but the maximum magnitude of CE indefinitely fluctuates as $\tau_r \to 0d$ though it becomes approximately stable for $\tau_r \gg 0d$. Let us see how the total energy liberated in the outbursts behaves with respect to both Θ and CE.

In Fig. 3.10 the mean intensity in all ten outbursts is plotted as a function of Θ with running average data for clarity and comparison. Here, the outbursts are arranged anticlockwise in the descending order of τ_r-values (marked in each box) from the top left Fig. 3.10a to the top right Fig. 3.10j. We see that $-1.5 < \Theta < 1$ for all the cases, though Θ does not normally go above ~ 0.5. For each outburst, Θ traces a loop anti-clockwise between the two generic HSs, which appear near the farthest right point of the loop. This particular point, where the two HSs coincide if $\tau_r \to 0d$ (e.g. Figs. 3.10f & 3.10h), represents the harder state if $\tau_r \gg 0d$ (e.g.

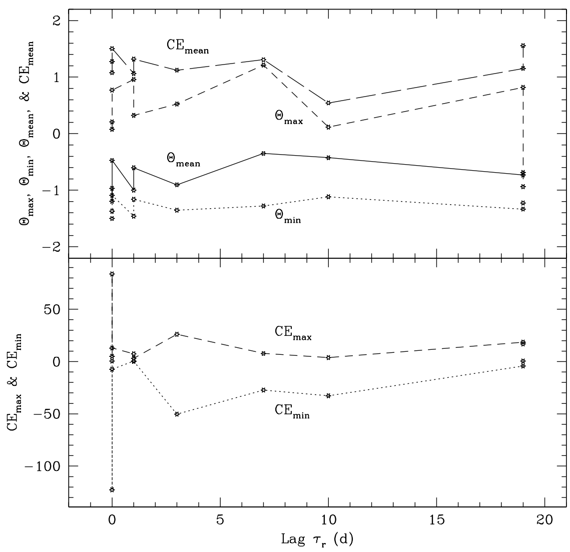

Figure 3.9: The minimum, maximum, and mean values of both Θ and CE during all outbursts are seen to vary with τ_r in a similar manner. The maximum magnitude of CE shows instability as $\tau_r \to 0d$, obtained in OB-I type outbursts in LMXRBs forming small disks. It does not vary too much with $\tau_r \gg 0d$, observed in OB-II type outbursts in LMXRBs having bigger disks (Ghosh & Chakrabarti 2018).

Figs. 3.10a-d). The farthest left point of the loop represents the generic SS flanked by the aforesaid HSs within which the outburst is spectrally bound. This can be understood from the incomplete loop in Fig. 3.10a where the outburst OB5 of GX 339-4 partially lacks its declining phase due to the truncation of data (see Fig. 3.7(e1)); the open end on the right indicates the initial HS while the farthest right point represents the harder state. On the other hand, the outburst OB1 of GRO 1655-40 in Fig. 3.10i is in its declining phase (due to the data choice, see Figs. 3.3e, 3.4e & 3.5(IX)) and this gives rise to an incomplete loop. Therefore, a closed loop arises when the outburst is fully considered. In such a case, the excursion path of the loop has a specific pattern, which is analogous to the so-called *q-diagram* observed in a typical HR-intensity diagram of an outburst (e.g. Capitanio et al. 2009). The area bound by the loop appears to be roughly proportional to τ_r if $\tau_r \gg 0d$. However, outbursts with $\tau_r \to 0d$ result in loops having arbitrary areas and distortion. In any case, a simple closed loop ensures a normal outburst irrespective of τ_r-values. If any significant deviation is present in the Θ-curve of an outburst (see §3.2.2) then it will be evident from the corresponding loop. For example, the twin outburst of XTE J1550-564 (Figs. 3.3c, 3.4c & 3.5(VII)) appears as a two-fold loop in Fig. 3.10f and indicates an anomaly. Similar anomaly is present in Fig. 3.10e as well, where OB2 of GRO J1655-40 is shown, due to an interim HS at ∼ $100d$ (from MJD 53410) observed in Fig. 3.5X & Fig. 3.8(d1).

Hysteresis is a phenomenon in which the relation between two physical quantities depends on whether one quantity is increasing or decreasing with respect to the other. This is a measure of the tendency (or the difficulty) in maintaining (or restoring) the system in its most stable configuration. In our context of studying the variation of intensity with flow parameters, it is an inability to retrace the rising phase track by the declining phase. In Fig. 3.10, the loop

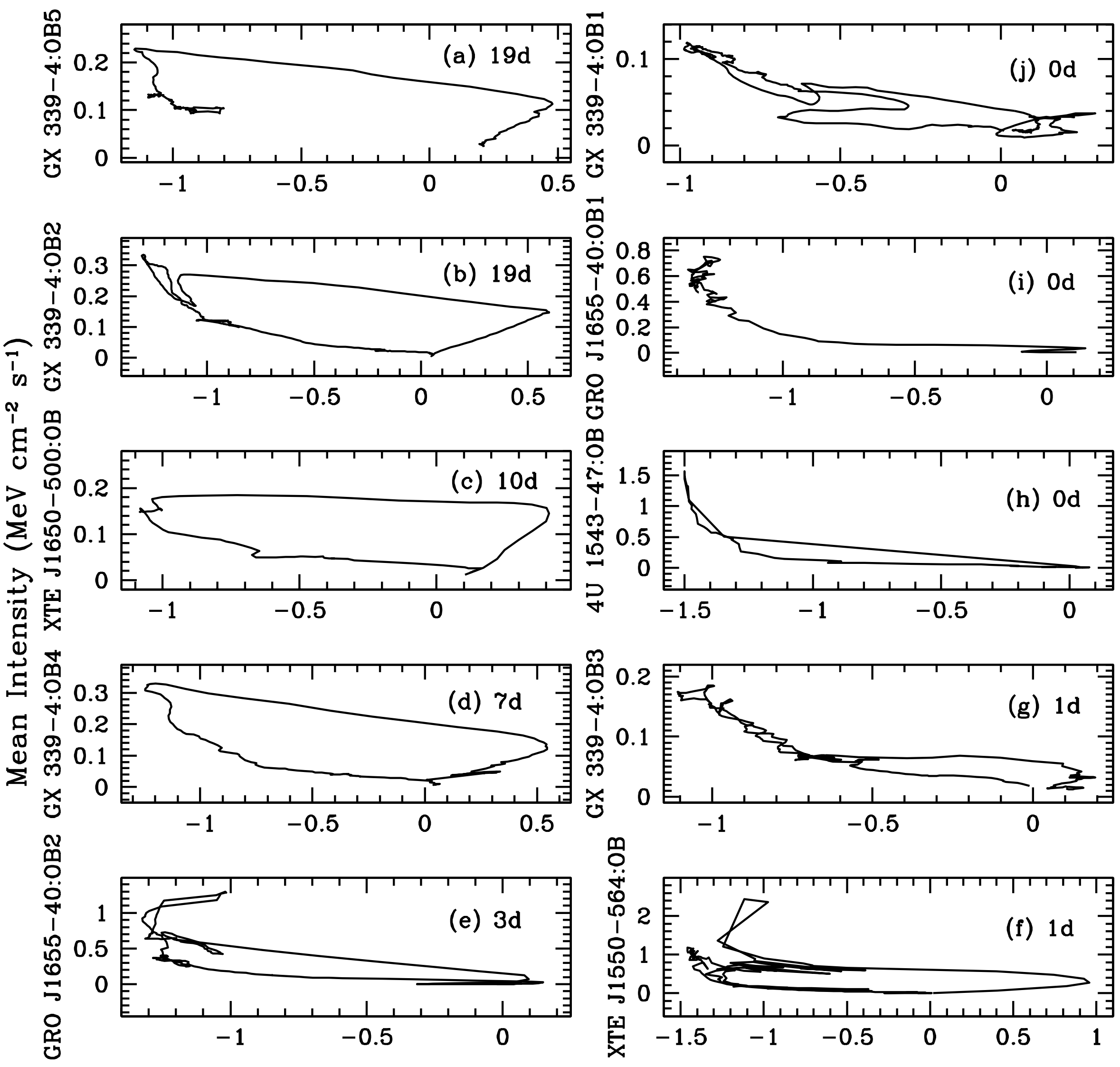

Figure 3.10: *Hysteresis loops*: Mean intensity of each outburst is plotted with running-mean values of Θ obtained from the same data used in Ghosh & Chakrabarti (2018). τ_r values are marked in boxes (a)-(g), in descending order from the top left. Ideally, each loop is traced anticlockwise by Θ between the two generic HSs converging to the farthest right point in the loop) within which the outburst is bound spectrally. The generic SS (the farthest left point in the loop) flanked by the HSs. An ideal Θ-behaviour of Fig. 3.6 would give rise to a closed and smooth loop, indicating a normal outburst. The loop gradually becomes thinner as τ_r disappears. As $\tau_r \rightarrow 0d$, the *hysteresis* loops become narrowed further in (g) to (j). Incomplete loops in (i) and (a) are respectively due to the outburst in its declining phase and the outburst partially lacking this phase because of the truncated data. So, such a *hysteresis loop* is physically more significant over the *q-diagram* of a HR-intensity diagram for a normal outburst as its area is proportional to $\tau_r > 0d$ but can be arbitrary if $\tau_r = 0d$. In general, the loops on the left and the right respectively represent OB-II and OB-I types of outbursts.

area is a measure of *hysteresis loss*, i.e. the amount of matter (and energy) dissipated away in the corresponding outburst. A large Keplerian disk takes a long time to disappear. Moreover, $\tau_r \gg 0d$ also means a large Keplerian disk. Thus, the retracing route deviates by a large margin in such a case. Therefore, loop area is also related to the outburst duration. This is why we prefer to study all outbursts as a whole instead of examining their rising and declining phases separately. Hence, both τ_r and the area of the *hysteresis loop* indicates the Keplerian disk size, which varies from one outburst to another. However, for $\tau_r \to 0d$, the dissipation can be arbitrarily high or low and energy with less disk matter would most likely to cause outflows (and jets, if other necessary physical flow conditions are satisfied). Numerical simulations also indicated that the hysteresis loop in an outburst is due to an inability of the Keplerian disk to be dissipated quickly in the absence of viscosity after the achievement of the SS (Roy & Chakrabarti 2017). Therefore, only from the behaviour of Θ and the corresponding hysteresis loop several characteristics of an outburst can be ascertained.

In order to show similar a response of the mean intensity to CE during the outbursts, we have plotted them in Fig. 3.11 (in the same manner as in Fig. 3.10). In Fig. 3.11 (*left*), actual daily average values are shown with both points and line as well. We can see that the points having very large magnitude (both positive and negative, due to ASM data type) of CE are very less in number. Therefore, the curves are zoomed with $0 \leq$CE≤ 4 and are shown in Fig. 3.11 (*right*). All our results drawn from the previous Θ-*hysteresis loops* are corroborated by the CE-*hysteresis loops* of Fig. 3.11.

3.2.7 Determination of Accretion Disk Size

We have seen from the schematic cartoon diagram in Fig. 3.2 that the region between X_a and the outer surface of the CENBOL at X_s is filled during the outburst. However, the viscous disk matter will take more time than the advective halo matter in traveling from X_a to the CENBOL. As a consequence, the advective halo component arrives earlier than the viscous disk component by τ_r. This timescale directly implicates lengthscale, i.e. the radial size of the disk formed just before the occurence of an outburst. However, this is an estimation of the disk size in one outburst relative to that in the other outburst of either the same source or the other. For example, large disks were formed before OB2 & OB5 in GX 339-4 and the OB in XTE J1650-500; all other outbursts occurred after the formation of smaller disks. In general, transient LMXRBs exhibiting sporadic outbursts most likely are to arise from either a small disk (e.g. XTE J1550-564) or a disk with moderate size.

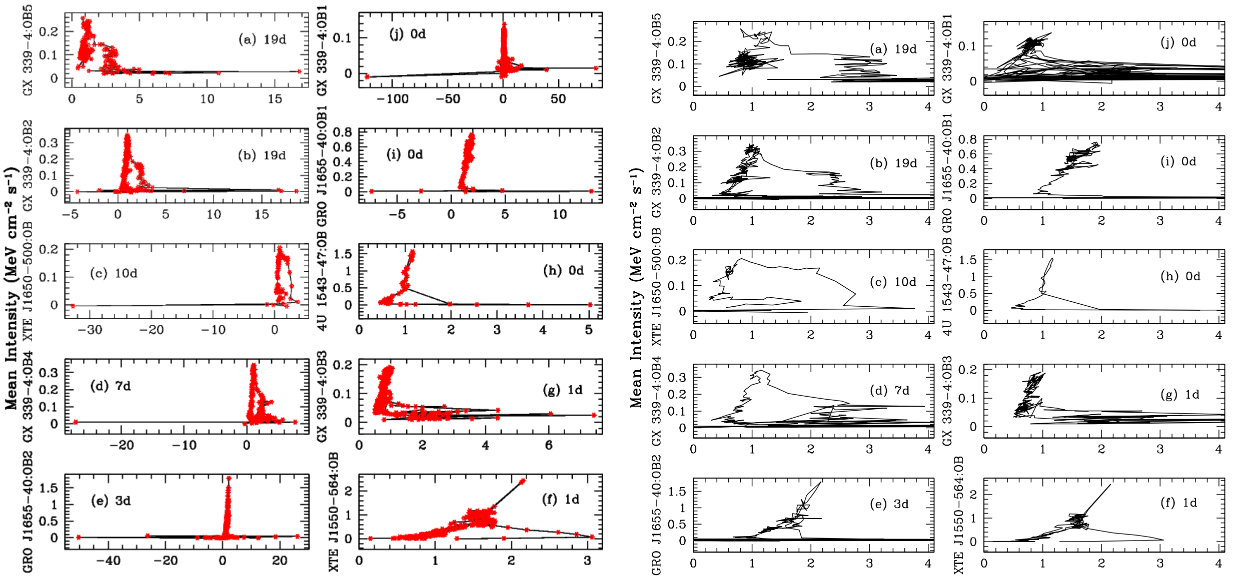

Figure 3.11: (*Left*) Mean intensity in all the outbursts is plotted with CE. Large values of CE, arisen due to RXTE/ASM data in some cases, are few in number and CE is more or less confined between 0 & 4. (*Right*) When zoomed in the range, 0 $\leq$CE$\leq$ 4, *hysteresis loops*, similar to those with Θ, follow once again. For $\tau_r > 0d$, loop areas appear to be proportional to τ_rs, or the amounts of energy liberated during the outbursts (OB-II type) of longer duration. However, for $\tau_r \rightarrow 0d$, loops are arbitrarily narrow and disrupted; radiated energy in such OB-I type outbursts of shorter duration can also be arbitrary.

3.2.8 Classification of Normal Outbursts: OB-I & OB-II

We can classify the outbursts (OB) in two categories: OB-I and OB-II, based on both physical and observational points of view (Ghosh & Chakrabarti 2018; Ghosh 2018). For an accumulation radius X_a nearer to the CENBOL at X_s, the arrival time lag τ_r will be negligibly small ($\tau_r \rightarrow 0d$) and so, the corresponding disk size will also be small. In this case, the resulting outburst belongs to OB-I type. On the other hand, if the accumulation radius is far away from the BH (i.e. $X_a \gg X_s$), then τ_r will be long ($\tau_r \rightarrow$ several days to a few weeks) and a large disk will be formed. In this case, the outburst will be called OB-II type. For OB-I type outbursts, the CENBOL may be small or squeezed to accommodate nearby a small disk, which dissipates itself quickly due to its negligible hysteresis into outflows (or jets, if other conditions are satisfied as well) which may be available as sub-Keplerian matter for a next episode. We shall see in §3.5 that OB-I outbursts are similar to the flares in HMXRBs like Cyg X-1 or in a variability source like GRS 1915+105 (Ghosh & Chakrabarti 2018). For OB-II type outbursts, the CENBOL may be big or inflated while a large disk is formed from afar and it liberates a huge amount of energy for a long time before the matter disappears into the black hole.

Figures 3.5, 3.7 & 3.8 show the difference between OB-I type and OB-II type outbursts from observational characteristics. The outbursts in Figs. 3.7(a1, c1) and 3.8(b1, d1) are OB-I type while those in Figs. 3.7(b1, d1, e1) and 3.8(c1) belong to OB-II type. In an OB-I, both soft and hard fluxes increase in a similar manner throughout the duration of the outburst ($t_{OB} = t_{ri} + t_{de}$). The duration of the rising phase (t_{ri}) is comparable to that of the declining phase (t_{de}) about the peak outburst. For $t_{OB} > 60d$ (say), $1 < \frac{t_{de}}{t_{ri}} \leqslant 2$. Figures 3.5(I, III, VII & X) show that CE and Θ fluctuate more about their mean highest values (CE≥ 2, $\Theta \geq 0$) in the HS along two *plateau*s at the commencement of the OB-I type outbursts before dropping quickly to their lowest values in the SS. In OB-II type outbursts, hard flux increases first and faster than the soft flux in the rising phase. The duration of their declining phase (t_{de}) is longer than that of the rising phase (t_{ri}). For $t_{OB} > 60d$ (say), $2 < \frac{t_{de}}{t_{ri}} \leqslant 6$. It is readily observed from Figs. 3.5(II, IV, V & VIII) that at the onset of the outbursts Θ and CE are roughly steady and Θ becomes steeper showing bumps (due to an excess of spectral hardening) above its plateau ($\Theta \sim \Theta_{HS}$), before falling off relatively slowly to its minimum toward the SS. Sporadic outbursts of transient LMXRBs of short duration ($t_{OB} < 60d$, say), as that of 4U 1543-47 shown in Fig. 3.8(a1), most likely belong to OB-I (Ghosh & Chakrabarti 2018).

For a ready reference, these features of difference between OB-I and OB-II types are summarized in Table 3.1.

3.2.9 Twin Outburst: An Anomaly in the Outburst

Visually, the lightcurves during a typical outburst show a uniformly resolved peak in a unique SS with significant photon counts distributed (in Poisson distribution) comparably in soft and hard energy levels. However, such a typical outburst cannot guarantee whether it is spectrally normal or not. Spectrally, a normal outburst is characterized by a particular transition track, i.e. HS→HIMS→SIMS →SS→SIMS→HIMS→HS, without a flip or a repeat of any of these four states (see Fig. 3.6). We have already noticed that all five outbursts (OB1 to OB5) of GX 339-4 are normal. Appearance of an extra SS or HS in the Θ-curve, however, would imply an *anomaly* via a multiplicity (twin, trine, etc.) in the outburst. For example, the OB in XTE J1550-564 is clearly a twin outburst, due to an interim HS/HIMS (at $\sim 80d$ from MJD 51060) in its Θ-behaviour in Fig. 3.5(VII) and two-fold hysteresis loop (typical track with a triangular loop when $-1.5 < \Theta < -1$) in Fig. 3.10f. This is clearly evident from two distinct peaks in lightcurves also (Fig. 3.8(b1)). However, lightcurves may not always reveal such an anomaly and sometimes show a misleading peak appearance. To see such a possibility, we consider OB2

Table 3.1: Classification of Normal Outbursts: OB-I & OB-II
(Ghosh & Chakrabarti 2018; Ghosh 2018)

OB-I Type Outburst		OB-II Type Outburst
Both soft and hard fluxes change in a similar manner throughout the duration and peak at the same time.	1.	During the rising phase hard flux increases faster and, visibly, peaks earlier than the soft flux in the lightcurves.
The lightcurves and Θ-curve are roughly symmetric about the peak (SS).	2.	The lightcurves and Θ-curve are not symmetric about the peak (SS).
The duration of the rising phase is comparable to that of the declining phase.	3.	The declining phase is few times longer than the rising phase.
Θ, along with CE, fluctuates rapidly about its mean HS-value ($\Theta_{HS} \sim 0$) along a broad plateau at the commencement before dropping quickly to its lowest value in SS ($\Theta \to -1$).	4.	Fluctuations in Θ (and CE) are less along a narrow plateau in the HS, where $\Theta \geq 0$, whence Θ increases steadily to its highest value of $\Theta_{hi} \sim 0.5$ (*harder* state) before falling off to its lowest value.
CENBOL may be collapsed.	5.	CENBOL may be inflated.
Arrival time delay $\tau_r \sim 0d$.	6.	Arrival time delay $\tau_r \gg 0d$.
Accumulation radius $X_a > X_s$ is nearby.	7.	Accumulation radius $X_a \gg X_s$ is afar.
Disk is small.	8.	Disk is big.
Hysteresis is negligible.	9.	Hysteresis is strong.
Accreted matter may result in outflows (or, sometimes, jets).	10.	Accreted matter would disappear into the black hole.

of GRO J1655-40 with a close watch at Figs. 3.5(X) & 3.10e: An extra HS at $\sim 100d$ from MJD 53410 in its Θ-curve and a two-fold loop (typical loop with a marginally separable island at $\Theta < -1$) indicate an anomaly. Its lightcurves in Fig. 3.8(d1), however, show the peak outburst at $\sim 100d$ which manifestly contradicts our previous observation of HS at the same instant. However, both can be explained. Before $\sim 50d$, both soft flux ($\sim 50\ counts.cm^{-2}.s^{-1}$) and hard flux ($< 100\ counts.cm^{-2}.s^{-1}$) were comparable and peaked already resulting in an SS, and thereafter continued to rise similarly until near $\sim 100d$. Then, suddenly the hard flux increased at a higher rate than the soft flux and hardened the spectrum causing a temporary HS at $\sim 100d$. So, the first outburst ended here and, following a quick fall in the hard flux (comparable to the soft flux as before), the next one started. Thus, strictly speaking, the OB in XTE J1550-564 is a *normal twin* while OB2 of GRO J1655-40 is an *anomalous twin.* However, we have ignored this simple anomaly in Table 3.2. As two out of ten outbursts appear to be twins, such an outburst can be very common and is worth reasoning from physical points of view with the help of TCAF.

Explanation for a Twin Outburst from TCAF: A normal outburst originates from the matter piled up at a particular accumulation radius $X_a > X_s$ as it is the most ideal situation for which the corresponding Θ-behaviour will be like that of Fig. 3.6 in terms of the shape the curve and the order of spectral states along it. But, this does not mean that accreting matter will have to be accumulated in a unique annular region around X_a in order to satisfy this requirement. It is quite natural to consider two accumulation radii at $X_{a1} > X_s$ and $X_{a2} \gg X_{a1}$ as the viscosity can vary both spatially and temporally. When the first bulk of matter from X_{a1} reaches X_s, the first outburst occurs and later, as soon as it is over, the second bulk of matter from X_{a2} reaches X_s to cause the second outburst. In this case, a normal twin outburst like that in XTE J1550-564 would be possible. On the other hand, if the second bulk from X_{a2} ($> X_{a1}$) reaches X_s before the first bulk is expended completely in the SS, then the sub-Keplerian matter of the second bulk would harden the spectrum of the first outburst temporarily. Belated arrival of the Keplerian matter from X_{a2} would soften the spectrum again. Such a contamination of both bulks of matter would result in an anomalous twin outburst like that we observed in GRO J1655-40.

Several other types of anomaly are possible depending upon where, when and how the matter keeps piling up. However, such anomalies are not generally evident from the lightcurves but can be scanned from the Θ-behaviour alone with a further justification from the hysteresis loop. These are dealt with in the following section.

3.3 Normal and Anomalous Outbursts in H 1743-322

In the preceeding Section, we have seen how outburst events reveal that even if the Keplerian disk rate is increased at the outer radius (r_{out}) the disk matter carrying high angular momentum is unable to move inward when the viscosity is inadequate to transport the angular momentum of the added Keplerian matter. The matter would generally pile up at $r_{in} < X_a \ll r_{out}$ until the flow becomes highly viscous or the accretion rates rise suddenly. As a consequence, a rapid inflow of disk matter triggers an outburst. The resulting spectrum eventually becomes soft due to the arrival of large disk matter at $r_{in} \sim X_s$. In such a situation, the outburst is said to be normal. However, due to a serious lack of sufficient viscosity, an outburst may evolve into

Table 3.2: Arrival Time Lags (τ_r) and Consequent Characteristics during the Outbursts (Ghosh & Chakrabarti 2018; Ghosh 2018)

Transient LMXRB	OB	τ_r (d) (Θ)	τ_r (d) CC(Θ,H/S)	τ_r (d) CC(H,S)	Spectral Nature	Disk Size
4U 1543-47	OB	0	0 ± 1.4	0 ± 1	Normal (OB-I)	Small
XTE J1550-564	OB*	5	1 ± 1.4	0 ± 1	Normal† (OB-I)	Small
XTE J1650-500	OB	10	10 ± 2.8	6 ± 2	Normal (OB-II)	Large
GRO J1655-40	OB2°	5	3 ± 1.4	0 ± 1	Normal† (OB-I)	Small
GX 339-4	OB1	0	0 ± 1.4	0 ± 1	Normal (OB-I)	Small
	OB2	22	19 ± 1.4	0 ± 1	Normal (OB-II)	Large
	OB3	0	1 ± 1.4	0 ± 1	Normal (OB-I)	Small
	OB4	10	7 ± 1.4	3 ± 1	Normal (OB-II)	Medium
	OB5	20	19 ± 4.1	0 ± 1	Normal (OB-II)	Large

$^\circ\tau_r = 0d$ for OB1. *Twin. †Presence of Anomaly. H/S=Hard or Soft (photon fluxes).

either a HIMS/SIMS, or a premature HS thereafter. Such an outburst appears to be *anomalous* or *failed*. When the viscosity parameter (α) rises well above its critical value (α_c) at a large distance, X_a, the disk will become Keplerian till the inner edge and a SS can form. If the viscosity does not rise much, the outburst will be anomalous. α has a specific limit to cross in order to reach a certain spectral state (Mondal et al. 2017).

Nevertheless, both normal and anomalous outbursts can be readily deciphered from temporal and spectral characteristics of two radiative components when linked with the dynamic photon index (DPI), Θ, even though not directly distinguishable from the lightcurves always. We have already seen how Θ successfully detected anomalies from its own behaviour with time and energy (in hysteresis loop) in the form of twin outbursts in XTE J1550-564 and GRO J1655-40. As discussed earlier, more HS/SS(s) in the well-like Θ-curve of Fig. 3.6 indicate the multiplicity (twin, trine, etc.) of the outburst, or the number of *mini outbursts*. If any outburst shows subtle and significant deviations of Θ-behaviour from that of Fig. 3.6, then we identify that outburst as *anomalous*. Such anomalies will be evident from the hysteresis loop in the form of a complex loop comprising multiple loops for multiple mini outbursts. Otherwise, a single and simple closed loop implies a normal outburst as usual.

In order to see various anomalies together in a single transient LMXRB, we consider H 1743-322. This is an enigmatic source as it remained quiescent for about a quarter of a century

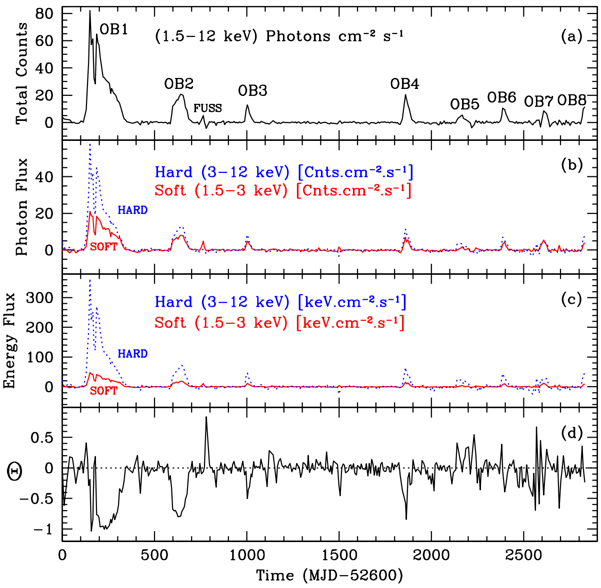

Figure 3.12: H 1743-322: All time series are drawn with weekly average data to clearly represent (a) total photon counts, hard & soft fluxes of (b) photon and (c) energy, and (d) Θ. Eight successive outbursts are marked in (a) as OBn, where n=1, ..., 8. OBs are manifested by the distinct wells in (d). A flare-up SS (FUSS), marked in (a), is also considered for its comparable peak and soft flux to those in all OBs (Ghosh & Chakrabarti 2019).

until its detection in a bright outburst observed in March 2003. This outburst was followed by several others observed through the following decade. Chakrabarti, Debnath & Nagarkoti (2019, hereafter CDN19) have analyzed the X-ray data recorded by a few satellites including RXTE/ASM for about a dozen of successive outbursts in H 1743-322 since 2003. They have shown that the total energy liberated per outburst is proportional to the time elapsed in quiescent state prior to the outburst. The 2003-outburst lasted for an exceptionally long duration and soon after it another outburst occurred in 2004. CDN19 argued that this second outburst should be considered to be associated with that of 2003 in order for explaining the occurrence of other outbursts in H 1743-322 post 2004. Moreover, during its yet another outburst in 2008, the source is reported to have transited from a HS to a HIMS before becoming harder again with decreased luminosity and due to the lack of a proper softening this outburst has been identified as a *failed* (Capitanio et al. 2009) or an *almost successful* (Zhou et al. 2013) outburst. These results motivated us to search for the possibility of the presence of unusual anomalies. Therefore, for detecting such anomalies we consider the first eight successive outbursts of H 1743-322 during 2003-2010 and analyze RXTE/ASM ($1.5 - 12\ keV$) data by our generalized procedure involving the single parameter Θ (Ghosh & Chakrabarti 2019). Instead of taking only the hard and soft photon fluxes, we have used also the hard and soft fluxes of energy carried by them. However, the responses of Θ to the fluxes of either photons or energy have been observed to be similar.

3.3.1 RXTE/ASM Observation of 8 Successive Outbursts in H 1743-322

Figure 3.12 shows the long-term (MJD $52720 - 55435$) behaviour of H 1743-322 in terms of (a) total photon flux, (b) hard (dotted/blue) & soft (continuous/red) photon fluxes, (c) average

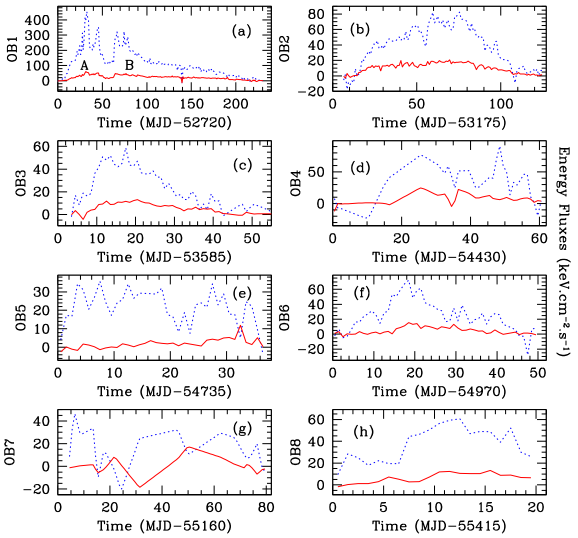

Figure 3.13: Average hard (dotted/blue) and soft (continuous/red) energy fluxes during the first eight outbursts in H 1743-322 since 2003 are zoomed by the use of daily average data. Two parts showing two peaks in OB1 are indicated as A & B in (a). The difference of behaviour between soft and hard fluxes in OB4, OB5, OB7 & OB8 is likely to be due to some anomalies (Ghosh & Chakrabarti 2019).

hard (dotted/blue) & soft (continuous/red) mean energy fluxes (i.e. intensities of the photon fluxes) and (d) the DPI Θ. All the time series in Fig. 3.12 are plotted with weekly-mean data for clarity. Eight successive outbursts are marked in (a) as OBn, where n=1, ..., 8, for identifying them as OB1 to OB8. The calendar year of each outburst is written in Table 3.3. A *flare-up soft state* (FUSS) in 2004 is marked in Fig. 3.12a. It was not recognized as an outburst or otherwise. But it is considered for our analysis in the same vein of the outbursts because its peak counts and total amount of soft flux are comparable to those in all outbursts. The spectral state becomes hard immediately after it. This is evident from the sharpest peak (∼ MJD 53375) in Θ from Fig. 3.12d. The outbursts of Fig. 3.12c are zoomed with daily average energy data in Fig. 3.13. Two peaks of the brightest outburst OB1 (of 2003) are marked as A & B in Fig. 3.13a. Several outbursts are different in character in terms of the time evolution of the soft and the hard energy curves. The numerical findings of our analysis and their physical implications (Ghosh 2018; Ghosh & Chakrabarti 2019) are summarized in Table 3.3, which reflects the transient trend in H 1743-322.

3.3.2 Estimation of Time Lags (τ_r) from Θ-Behaviour

Figure 3.14 shows the behaviour of Θ with time during all eight outbursts indicated as OB1 to OB8 serially along the vertical axes. The dotted/red curves are drawn to represent average envelopes of Θ for comparing them with the ideal Θ-behaviour of Fig. 3.6. Θ attains its highest value (> 0), due to the lag-dependent extra spectral hardening as described earlier, about two weeks to a few days after the commencement of the outbursts OB1, OB3 & OB5-OB8 as seen in Figs. 3.14a, 3.14c & 3.14e-h respectively. These estimated time lags ($\tau_r > 0d$) from Θ are marked. Both OB2 & OB4, unlike others, lack any extra spectral hardening over and above

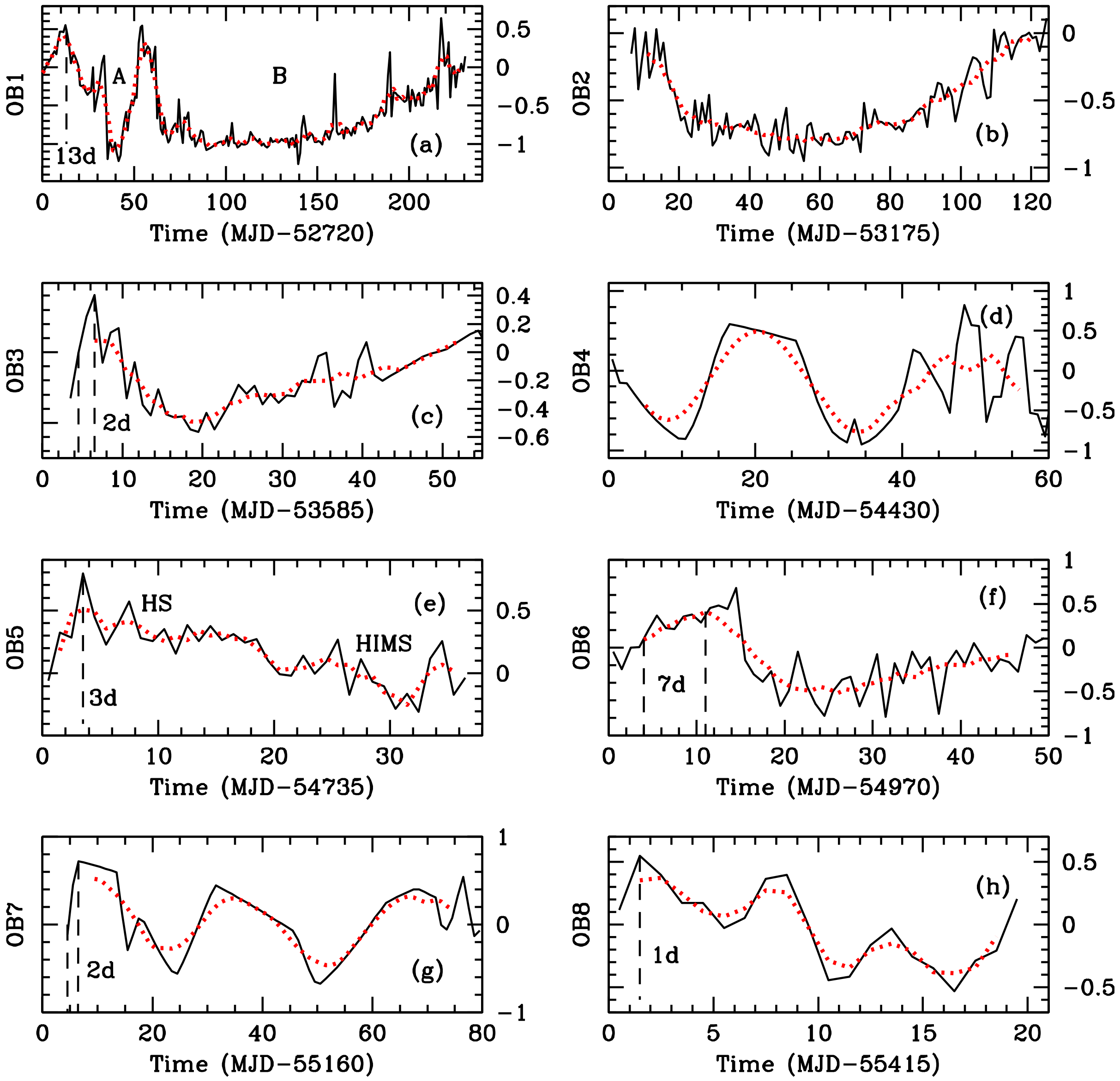

Figure 3.14: Behaviour of Θ with time during all outbursts of Fig. 3.13 is drawn in black/continuous with the average daily data. Dotted/red curves represent the average envelopes for a comparison with the ideal diagram of Θ in Fig. 3.6. Θ drops down from its gradually attained highest value following the commencement of the normal outbursts OB2, OB3 & OB6 and anomalous OB1-A in (b), (c), (f) & (a) respectively and rises again at the end; whereas, its features are deviated in (d) OB4, (g) OB7 & (h) OB8. The trend in Θ is declining throughout in (e) OB5 and a comparison with Fig. 3.6 readily indicates a direct HS→HIMS spectral transition and a further hardened spectrum at the end of this *failed* outburst, whereas in view of (c) & (f) it is an *almost successful* outburst. More than one well in (a) indicates the multiplicity in OB1 or *mini* outbursts in OB4, OB7 & OB8. Estimated τ_rs $(> 0d)$ are marked (Ghosh & Chakrabarti 2019).

the generic HS at their beginning.

3.3.3 Detection of Anomalies from Θ-Curves

However, OB5 (in 2008), as seen from Fig. 3.14e, could not manifest as an outburst like OB2 or OB3 despite have similar beginning. Θ decreased only toward the end of OB5 and missed the expected SS or the peak. With reference to Fig. 3.6, a direct HS→HIMS spectral transition followed by a further hardening at the end of this *failed* outburst (Capitanio et al. 2009) are indicated, whereas in view of Figs. 3.14c & 3.14f OB5 appears to be as an *almost successful* (i.e. almost normal) outburst (Zhou et al. 2013). No other reports of any such anomaly are available in the literature. Let us identify several other anomalies in the other outbursts of H 1743-322.

In view of both Fig. 3.13a & Fig. 3.14a, OB1 is a twin outburst characterized by two SSs. Although OB1-A could itself be a twin due to an interim temporary HS and is anomalous due to an unusual spectral transit. But OB1-B is normal and is comparable to OB2, OB3 & OB6 of Figs. 3.14b, 3.14c & 3.14f which are also normal. However, features of Θ, in comparison with Fig. 3.6, are deviated in Fig. 3.14d for OB4, Fig. 3.14g for OB7 & Fig. 3.14h for OB8. Erratically fluctuating Θ is due to multiple number of *mini outbursts*, indicated by multiple wells in dotted/red curves, where each constituent small well separately conforms with the ideal Θ-behaviour of Fig. 3.6. Each of these wells is characterized by its own SS (or SIMS) and represents a mini outburst. The multiplicity is also apparent from the number of troughs contained in the Θ-well, i.e. there can be three mini outbursts in OB4 while two mini outbursts in both OB7 & OB8. Therefore, there is a flipping and the recurrence of the spectral states in the same outburst enveloping the mini outbursts. However, the energy curves (i.e. the lightcurves scaled with mean photon energy) of Figs. 3.13d, 3.13g & 3.13h do not clue in about the recurrent spectral transition happened respectively in OB4, OB7 & OB8.

3.3.4 Determination of Time Lags (τ_r) from CC(Θ, Hard) & CC(Θ, Soft)

We have seen earlier that the commencement of an outburst in HS does not ensure an immediate spectral transition to an intermediate state (HIMS/SIMS), the spectrum becomes initially harder instead. As the halo matter rushes in, the photons become spectrally harder with more electrons to cool down. This is due to the fact that the source of soft photons, i.e. the disk matter, has not yet arrived at $r_{in} \sim X_s$. The time interval between the attainment of the hardest state and the beginning of the outburst in HS is the time lag, τ_r, already estimated from Θ-behaviour in Fig. 3.14. However, these time lags are not usually observed from a direct coorrelation between the hard flux and the soft flux, i.e. CC(Hard,Soft), but can be computed

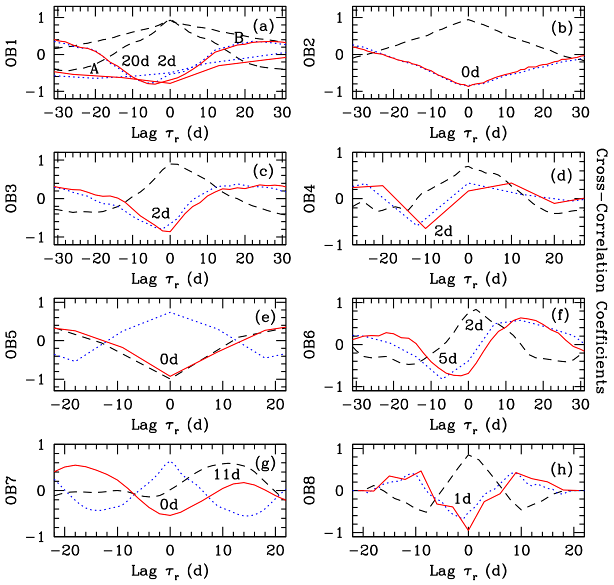

Figure 3.15: CC(Θ, Hard), CC(Θ, Soft) & CC(Hard, Soft) are represented respectively by dotted/blue, continuous/red and dashed/black curves. Time lags are marked. A & B regions of OB1 are analyzed separately in (a). OB5 & OB7 are different from the rest: fluxes are anti-correlated with Θ. OB1 in (a) shows $\tau_r = 20(\pm 8)d$ (consistent with $13d$ from Θ) while the lags are negligibly small in subsequent OBs (Ghosh & Chakrabarti 2019).

by the time difference between the peaks of CC(Θ, Hard) and CC(Θ, Soft) curves resulted from the correlation of both fluxes with Θ. These CC-profiles are shown in Fig. 3.15. Two regions A & B of Figs. 3.13a & 3.14a are used separately in Fig. 3.15a. Time lags are marked in all boxes.

A lag time of about a week as a Θ-estimate, indicated in Fig. 3.14f for OB6, is in agreement with the outcome of $5(\pm 3.5)d$ obtained from the CCs with Θ in Fig. 3.15f. Similarly, a lag of about two weeks in Fig. 3.14a for OB1 is justified by $20(\pm 8)d$ from Fig. 3.15a. So, our previous estimates of lags from Θ-behaviour alone are proved to be correct. We have simplified all the complex outbursts of H 1743-322 by our *spectro-temporal* index Θ which indeed dynamically traces each outburst at each instant in terms of both spectral and temporal features.

Figs. 3.15e & 3.15g for OB5 and OB7 are different from the rest as hard flux is anti-correlated with respect to soft flux (OB5) and Θ (OB7). Both implies a lack of proper softening in their rising phases. An exceptional lag of $11d$ in Fig. 3.15g for OB7 from the direct CC(Hard, Soft) may be due to either the fact that fresh incoming matter with the leftover of OB6 increased the hard flux, or a jump in Comptonizing efficiency following a sudden increase in accretion rates. This lag is actually $\tau(\Theta_{hi})$ as discussed in §3.2.3. This time interval is readily evident from Fig. 3.14g by an almost flat bump with $\Theta_{hi} \sim 0.6$ spanning over $\sim 10d$ which is roughly equal to the time for which the hard flux maintains more or less its peak counts as seen from the energy curves in Fig. 3.13g. A similar lag of $\tau(\Theta_{hi}) \sim 5d$ is implicit in OB8 also (Figs. 3.13h & 3.14h). This evidence also ensures that a fast increase in hard flux does not guarantee a spectral transition.

Although the brightest outburst in Fig. 3.15a shows a time lag of $20(\pm 8)d$ for OB1-A

(2003), but the lags are negligibly small in the subsequent weaker outbursts.

3.3.5 Confirmation of Anomalies from Hysteresis Loops

In Fig. 3.16, the mean intensity in all the outbursts of Fig. 3.13 is plotted with Θ of Fig. 3.14. However, running average data are used for clarity and comparison. Time lags obtained in Fig. 3.15 are marked along the vertical axes. Closed *hysteresis loops* in Figs. 3.16b-c & 3.16f respectively justify that OB2, OB3 & OB6 are normal outbursts. These agree with the Θ-behaviour in Figs. 3.14b-c & 3.14f respectively. The closed loop in Fig. 3.16e indicates that OB5 (observed in 2008) could almost be a normal outburst which lacks a proper softening as $\Theta > -0.3$ and this agrees with an earlier finding (Zhou et. al 2013). This failure or an anomaly in OB5 is more directly evident from our analysis.

However, the number of closed loops pertaining to any outburst in Fig. 3.16 corresponds to the number of constituent wells in Θ (Fig. 3.14). Both consistently indicate either the number of *mini outbursts* or the multiplicity present in it. Therefore, OB4, OB7 & OB8 are identified as anomalous outbursts. The excursion track is erratic as seen respectively from Figs. 3.16d, 3.16g & 3.16h. The multiplicity is also apparent from the folded loops, i.e. there are three mini outbursts in OB4 while two mini outbursts are contained in both OB7 & OB8.

Loops in solid and dotted/red in Fig. 3.16a show the hysteresis property of OB1-A & OB1-B respectively. OB1 is a twin outburst, though OB1-A itself is complex showing an anomaly and is itself a twin due to a two-fold loop, arisen due to the presence of an interim but momentary HS (see Fig. 3.14a). However, OB1-B is similar to OB2 of Fig. 3.16b and both are normal. OB1-A or, OB1 as a whole, may be compared with the twin outburst of XTE J1550-564 observed earlier in terms of both Θ-behaviour and hysteresis loop.

3.3.6 Flare-Up Soft State (FUSS) in 2004: A Missed Outburst

Figure 3.17 shows (a) energy fluxes, (b) Θ, (c) CC-profiles and (d) hysteresis diagram of the FUSS occured immediately following OB2 in 2004. Line types or colour stamps in Fig. 3.17 are same as before. The magnitude of soft flux in (a) is comparable with those in all outbursts. FUSS is also showing a striking excursion path in (d). The lumpy behaviour of Θ and hysteresis diagrams in Figs. 3.14d, 3.14g & 3.14h and Figs. 3.16d, 3.16g & 3.16h indicate that OB4, OB7 & OB8 are comparable and almost similar to FUSS. Due to a lack of hard flux during its peak it was quite possibly a missed outburst which went unnoticed by all before us. CDN19 have shown that OB2 could partially release energy from the disk matter accumulated during the long quiescence prior to OB1 in 2003. Similarly, FUSS can also arise from the surplus disk matter of OB2 (Ghosh & Chakrabarti 2019).

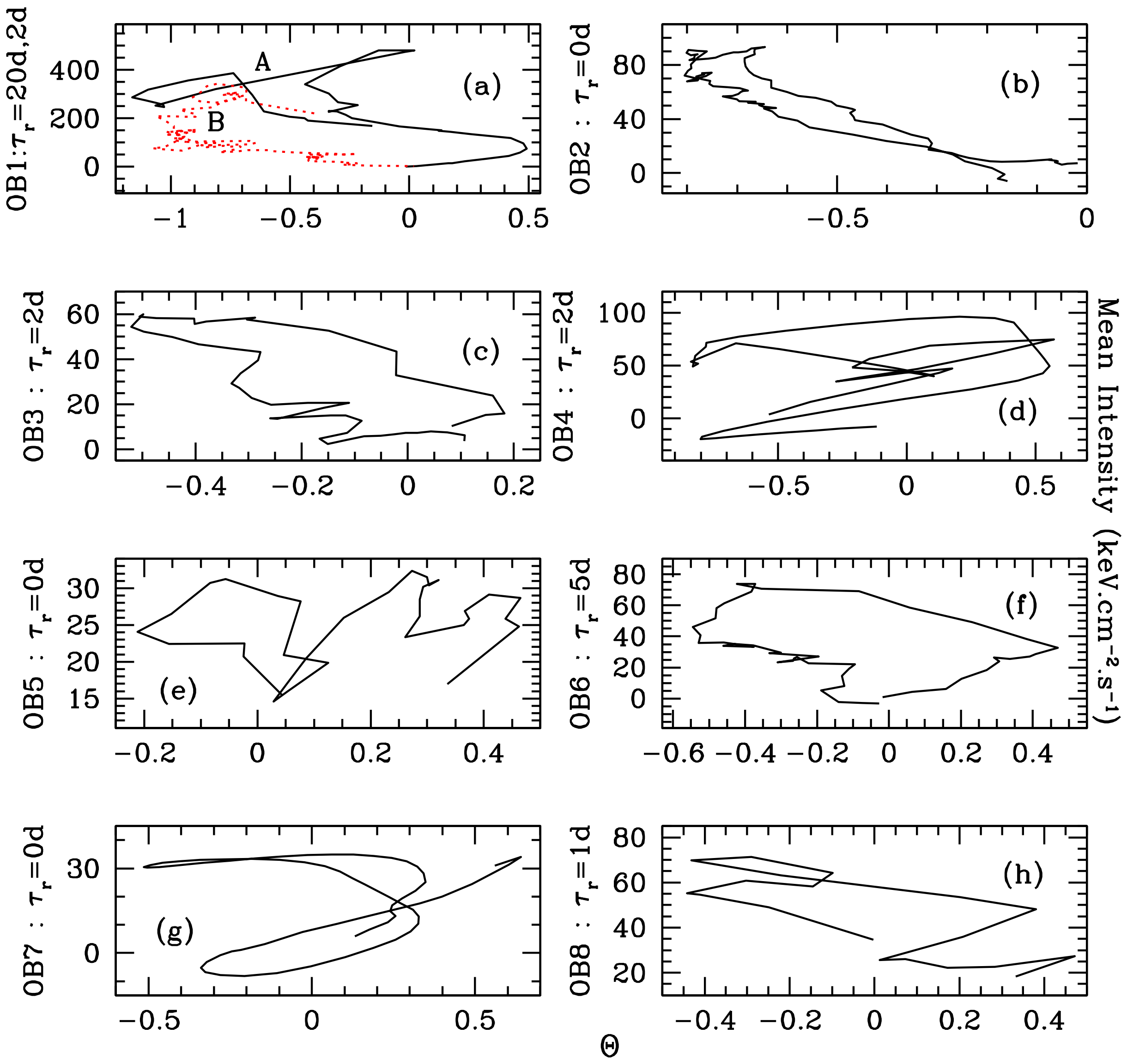

Figure 3.16: *Hysteresis loops* for outbursts in H 1743-322:- Running-average data are used for clarity and comparison. Time lags are marked along the vertical axes. Closed loops in (b), (c) & (f) are indicating normal outbursts. 2-fold loop for OB1-A as well as dotted/red loop for OB1-B (comparable to the normal OB2 in (b)) in (a) indicate a twin (if not a trine) outburst OB1. This is an anomalous outburst altogether. For other anomalous outbursts, excursion path becomes erratic or folded (indicating multiple *mini outbursts*) as seen in (d), (g) & (h). The situation is marginal for the *almost successful / failed* outburst OB5 in (e). The biggest loop area in (a), which is consistent with the corresponding longest time lag ($\tau_r = 20(\pm 8)d$), indicates the largest disk size in the brightest outburst OB1-A in H 1743-322. Small loop areas and short τ_rs all subsequent outbursts are indicative of small sizes of the Keplerian disk or nearby accumulation radii, X_as (Ghosh & Chakrabarti 2019).

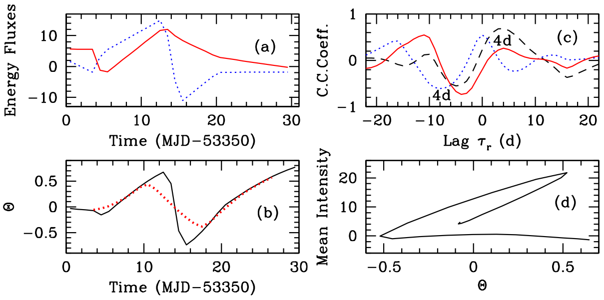

Figure 3.17: Flare-up SS (FUSS): (a) Two energy fluxes, (b) Θ, (c) CC-profiles and (d) hysteresis loop. Line types or colour stamps are the same as before. $\tau_r = 4d$ is evident from all CCs and Θ (Ghosh & Chakrabarti 2019).

3.3.7 Waning Accretion Disk in H 1743-322

Due to the viscous time required to transport matter inward, a farther piling radius X_a implies a greater arrival time lag τ_r. We see that τ_r in the brightest outburst OB1 of H 1743-322 is longer than that in each of its subsequent outbursts occured with decreasing brightness. The biggest loop area in Fig. 3.16a is also consistent with this highest value of $\tau_r = 20(\pm 8)d$ (see Fig. 3.15a and Table 3.3). This means that the disk size in OB1 is the largest of all. This result is consistent with the preceding long time quiescence of the source when X_a was at the farthest distance (CDN19). Negligibly small lags in all subsequent outbursts indicate small Keplerian disks.

H 1743-322 remained in pre-outburst quiescent phase for about 25 years until 2003, when a complex outburst, OB1, occurred releasing a large amount of energy and lasted for 230d (MJD $52720 - 52950$). OB1 is a twin outburst comprising an anomalous OB1-A and a normal OB1-B. Again in 2004, another outburst, OB2, occurred. OB2 is a normal outburst for which X_a was very close to the outer edge of the CENBOL because of 0d time lag. This justifies the argument of CDN19 that OB2 caused due to the effect of a leftover of the energy that should have been emitted in OB1. Thereafter, outbursts were occurring regularly and releasing a little energy compared to that of OB1. FUSS, a *mini outburst* or a *flare*, occurs immediately after OB2. OB3 is a normal outburst which is followed by two consecutive anomalous outbursts, OB4 & OB5, preceding the next normal one, OB6. OB7 is once again anomalous and is followed by yet another anomalous outburst, OB8. Therefore, every normal outburst in H 1743-322 appears to be either followed or preceded by one or more premature outbursts showing various anomalies in spectral transition (Ghosh & Chakrabarti 2019). Along with these eight outbursts during 2003-2010, CDN19 have considered several others post 2010 to show that the amount of energy release per outburst is directly proportional to the duration of the quiescent phase prior to it.

It seems that not all the matter piled up in the preceding quiescence was always emptied out at the outburst, i.e., the disk was not exhausted totally. Thus, once high viscosity phase was over, multiple attempts (as in 2004 via OB2 and FUSS) were made to evacuate the matter

Table 3.3: Time Lags (τ_r) and Consequent Features of Successive Outbursts in H 1743-322 (Ghosh 2018; Ghosh & Chakrabarti 2019)

Calendar Year	Outburst No.	τ_r (d) (Θ)	τ_r (d) CC(Θ,H/S)	τ_r (d) CC(H,S)	Spectral Nature	Disk Size
2003	OB1 (A)	13 (Longest)	20 ± 8	0 ± 1	Anomalous (Brightest)	Largest
	OB1 (B)	2	2 ± 1.4	0 ± 1	Normal (OB-I)	Small
2004	OB2	0	0 ± 1.4	0 ± 1	Normal (OB-I)	Small
2004	FUSS†	4	4 ± 1.4	4 ± 2	Anomalous	Small
2005	OB3	2	2 ± 1.4	0 ± 1	Normal (OB-II)	Small
2007-8	OB4	0	2 ± 7.8	0 ± 1	Anomalous	Small
2008	OB5	3	0 ± 6.4	0 ± 7	Anomalous	Small
2009	OB6	7	5 ± 3.5	2 ± 1	Normal (OB-II)	Medium
2009-10	OB7	2	0 ± 1.4	11 ± 1	Anomalous	Small
2010	OB8	1	1 ± 3.2	0 ± 2	Anomalous	Small

†Flare Up Soft State (mini outburst). H/S=Hard or Soft (photon energy fluxes).

to recover that phase again. In doing so, the accumulation of matter took place at gradually decreasing radii X_as approaching toward the inner region close to X_s or r_{in}.

However, there could be another possibility that the large accretion disk, which was formed in the course of two and half decades till 2003, was not at all dissipated totally in any of the outbursts. Instead, the disk remnant at the end of any preceding outburst was enhanced by fresh incoming matter during the quiescent phase and the disk was formed for the following outburst. From Figs. 3.12a-c we see an overall declining trend in terms of the decay in the fluxes of photons or energy (hard, soft and total) from OB1 to OB3 and from OB4 to OB8. The quiescent phase between OB3 and OB4 lasted for about $850d$, which was longer than other such interim phases ($< 300d$) in all consecutive pairs. As a consequence, the photon fluxes clearly increased much in OB4 (compared to OB3) by the significant enhancement in seed photons due to the fresh disk matter added to the disk remnant of OB3. Therefore, the seven outbursts, OB2 to OB8, could be supposed as the *aftershocks* of OB1. It is unrealistic to think that the disk formed slowly in 25 years before OB1 could be disappeared fully in a few years.

3.4 Comparison between GX 339-4 and H 1743-322

We have aleady seen (in §3.1.9 and Table 3.2) that all five successive outbursts (OB1 to OB5) in GX 339-4 are normal outbursts with Keplerian disks of various sizes (Ghosh & Chakrabarti 2018). On the other hand, in H 1743-322, following its brightest outburst OB1 occurred in 2003, every normal outburst is either followed or preceded by an anomalous outburst (Ghosh & Chakrabarti 2019). In fact, OB1 itself comprises an anomalous twin outburst and a normal outburst following it. Four out of seven outbursts post 2003 have been detected by us to be anomalous. Therefore, both sources are worth comparing with each other in terms of their similarities and differences. In this section, first we pick the first five outbursts (OB1 to OB5) of H 1743-322 since 2003 to 2008 and the five outbursts (OB1 to OB5) of GX 339-4 observed during 1997–2010 in order to compare these two sources with multiple outbursts on the basis of long-term transient behaviour (Ghosh 2018). Second, from the available reports in the literature, we shall incorporate the mass accretion rates computed from the TCAF-fitting of short-term RXTE/PCA ($2.5 - 25\ keV$) data for a couple of outbursts in both sources and emphasize some other issues in comparison with our results. At the end of the section, we shall outline how all outbursts of all transient sources can be studied universally by our single parameter, DPI or Θ, and explained accurately with TCAF in hand.

3.4.1 Long-term Behaviour of 5 Successive Outbursts (OB1 to OB5)

In Fig. 3.18, the total mean energy values of both hard and soft photons (i.e. intensity) during the successive five outbursts (OB1 to OB5) in each of (*top*) GX 339-4 and (*bottom*) H 1743-322 are represented by histograms, drawn along the vertical axis by blue/dashed and red/continuous bars. Calendar year of the outburst event is labelled on each histogram. The ratio of soft intensity to hard intensity in each outburst (OB) is always a fraction (< 1). The dotted curve joins these ratios (represented by triangles) for all OBs on a (0,1) scale. Equal bar width of the histograms is not to scale, and so, has nothing to do with the outburst duration. However, each triangle on the dotted curve indicates the mid-point of each outburst along the horizontal time axis.

First of all, it should be noted that the five OBs of GX 339-4 occurred in about 13 years while H 1743-322 exhibited its five OBs in about 5 years only. Soft photon intensity varies within a range of $27\% - 35\%$ of the hard photon intensity of the OBs in the former source, whereas, this range is only $10\% - 27\%$ in the latter. The intensity of total hard photons per outburst in GX 339-4 is readily observed to lie between $\sim 15\ MeV.cm^{-2}.s^{-1}$ (OB4) and $\sim 48\ MeV.cm^{-2}.s^{-1}$ (OB2). On the other hand, the intensity of total hard photons is the

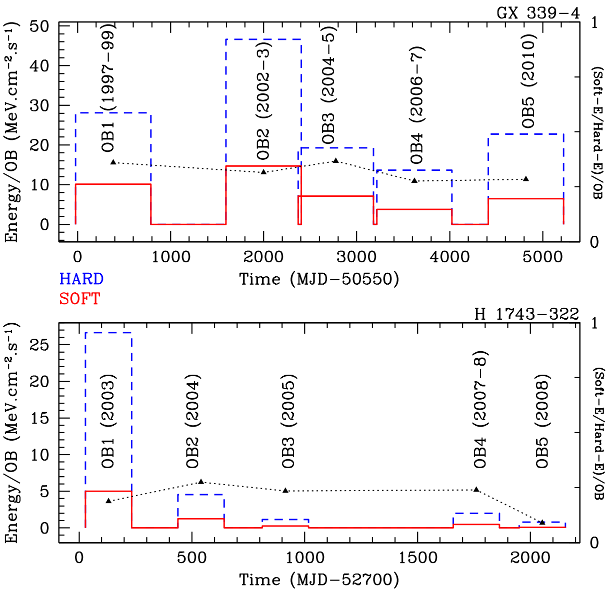

Figure 3.18: *Histograms* are drawn with total mean hard (blue-dashed) and soft (red-continuous) intensity in successive 5 OBs of (*top*) GX 339-4 & (*bottom*) H 1743-322. Equal bar width is not to scale. Triangles (central points of OB1-OB5) indicate soft-to-hard energy ratio on a (0,1) scale. The quiescent time elapsed between any two consecutive outbursts is responsible for an increase in brightness in the latter (Ghosh 2018).

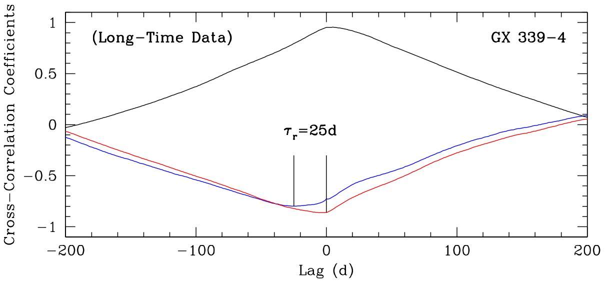

Figure 3.19: GX 339-4: CC-curves of soft & hard photon fluxes and Θ, using untruncated daily data (in Fig. 3.3(a)) comprising all 5 OBs, are drawn. $\tau_r = 25d$ indicates the general tendency of a leading sub-Keplerian flow.

highest ($\sim 27\ MeV.cm^{-2}.s^{-1}$) in OB1 of H 1743-322 and lowest in OB5 ($\sim 1\ MeV.cm^{-2}.s^{-1}$) while this does not exceed $\sim 5\ MeV.cm^{-2}.s^{-1}$ for the rest three OBs in between. All these estimates from Fig. 3.18 prove that OB1 is the brightest while the subsequent four outbursts are unusually fainter in H 1743-322 and, as far as luminosity is concerned, only OB1 of H 1743-322 is comparable to any of OB1–OB5 in GX 339-4. Brightness of the pairs, OB1 & OB5, and OB3 & OB4, is similar. Also, OB1 & OB5 are comparable to the so-called brightest OB1 of H 1743-322 while OB2 of GX 339-4 is two times more luminous. CDN (2019) have shown from a rigorous long-term analysis with X-ray data of a few satellites including RXTE/ASM for more than a dozen of outbursts in H 1743-322 that the luminosity of any outburst is almost proportional to the preceeding time of quiescence. This appears to be true in GX 339-4 also and could be a basic transient property. From Fig. 3.18 it is clearly visible in GX 339-4 that the brightness of OB2 (or OB5) has increased a significantly as compared to preceeding OB1 (or OB4) separated by a commensurate quiescent time interval. For H 1743-322 also, a significantly long quiescent period following OB3 must have been instrumental behind brighter OB4, breaking the declining transient trend of the source.

3.4.2 Variation in Accumulation Radii, Time Lags and Accretion Disks

The common feature of a proportionality between the quiescent time prior to an outburst and its brightness in both GX 339-4 and H 1743-322 means that a farther accumulation radius X_a gives rise to a longer quiescence or a longer arrival time lag τ_r. However, the converse is not necessarily true. X_a, in general, varies from one outburst to the other and so, it can go far away from or come closer to the CENBOL. Having a quick look at Table 3.2 given in §3.1, we see that τ_r is negligibly small ($\sim 0d$) for OB1 & OB3 while it is about three weeks for OB2 & OB5 in GX 339-4; $\tau_r \sim$ a week in OB4. If $\tau_r = 0d$ sets a lower critical limit to X_a, then there could be an upper critical limit of X_a determining the maximum τ_r with which the sub-Keplerian halo would lead ahead of the Keplerian disk as a general tendency in a transient LMXRB exhibiting outbursts frequently. However, such limits are also possible in other transient sources showing sporadic outbursts. To see such a possibility, we consider long-term ($5000d$) untruncated lightcurves of daily average soft and hard photon fluxes (as in Fig. 3.3(a)) comprising all five OBs of GX 339-4 and the quiescent time intervals therein and cross-correlate them with Θ. Figure 3.19 shows these CC-curves resulting in $\tau_r = 25d$, i.e. about three to four weeks. This outcome is also similar to the highest time lag, $\tau_r = 20(\pm 8)d$, i.e. about two to four weeks, observed in H 1743-322 for its OB1. Thereafter, X_a moves in closer as the subsequent τ_r's are either negligible or less than about a week.

Accumulation radii represent the sizes of the Keplerian disks in multiple outbursts of both GX 339-4 or H 1743-322. Therefore, varying disk sizes are obvious in the five outbursts of GX 339-4. However, in H 1743-322, the largest disk was formed before OB1. All its subsequent outbursts followed either from the disks of waning size or from a singular waning disk, which dissipated itself by parts by enhancing its disk from fresh viscous matter during quiescent phases. Nevertheless, both temporal and spectral properties are more or less similar during the consecutive five normal outbursts of GX 339-4 even though the disk size increases or decreases from one to the other (Ghosh & Chakrabarti 2018) while H 1743-322 has shown several anomalies (Ghosh & Chakrabarti 2019) during its most outbursts. Their unusual temporal and spectral properties are due to the effect of influence of decreasing sizes of the Keplerian disk.

3.4.3 Time Lags from Lightcurves and Accretion Rates

In §3.1.3, §3.1.5 and §3.2.4, we have explained the possible circumstances of detecting time lags from lightcurves (τ_{lc}) or from mass accretion rates ($\tau_{\dot{m}}$). Without any reiteration, we state here that $\tau_{lc} \approx \tau_{\dot{m}} \approx \tau(\Theta_{hi})$ (see Eq. 3.2). Note that $\tau(\Theta_{hi})$, as an exception, becomes relevant only when $\tau(\Theta_{HS} \rightarrow \Theta_{hi})$ exists (i.e. for OB-II type outbursts). But $\tau_r \gg 0d$ cannot ensure the detection of $\tau(\Theta_{hi})$ unless $\Theta = \Theta_{hi} > 0$ is maintained well above $\Theta_{HS} \approx 0$ and the hard flux roughly holds its highest value about its blunt peak for a significant time ($\sim$ a week or more) even after the initial extra spectral hardening (HS→harder state transition) of a given outburst. We observed this feature in the sporadic outburst of XTE J1650-500 also (§3.1).

To see such an effect in GX 339-4 and H 1743-322, first we revisit OB5 of GX 339-4 in Fig. 3.20, where the rising phase of this outburst is zoomed with the lightcurves of hard and soft photon fluxes and CE (with the same vertical axis scale but ignoring the unit for the fluxes) from RXTE/ASM daily mean data in (a). Debnath, Mondal and Chakrabarti (2015) fitted the spectra of OB5 (2010) with TCAF using RXTE/PCA ($2.5 - 25$ keV) data and extracted the mass accretion rates, $\dot{m}_{disk}$ & $\dot{m}_{halo}$, among other things. Figure 3.20b shows the behaviour of $\dot{m}_{disk}$, $\dot{m}_{halo}$ and accretion rate ratio, ARR$=\frac{\dot{m}_{halo}}{\dot{m}_{disk}}$ (exploiting the same vertical scale but ignoring the unit for the rates) in the rising phase of OB5. Two rates are correlated and the CC($\dot{m}_{halo}$, $\dot{m}_{disk}$) profile is shown in Fig. 3.20c. Let us recall, from Fig. 3.7(e2), the fact that CC(Hard, Soft) gives $0d$ lag as usual while CCs with Θ indicate $\tau_r = 19d$. However, from Fig. 3.20a, it is clearly seen that the hard flux peaks $6d$ earlier than the soft flux and more or less maintains its counts around a blunt peak until the latter achieves its peak. In such a case, we interpret the peaking time difference in their lightcurves as $\tau_{lc} = 6d \approx \tau(\Theta_{hi})$. Similarly, we can expect this lag to be estimated from the time interval between $\dot{m}_{disk}$ & $\dot{m}_{halo}$, which are controlling the photon fluxes. This is evident from Fig. 3.20b that $\tau_{\dot{m}} = 7d \approx \tau(\Theta_{hi})$ (Ghosh, Banerjee & Chakrabarti 2019). As soon as $\dot{m}_{halo}$ peaks and starts dropping fast both ARR and CE have decreased from their highest values towards the lowest ones in consistent with Θ (see Fig. 3.7(e1) shown earlier or Fig. 3.22(a5) drawn later). Meanwhile, the hard flux retains its peak (~ 25 $counts.cm^{-2}.s^{-1}$) until the soft flux achieves its own stable peak a week later.

We can check from Fig. 3.7(e2) that CC(Hard, Soft) gives an asymmetric peak at $0d$ because both fluxes rise or fall similarly at almost all instants, showing a linear dependence. But, we see from Fig. 3.20c that CC($\dot{m}_{halo}$, $\dot{m}_{disk}$) results in a peak at $8(\pm 1)d$ for both the data with interpolation (WI) or without it (WoI). This asymmetric peak, shifted to $8d$, indicates that the nonlinearity is not removed from otherwise independent two accretion rates, which do not vary like the resulting photon fluxes. Nevertheless, all these three estimates consistently give a lag of about a week, which is shorter than the τ_r-value of about three weeks observed in OB5 of GX 339-4 by us earlier in Fig. 3.7(e2). Therefore, τ_r actually comprises the lag obtained here. High τ_r-value also indicates a strong disk hysteresis (big loop area), which requires a long relaxation time for the accretion flow to return into its pre-outburst phase geometry. This is implicit in the broad peak of the CC($\dot{m}_{halo}$, $\dot{m}_{disk}$) curve in Fig. 3.20c.

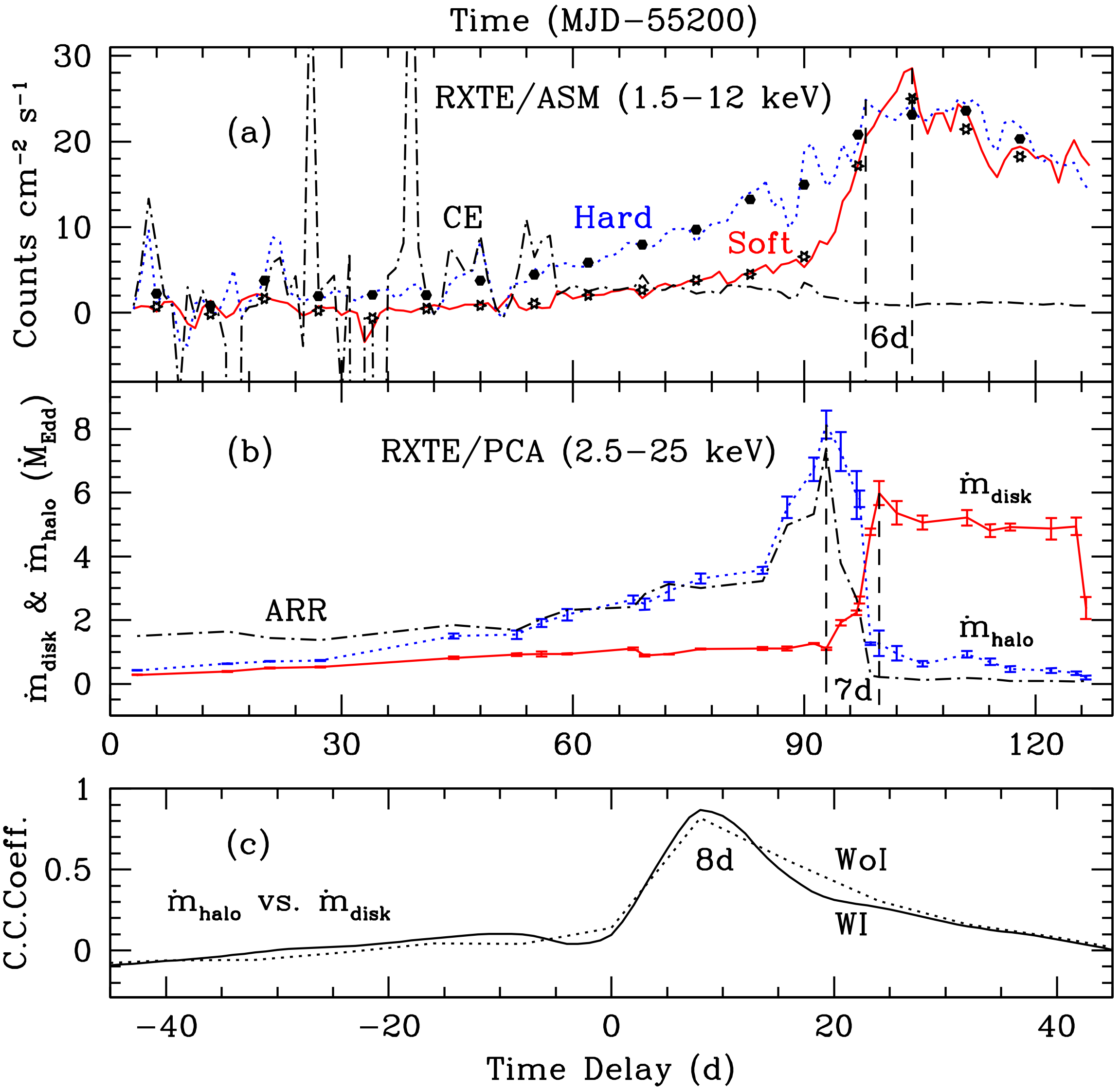

Figure 3.20: OB5 of GX 339-4 in the rising phase: Lightcurves of hard ($3-12$ *keV*), soft ($1.5-3$ *keV*) photon fluxes, and CE (using the same scale but ignoring the flux unit) from RXTE/ASM daily mean data are plotted in (a). Higher values of CE are ignored for clarity. Weakly average data are also plotted with dots for hard & stars for soft. Corresponding mass accretion rates, $\dot{m}_{disk}$ & $\dot{m}_{halo}$ computed with RXTE/PCA ($2.5-25$ *keV*) data by Debnath, Mondal and Chakrabarti (2015), are plotted along with ARR=$\frac{\dot{m}_{halo}}{\dot{m}_{disk}}$ (ignoring the unit for two rates but using the common scale) in (b). CC($\dot{m}_{halo}$, $\dot{m}_{disk}$) profile is shown in (c). Time lags of about a week, which are very less compared to $\tau_r \sim 3$ weeks (vide 10^{th} row of Table 3.2), are marked in all boxes (Ghosh, Banerjee & Chakrabarti 2019).

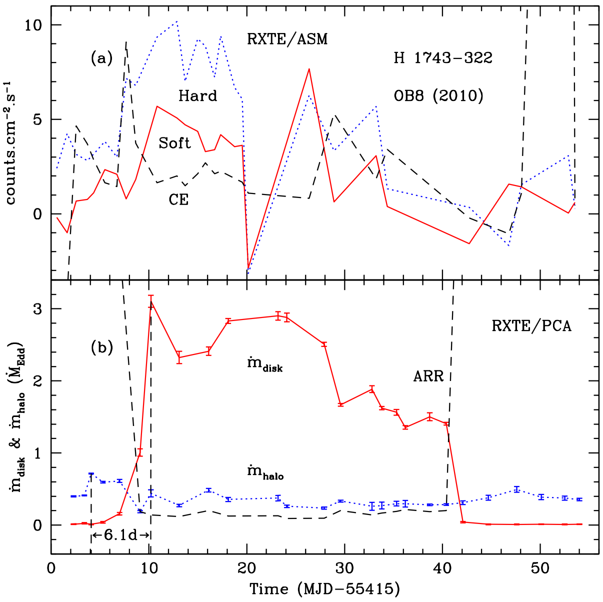

Figure 3.21: OB8 in H 1743-322: (a) soft and hard photon fluxes along with CE (without units) from daily RXTE/ASM data are plotted (see Figs. 3.13h, 3.14h & 3.16h). The hard flux is seen to maintain its peak value for about a week ($\sim \tau_{lc}$) at the beginning. (b) Two mass rates, $\dot{m}_{disk}$ and $\dot{m}_{halo}$, obtained using RXTE/PCA ($2.5-25\ keV$) data by Molla et al.(2017), are drawn. Both peak twice; the first peak is marked with a lag $\tau_{\dot{m}} \sim 6d$ (Ghosh, Banerjee & Chakrabarti 2019).

In order to show a similar situation in H 1743-322, let us step out from here for a while and refer to its OB8 from §3.2. OB8 occurred in 2010 and is found by us to be an anomalous outburst for which $\tau_r = 1(\pm 3.2)d$. Its lightcurves and CE (with the same scale of the fluxes but ignoring their units) are drawn in Fig. 3.21a. From both Fig. 3.21a and Fig. 3.13h, it can be checked that the hard flux peaks in the *harder state* at the commencement, having risen to $< 5\ cnts.cm^{-2}.s^{-1}$ or $< 30\ keV.cm^{-2}.s^{-1}$, and then fluctuates above $3\ cnts.cm^{-2}.s^{-1}$ or $20\ keV.cm^{-2}.s^{-1}$ for less than a week until the soft energy flux peaks. Both peak for a second time later (see Θ-behaviour in Figs. 3.14h & 3.16h). From an eye-estimation, we can infer, $\tau(\Theta_{hi}) \sim \tau_{lc} < 7d$, and expect as well to detect this lag from the mass accretion rates as $\tau_{\dot{m}} < 7d$. Incidentally, two mass accretion rates, $\dot{m}_{disk}$ and $\dot{m}_{halo}$, for this outburst were extracted by Molla, Chakrabarti, Debnath & Mondal (2017). They fitted the spectra obtained from RXTE/PCA ($2.5-25\ keV$) data with TCAF. These two mass rates are drawn in Fig. 3.21a along with ARR, ignoring its unusual higher values (with maxima at ~ 60) at two extreme points of the outburst. Both $\dot{m}_{disk}$ and $\dot{m}_{halo}$ peak twice as expected because of its two mini outbursts (two-fold loop in Fig. 3.16h or two strong dips in Θ-well in Fig. 3.14h). However, the first peaking is marked with a lag $\tau_{\dot{m}} \sim 6.1d \sim \tau(\Theta_{hi})$ (see Figs. 3.13h & 3.16h). CC($\dot{m}_{halo}$, $\dot{m}_{disk}$) would also give rise to peaks indicating similar lags, however, with a little vagueness due to the ill-defined peaks in both photon fluxes and accretion rates. We comprehend that the two lags, viz. $\tau_r = 1(\pm 3.2)d$ and $\tau_{\dot{m}} \sim 6d \sim \tau(\Theta_{hi})$, are actually the same as inherent from the Θ-curve in Fig. 3.14h, the difference arises from the poor CC giving rise to high errorbars.

If we compare Fig. 3.20b for the normal OB5 of GX 339-4 with Fig. 3.21b showing the anomalous OB8 of H 1743-322, we can clearly see anomalies in the latter in terms of the evolving accretion rates $\dot{m}_{disk}$ and $\dot{m}_{halo}$. ARR is unusually high at the begining and the end of both outbursts. We also observed a steady rise in CE at two extreme points of OB8 and also in all other anomalous outbursts of H 1743-322. This is why we did not continue dealing with CE for any outburst of H 1743-322 and depended on finite Θ only. On the other hand, in GX 339-4, OB5 is normal in terms of the mass rates also. At the commencement of a normal outburst, like that in OB5 here, both ARR and CE should be highest (but finite) due to the highest halo rate and both drop quickly due to a fast rise in the disk rate. Both will rise again at the culmination of the outburst because of the dissipation of disk matter in the mean time. Thus, our general classification of normal and anomalous outbursts is justified also from the behaviour of growth and decay of mass accretion rates in them.

3.4.4 Identifying and Unifying all Outbursts by DPI (Θ): Universality

It should be noted again that we can segregate soft and hard photon fluxes by assuming them respectively as black body and power-law radiation components. These, in turn, physically relate to two mass rates, $\dot{m}_{disk}$ and $\dot{m}_{halo}$, which represent two hydrodynamical flow components traveling in two different timescales in accretion process as established by TCAF. With TCAF in hand, we have studied all the outbursts throughout this Chapter and obtained various new and fundamental aspects of them. TCAF is implicitly considered in drawing the histograms of Fig. 3.18 also because soft and hard photons are taken into account separately instead of overall photon flux. As a result, we can see that OB1 and OB5 in H 1743-322 are most likely to be anomalous because the dotted curve with the triangular points representing soft-to-hard ratio is more or less horizontal in both GX 339-4 and H 1743-322. This indicates a constancy except for OB1 and OB5 of the latter. An exceptional difference of height between the bars for soft and hard intensity of OB1 in H 1743-322 is prominent enough to suspect something special hidden in it; we have already seen that OB1 indeed has complex anomalies. Several other quick numerical estimates and qualitative difference in features of altogether ten outbursts in GX 339-4 (OB1-OB5) and H 1743-322 (OB1-OB5) are already discussed in §3.3.1.

Our dynamical photon index, DPI (Θ), connects TCAF with RXTE/ASM data. As, by definition, Θ always operates between a very short numerical range of ±1.57 (or $\pm\pi/2$) only, it can accommodate all outbursts in this range and scan any outburst both temporally and spectrally. We have seen that Θ characteristically assumes both ARR and CE (compare Fig. 3.20a-b with Fig. 3.5(V)) in a more delicate manner and maps all intricate details of different states of the overall spectral transition of any outburst, either normal or anomalous. Figure 3.22 is illustrated at once to see how the five outbursts (OB1 to OB5) in each of GX 339-4

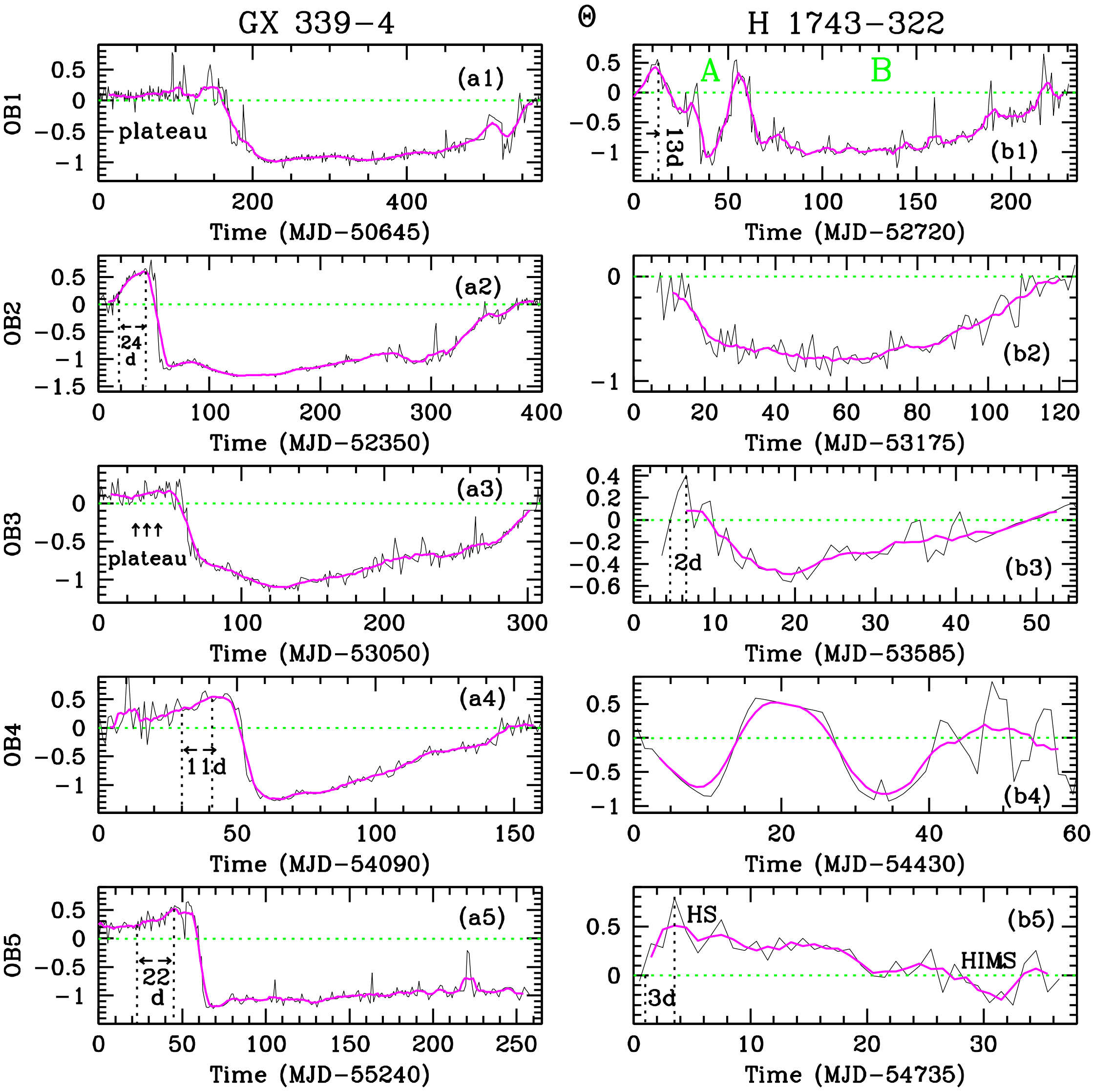

Figure 3.22: Θ-behaviour in OB1–OB5 in both GX 339-4 & H 1743-322: Θ unifies all the outbursts on its unique scale ($-1.57 < \Theta < +1.57$) and scans all spectral and temporal nuances of each outburst. $\Theta_{HS} \to 0$ (horizontal green/dotted lines) defines a plateau in the HS. Average envelopes (smoother curves in magenta) are drawn with running-mean data. Θ drops down from here following the commencement of outbursts and rises again at their end as in (a1) & (a3). But, Θ also shows bumps over the plateau due to an extra spectral hardening ($\Theta_{HS} \to \Theta_{hi} > 0$) in (a2), (a4), (a5) & (b1). Each bump is just a reflection of the time lag, τ_r. Numbers in boxes are approximate $\tau_r(d)$. In (b5), Θ decreases slowly from HS to HIMS, and marginally attains a HS at the end of this anomalous outburst. Multiple wells indicate more than one SS or interim HS/HIMS/SIMS in (b1), and two mini outbursts in (b4) (Ghosh 2018).

and H 1743-322 as represented in Fig. 3.18 can be unified in the (Θ, t)–*space* or distinguished from one another (Ghosh 2018). Along with the actual daily data of Θ, average envelopes (smoother/magenta curves) are drawn using its running-mean data in order to compare them side by side. $\Theta = \Theta_{HS} \rightarrow 0$ (green/dotted horizontal lines) defines the *plateau* in the HS as discussed earlier. Bumps above the plateau in Figs. 3.22(a2, a4, a5 & b1) ensure long time lags (τ_r) and these four OBs are OB-II type forming large disks. A horizontal plateau without a bump (e.g. Figs. 3.22(a1 & a3)) and the lack of a plateau (e.g. Figs. 3.22(b2 & b4)) confirms negligible time lags and both represent OB-I type outbursts carrying small disks. Numbers in boxes are approximate $\tau_r(d)$-values estimated here from the mean curves. The expected Θ-wells seen in Figs. 3.22(a1-a5) tell us that all five OBs of GX 339-4 are normal while the disrupted wells in Figs. 3.22(b1, b4 & b5) establish the presence of spectral anomalies in OB1, OB4 & OB5 of H 1743-322. Moreover, the double wells represent two mini outbursts in OB4 while a twin outburst in OB1 in a broad sense (as OB1-A in Fig. 3.22(b1) itself is two-fold).

Therefore, Θ summarizes spectro-temporal evolution of any outburst in its (Θ, t)-*space*. We can jump to its counterpart, (Θ, E_I)-*space*, which is just the hysteresis loop drawn with total mean energy flux or intensity ($E_I\ keV.cm^{-2}.s^{-1}$) of the outburst for justifying the outcomes from the former. We have already seen this to be true in the hysteresis diagrams of Fig. 3.11 and Fig. 3.16. Therefore, Θ indeed rescales all outbursts showing a universality in its unique scaling character.

Let us now see in the next section how this single dynamic parameter extracts realistic results in other XRBs, which are not transient sources.

3.5 Accretion Flows with Weak Keplerian Components

So far, we have seen that due to a lack of viscosity in achieving its critical limit (α_c) accreting matter can stop at different accumulation radii, X_as, before the multiple outbursts in the same transient source. Also, X_a varies in different transient LMXRBs, which show sporadic outbursts amidst their predominant quiescent phases. Our primary measurable quantity is the relative arrival time lag (or delay), τ_r, of the slow Keplerian flow component behind the fast sub-Keplerian flow component in reaching near the CENBOL at X_s (or r_{in}) from X_a. Therefore, τ_r varies with X_a in proportion. Furthermore, 18 outbursts of 6 transient LMXRBs have revealed that τ_r can be as short as $0d$ and may not be longer than 3 or 4 weeks. Therefore, for transient LMXRBs, we can set two extreme limits to X_a:

$$X_a = X_a^{min}\ for\ \tau_r = \tau_r^{min} \rightarrow 0d \quad (r_{out} \gg X_a^{min} > X_s) \tag{3.3}$$

and

$$X_a = X_a^{max} \; for \; \tau_r = \tau_r^{max} \leq 30d \quad (r_{out} > X_a^{max} \gg X_s). \tag{3.4}$$

Therefore, intuitively, we can write from Eqs. 3.3 & 3.4

$$X_a^{max} \sim \mathscr{O}[10] \; X_a^{min}. \tag{3.5}$$

Eq. 3.3 is attributed to a weak Keplerian flow forming a small accretion disk (as in OB-I type outbursts) while Eq. 3.4 implicates large Keplerian disks, which are required for the outbursts of long duration and high luminosity (i.e. OB-II type outbursts). The upper limit of Eq. 3.4 can be different in other types of LMXRBs. For example, in 1E 1740.7-2942, which is a persistent LMXRB, a time lag of about $25d \sim \tau_r^{max}$ is observed while another persistent LMXRB, GRS 1758-258, shows a lag of $\sim 60d \gg \tau_r^{max}$ (Smith, Heindl & Swank 2002a). This means that the upper critical distance X_a^{max} in transient LMXRBs like GX 339-4 could be the lower limit for X_a in persistent LMXRBs. On the other hand, negligibly small lags ($\sim 0d$) are observed in two persistent HMXRBs, viz. Cyg X-1 & Cyg X-3 (Smith, Heindl & Swank 2002a). So, the Cygnus sources have a bearing on weak Keplerian flows. Eq. 3.5 hints that a 'large' Keplerian disk (as in OB-II type outbursts and persistent LMXRBs) can be bigger than a 'small' Keplerian disk (as in OB-I type outbursts and persistent HMXRBs) by a factor of $\mathscr{O}[10]$.

In this section, we discuss the results of our observational analysis on Cyg X-1 with the dynamic photon index or DPI (Θ) as the main probe (Ghosh & Chakrabarti 2018). Besides, a class-variable source, GRS 1915+105, will be brought into the picture due to its similarities with Cyg X-1 (Ghosh & Chakrabarti 2018). At the end of this section, we shall see how the other Cygnus source, namely, Cyg X-3, behaves quite differently as compared to Cyg X-1, GRS 1915+105 and all other transient XRBs taken into account so far (Ghosh 2018).

3.5.1 Long-term RXTE/ASM Observation of Cyg X-1

Figure 3.23 shows long-term (MJD 50500 − 55500, or about 13 years) behaviour of Cyg X-1 through six quantities, viz. (a) hard flux, (b) soft photon flux, (c) HR1, (d) HR2, (e) CE and (f) DPI (Θ). Photon fluxes are expressed in $counts.cm^{-2}.s^{-1}$ as usual. Weekly running mean data are used for comparison and neatness. Considerable variabilities in all the time series are evident. Θ is seen to be mostly positive indicating omnipresent hard states. Θ attains its highest values during HS in various regions where both soft and hard fluxes are the lowest. In the predominant HS, the soft flux is about half of the hard flux. This implies harder spectra, in general. Variation of both HRs and CE are exactly similar to DPI at all instants of time.

Prima facie, it seems that there is no relative time lag among the soft photon flux, the hard

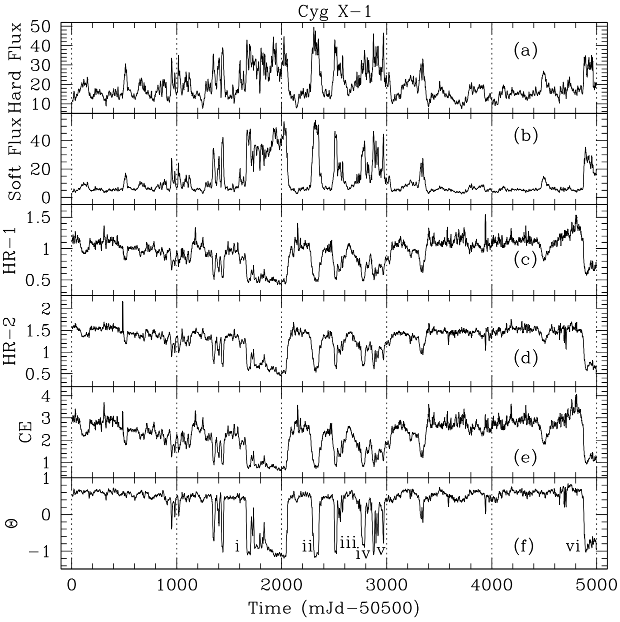

Figure 3.23: Weekly running average photon fluxes ($counts.cm^{-2}.s^{-1}$), HR1, HR2, CE and Θ are plotted respectively in (a) to (f) to show similar variation. A long HS ($\Theta_{HS} \geq 0$) is maintained for first $\sim 1300d$. Thereafter, softening occurs several times till $\sim 3000d$. A longer HS prevails further for $\sim 2000d$ preceding a softening at the end. As $\Theta \to -1$ indicates a softening toward SS, six such phases are marked as 'i' to 'vi' in (f) (Ghosh & Chakrabarti 2018).

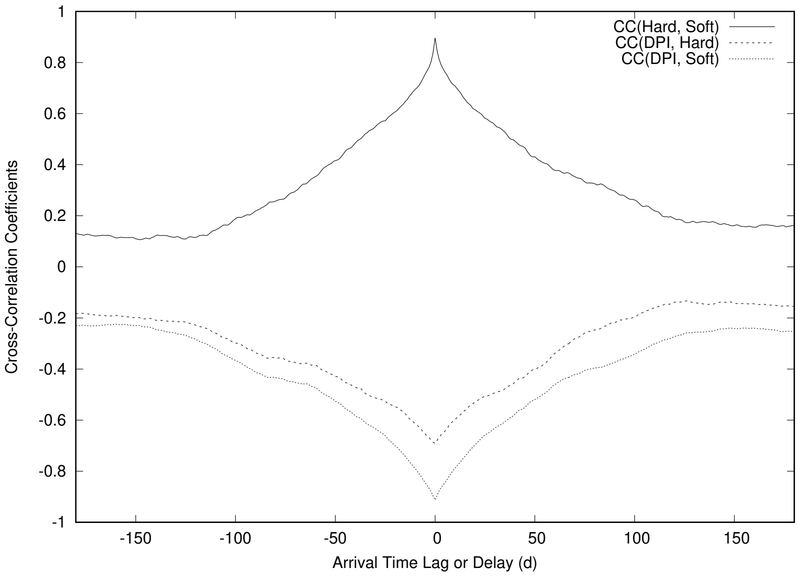

Figure 3.24: CC-profiles with long-term untruncated data of Cyg X-1 are shown. $\tau_r = 0d(\pm 2.4h)$ is seen in both CC(Hard, Soft) and CCs of two photon fluxes with DPI (Θ). Behaviour of Θ with both fluxes is exactly similar to that in OB-I type outbursts observed earlier in LMXRBs.

photon flux and Θ. Irrespective of the phases of spectral transition, a remarkable synchronicity is maintained throughout. To find it accurately, CC-profiles have given identical outputs, when computed with both $0.1d$-bin and $1d$-bin interpolated data without any truncation. The former set of CC-curves, which are reproduced from the same data used in Ghosh & Chakrabarti (2018), are drawn in Fig. 3.24. All CCs, namely, CC(Hard, Soft), CC(DPI, Hard) and CC(DPI, Soft), give rise to $0d(\pm 2.4h)$ lag between one another. This implies that the Keplerian disk is small in size (Ghosh & Chakrabarti 2018). All three CC-curves are exactly similar to those obtained for OB-I type outbursts observed earlier in the transient LMXRBs. Using the three energy bands of long-term ($\sim$ 5 years) RXTE/ASM data separately, Reig, Papadakis & Kylafis (2002) obtained flux-flux CC-profiles, which are similar to the CC(Hard, Soft) curve shown here.

3.5.2 Irregular Soft States in Cyg X-1

Being an HMXRB, the black hole in Cyg X-1 accretes matter from the winds of its companion. Therefore, its apparently everlasting HS is controlled mostly by the sub-Keplerian flow component. Even though Cyg X-1 is known to be a persistent source, it sporadically transits to SS for short time intervals, as indicated in Fig. 3.23f. Both soft and hard fluxes become similar in photon counts during SS. Being a wind-fed system, Cyg X-1 could exhibit *mini outburst*s or *flare*s. Now, unlike HRs and CE, DPI is able to decide the degree of softness quantitatively. In SS, $\Theta \sim -1$ while $\Theta_{HS} \geq 0$ in HS. We can see from Fig. 3.23f that a prolonged HS is more or less maintained for about first 1300d since MJD 50500, thereafter extreme softening occurs several times up to 3000d almost regularly. Thereafter a longer HS prevails for about 2000d preceding a further softening at the end of our observation. There are altogether six SSs, marked as i, ii, iii, iv, v & vi, in which $\Theta = -1$ is achieved. These regions of flaring phases in Fig. 3.23f seem like outbursts of short duration (comparing with the Θ-behaviour of Fig. 3.6).

However, each SS of i to vi marked in Fig. 3.23f is not a flare of our interest, like the complex first one (i) with rapid softening and hardening in HIMS/SIMS. Due to our uniform choice of data (for all three sources under the concern of this section), there is a lack of the declining phase in ‘vi’ and so, it cannot be considered. The easiest way of quickly finding outburst-like flares is to draw hysteresis loops with DPI as the abscissa for the rest four SSs: ii, iii, iv & v. Figure 3.25 shows these loops, i.e. the total (soft + hard) mean photon energy flux vs. DPI plots. The narrow loops of (ii) and (iii) are very much similar to the loops for the OB-I type outbursts (see Figs. 3.10g-j) and are identified as two flares. Let us rename them respectively as Flare I & Flare II for a further study. The loops of (iv) and (v) are narrow but disrupted, even though they are more or less comparable to the former two.

3.5.3 Sporadic Flares in Cyg X-1

For a further confirmation of the long-term no-lag property of Cyg X-1 depicted by the CC-curves of Fig. 3.24, the four short-term soft states (ii to v) of Fig. 3.25 including the selected Flare I (i.e. ii) and Flare II (i.e. iii) are also considered for correlation. However, as expected, CC-profiles with the two photon fluxes and DPI in them also have given $\tau_r = 0d$. Figure 3.26 illustrates such CC-curves obtained with the short-term data of Flare I (i.e. the SS ‘ii’ of Fig. 3.25). Both CC(DPI, Hard) and CC(DPI, Soft) peaks give a time lag of $\tau_r = 0(\pm 0.1)d$. CC(Hard, Soft) gives 0d lag as usual. All three CC-curves are not only similar to the CC-profiles with the entire data of Cyg X-1 (Fig. 3.24) but also to those for OB-I type outbursts (see Figs. 3.7(a2 & c2) and 3.8(a2 & b2)). In all these cases, DPI is anti-correlated with both

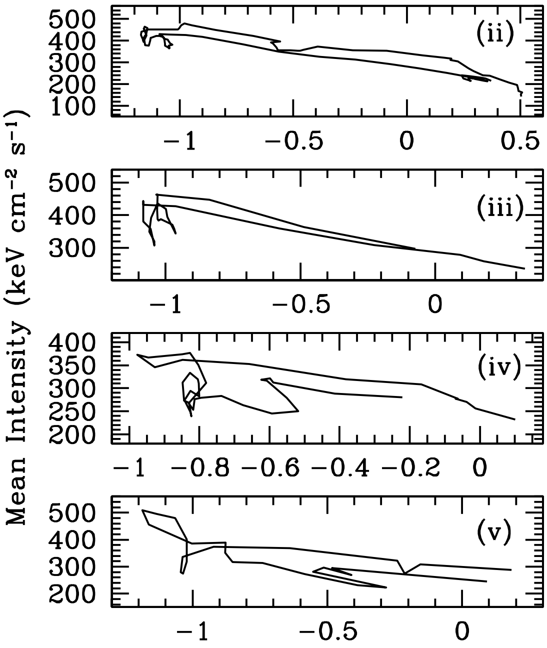

Figure 3.25: To find outburst-like flares quickly, hysteresis loops are drawn with DPI as the abscissa for the four SSs, namely, ii, iii, iv & v as marked in Fig. 3.23f. For a lack of the declining phase due to the choice of data, 'vi' is omitted; 'i' is is also ignored for its complex feature. As the narrow loops of (ii) and (iii) are very much similar to the loops for the outbursts of OB-I type (Figs. 3.10g-j and are identified as two flares: Flare I & Flare II.

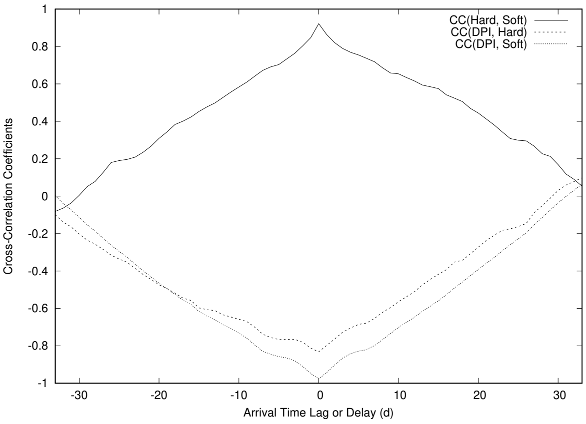

Figure 3.26: CC-profiles in Flare I (i.e. Fig. 3.25(ii)) are shown. CC(DPI, Hard) and CC(DPI, Soft) peaks give $\tau_r = 0(\pm 0.1)d$. CC(Hard, Soft) gives $0d$ lag as usual. All CC-curves mimic the CC-profiles of Fig. 3.24 as well as those for an OB-I type outburst (see Figs. 3.7(a2 & c2) and 3.8(a2 & b2)).

photon fluxes.

Therefore, infrequent flares in Cyg X-1 are very much important in understanding its Keplerian accretion flow, which must be a weak flow forming a very small disk like that observed in an OB-I type outburst. Next, we take into account both Flare I and Flare II for studying them from a different approach.

3.5.4 Luminous Flare(s) of Cyg X-1 with RXTE/PCA ($2.5 - 25\ keV$) Data

It can be readily seen from Fig. 3.23 that throughout the duration of our long-term observation of more than 13 years, Flare I is the most conspicuous and deserves a further analysis in a greater detail for understanding the underlying accretion flow dynamics in Cyg X-1. Flare II is relatively less luminous. Both flares are zoomed with the soft and hard photon counts are plotted with RXTE/ASM daily average data in Fig. 3.27a. In Fig. 3.27b, CE, HR1 & HR2, corresponding to the lightcurves of Fig. 3.27a are plotted. GBC19 have fitted the $2.5 - 25\ keV$ spectra of Cyg X-1 obtained from RXTE/PCA data for $530d$ (MJD $52621 - 53151$) comprising both flares with TCAF solution. Two mass accretion rates, $\dot{m}_{disk}$ and $\dot{m}_{halo}$, thus extracted by them, are plotted in Fig. 3.27c along with their ratio, ARR.

For about a month (< MJD 52650) prior to Flare I the source was in the HS. Figure 3.27b clearly shows higher values of HR1 & HR2 and CE during this period while Fig. 3.27a reveals that the hard flux is greater than the soft flux over this duration. $\dot{m}_{halo}$ is consistently higher than $\dot{m}_{disk}$ during this period, i.e., the average $\dot{m}_{halo}$ is $< 2\ \dot{M}_{Edd}$ and the average $\dot{m}_{disk}$ is $< 1\ \dot{M}_{Edd}$ are maintained in this period, as seen from Fig. 3.27c. Thus ARR=$\dot{m}_{halo}/\dot{m}_{disk}$ is also high (~ 2.5) during this period. Then, all of a sudden, both mass rates rise simultaneously. The time lag between them was found to be $\tau_{\dot{m}} = 0d^{+4.42}_{-1.43}h$. For the outbursts in LMXRBs, we have seen earlier (Fig. 3.20b & Fig. 3.21) that the halo rate always rises earlier by about a week than the disk rate. However, in Flare I of Cyg X-1, the peaking instants of two rates are almost coincident. This further implies that the Keplerian disk is indeed small in size. At $\sim 360d$ (from the origin at MJD 52610) Flare II occurs when the disk rate exceeds the halo rate again, ARR drops in the rising phase. This behavior continues till $\sim 450d$. Fig. 3.27b shows diminished CE, HR1 and HR2 during this short period characterized by a SS. The spectral state transits from this SS to an intermediate state or a HS around $460d$ and this continues till the end of our observation. The average halo rate during this period is $\sim 6.5\dot{M}_{Edd}$, the average disk rate $\sim 2.5\dot{M}_{Edd}$. Meanwhile, HR1, HR2, CE and ARR have gone up, as evident from Figs. 3.27b-c).

In view of Fig. 3.27c, it seems that Flare I begins in the HS while Flare II occurs immediately after Flare I without passing through an overlapping HS in between. Rather, Flare II seems to begin in the SIMS/HIMS, during the the declining phase of Flare I. It is possible that the Keplerian disk of Flare I was not dissipated totally. So, Flare II is different from Flare I, even though both declines with similar values of accretion rates ($\sim$ at $300d$ & $500d$ from MJD 52610 in Fig. 3.27c).

Two accretion rates are cross-correlated, keeping the time window confined between the commencement and the peak of Flare I, using the data with interpolation (WI) or without interpolation (WoI), as shown in Fig. 3.28. The same $0d$ time lag is obtained. The symmetry of the CC-curves about the peak is similar to that of CC(Hard, Soft) in Fig. 3.24. This is in contrast with the asymmetric peak obtained for the outburst OB5 of GX 339-4 shown earlier in Fig. 3.20c. As discussed earlier, such a symmetry signifies a negligible relaxation time for the system following the quick dissipation of a Keplerian flow.

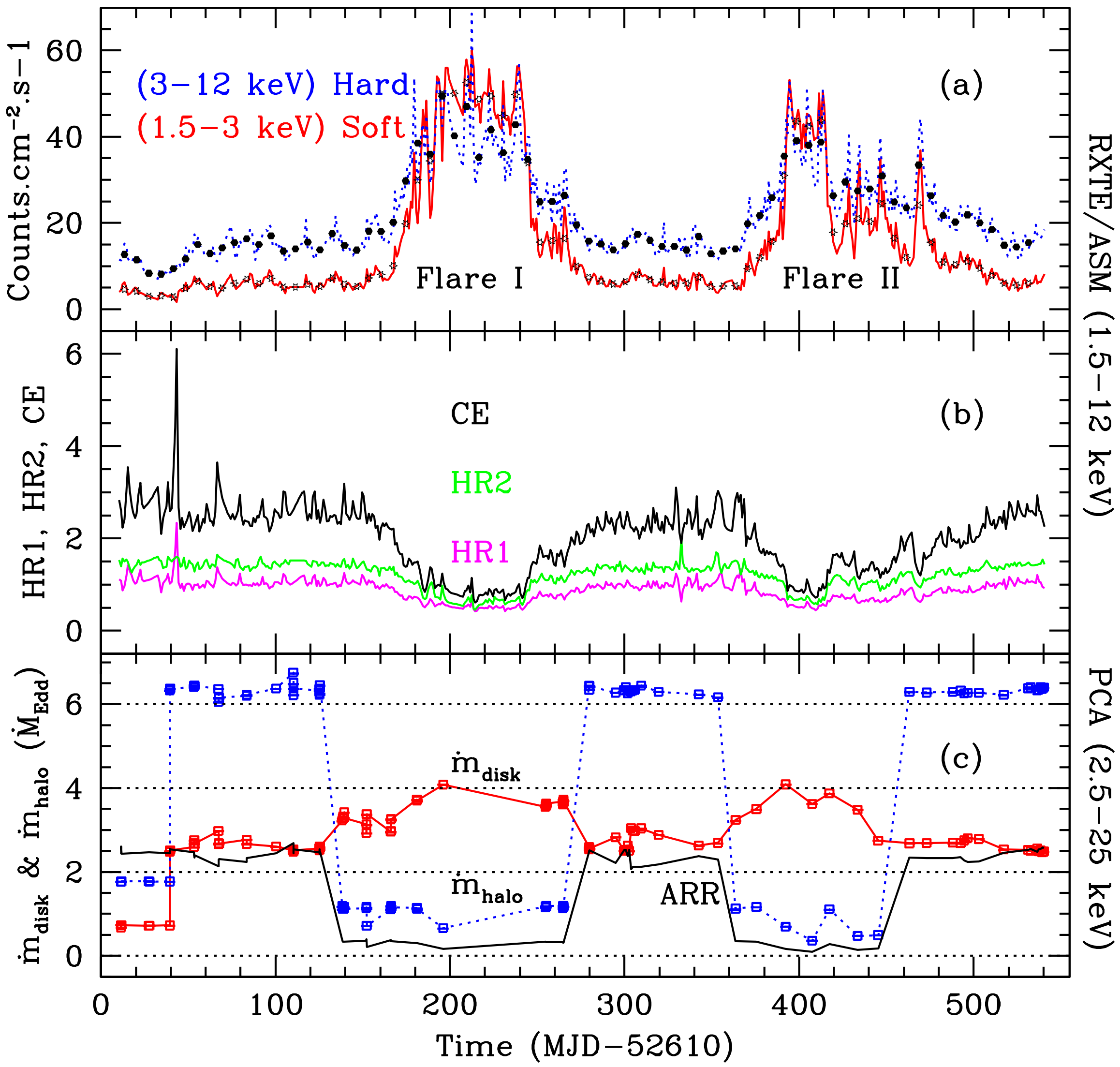

Figure 3.27: Flare I & Flare II of Cyg X-1: (a) Long-term lightcurves (dotted/blue for hard photon flux and continuous/red for soft photon flux) with RXTE/ASM daily average data are plotted. Also, weekly average data are plotted with points (dots for hard & stars for soft) for a quick look at their synchronous responses; both hard and soft fluxes are clearly seen to evolve simultaneously. CE, HR1 & HR2 are plotted in (b). All quantities seem to vary similarly at all instants. In (c), two accretion rates $\dot{m}_{disk}$ and $\dot{m}_{halo}$, as obtained from TCAF-fitted spectra of RXTE/PCA $(2.5-25\ keV)$ data are plotted. The accretion rate ratio (ARR) is roughly constant during the flares. Both mass rates quite possibly peak at the same instant ($\sim$ MJD 52650) before Flare I indicating no apparent time delay, $\tau_{\dot{m}} = 0d^{+4.42}_{-1.43}h$, in agreement with our previous $\tau_r = 0d(\pm 2.4h)$. Relatively irregular, Flare II occurred immediately after Flare I without any detectable achievement of HS in between (Ghosh, Banerjee & Chakrabarti 2019).

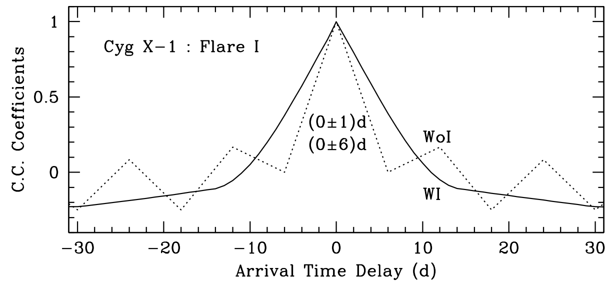

Figure 3.28: CC($\dot{m_{halo}}$, $\dot{m_{disk}}$) profiles are obtained by using the data with interpolation (WI) and without interpolation (WoI) between the commencement and the peak of Flare I. Both peaks give a time lag of $\tau = 0d$.

3.5.5 Accretion Disk Size in Cyg X-1

Our different ways of analysis of Cyg X-1, on the short-term basis or in the long run, reveal that the sub-Keplerian halo flow is predominant most of the time. However, during sporadic soft states or flares weak Keplerian flows are generated. There is no detectable time lag between the disk and the halo. As the changes in the Keplerian flow rate and the recession of the inner edge of the disk are decided by the viscosity at X_a, it is possible that a fresh but ephemeral ring-like disk forms from the halo component due to a sudden rise in viscosity which gives rise to sporadic mini outbursts or flares. There could be a major influence from the periodic modulation due to its eccentric binary orbit on the variation of accretion rates. This could lead to an aperiodic variability observed in the brightness of Cyg X-1.

Nevertheless, the subsequent rise and fall in mass accretion rates are akin to SIMS to SS or vice versa in outbursts. Thus the rates vary similarly. However, there is no detectable delay in the peaking of the two photon fluxes (compare Fig. 3.27a with Fig. 3.20a. Therefore, the Keplerian disk size in Cyg X-1 must be very small and the viscous timescale through the Keplerian flow does not significantly enhance the travel time of accreting matter from the outer edge to the inner edge of the disk. It could be possible that no accumulation radius X_a is needed at all in forming a very small Keplerian disk even though $\tau_r = 0d$ indicates a nearby threshold for X_a like that for an OB-I type outburst of a given transient source carrying a small disk (see Eq. 3.3). However, the size of the disks is different in different OB-II type outbursts, but for persistent Cyg X-1 such an ambiguity is absent. It seems that whenever its small disk is formed, it is dissipated away very fast and the HS ($\Theta_{HS} \sim 0.5$) is returned within a short time due to a lack of hysteresis (see the CC(Hard, Soft) curve in Fig. 3.24 and Fig. 3.28).

3.5.6 Long-term RXTE/ASM Observation of GRS 1915+105

Since its discovery in 1992, GRS 1915+105 has been monitored more than thousands of times by RXTE and found to have lightcurves of unpredictable nature with variability in timescales ranging from seconds to days. It is regarded as a transient source with a significant variability in X-rays (Castro-Tirado et al. 1994; Greiner, Morgan & Remillard 1996; Morgan, Remillard

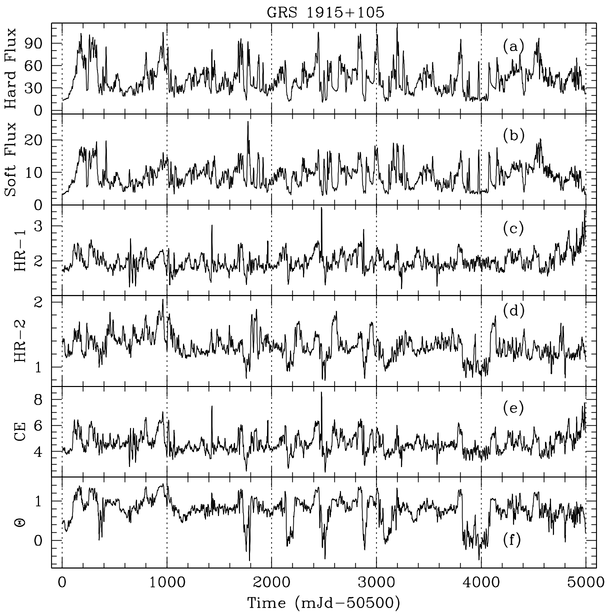

Figure 3.29: Using weekly running-mean data, two photon fluxes ($counts.cm^{-2}.s^{-1}$) are plotted in (a) and (b) while (c) to (f) show similar variation in HR1, HR2, CE and Θ. Θ-behaviour in (f) indicates that the source mostly resides in HS like Cyg X-1 but there are atleast six HIMSs present instead of any SS as $\Theta > -0.4$. The average hard flux is several (~ 5) times higher than the soft flux unlike Cyg X-1 (Ghosh & Chakrabarti 2018).

& Greiner 1997; Harlaftis & Greiner 2004). Several observers have reported that this enigmatic source exhibits many types of variability classes which are named as: α, β, γ, δ, ϕ, $\chi_1, \chi_2, \chi_3, \chi_4$, μ, ν, λ, κ, ρ, θ, etc. (Belloni et al. 2000; Rao et al. 2000; Chakrabarti et al. 2000). These variability class transitions are results of the geometry of the Compton cloud, apart from the usual variation in accretion rates of Keplerian and sub-Keplerian disks (Pal, Chakrabarti & Nandi 2013). However, these classes of the pattern formation in the lightcurves do not appear at random, but maintains an order, which is directly dependent on the Comptonizing efficiency (Pal & Chakrabarti 2015). A very fast spectral transition between SS and SIMS in GRS 1915+105 is believed to be due to a critically viscous accretion flow (Naik et al. 2002).

Despite the fact that GRS 1915+105 is a LMXRB while Cyg X-1 is a HMXRB, there are certain similarities between them. For example, the BH mass of both is comparable and is about $14-15\ M_{\odot}$ (Harlaftis & Greiner 2004; Orostz et al. 2011). On the other hand, similar flux-flux relationship and a few common classes of aperiodic variability are observed in both from the analysis of long-term ($\sim 5\ yr$) RXTE/ASM data (e.g. Reig, Papadakis & Kylafis 2002). Moreover, in both the sources, strong sub-Keplerian winds control the overall accretion process. In order to investigate GRS 1915+105 from our generalized approach on the basis of the single parameter of reference (DPI) we present here the results of a very long-term ($\sim 13\ yr$) analysis with RXTE/ASM data.

Figure 3.29 shows the behaviour of GRS 1915+105 for a long time through six quantities, viz. (a) hard photon flux, (b) soft photon flux, (c) HR1, (d) HR2, (e) CE and (f) DPI or Θ. Weekly running mean data are used to compare the variation in all time series. Θ is not only

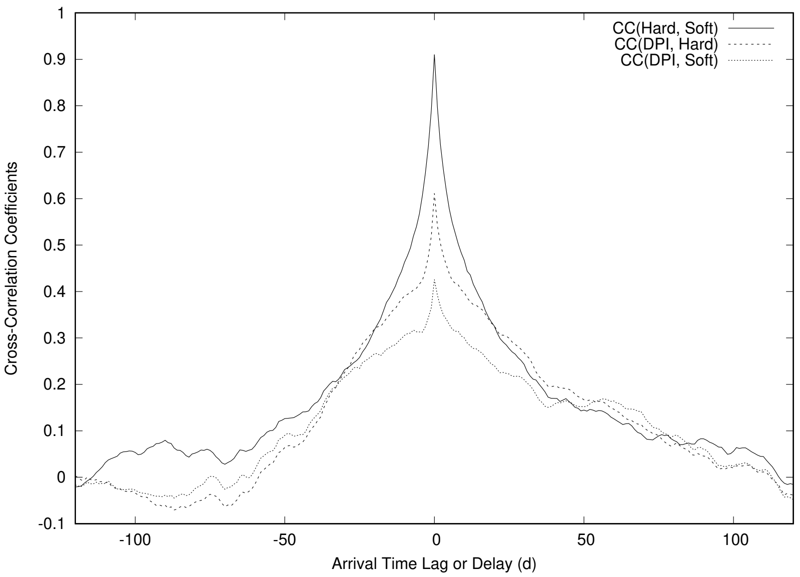

Figure 3.30: CC-profiles using long-term (> 13 years) data of GRS 1915+105. $\tau_r = 0(\pm 0.1)d$ is obtained from CC(DPI, Hard) and CC(DPI, Soft). Unlike the anti-correlation seen in Cyg X-1 (Fig. 3.24), DPI is strongly correlated with both fluxes, and furthermore, CC-curves with DPI are not fully segregated.

positive ($\Theta \to +1$) for most of the time but also is rarely negative ($\Theta > -0.4$). Θ-behaviour in Fig. 3.29f indicates that the source mostly resides in HS like Cyg X-1 throughout but there are atleast six HIMSs present (where $-0.4 < \Theta < 0$) instead of any SS. These, however, are not comparable with the six SSs (where $\Theta \leq -1$) comprising the outburst-like flares of Cyg X-1. In regions of low soft and hard fluxes, both CE and Θ are high. However, unlike Cyg X-1, the hard flux is several ($\sim 5-6$) times higher in count rate than the soft flux and so, CE is much higher. This implies that harder spectra are predominant. But it is not obvious from Figs. 3.29a-b & 3.29f whether there is a definite time lag between the photon fluxes and Θ. As Θ and CE change simultaneously with both photon fluxes, there should be really a negligible lag. In order to find it, CC-profiles are computed using the entire untruncated daily average data as well as dwell-by-dwell ASM data with $0.1d$ time bin and similar outputs result in. The latter set of CC-curves, viz. CC(Hard, Soft), CC(DPI, Hard) & CC(DPI, Soft), which are reproduced from the same data used in Ghosh & Chakrabarti (2018) but with different binning, as shown in Fig. 3.30, indicates that hard and soft fluxes have no relative lag with DPI, $\tau_r = 0(\pm 0.1)d$. This implies that the size of the Keplerian disk cannot be large.

However, as far as the CC-curves are concerned, there is an important difference between Cyg X-1 and GRS 1915+105 evident from Fig. 3.24 and Fig. 3.30. CC-curves with DPI show a strong anti-correlation between each photon flux and DPI in Cyg X-1, whereas, DPI is strongly correlated with both fluxes in GRS 1915+105. Moreover, CC-curves with DPI are not fully segregated in the latter. This means that there is a nonlinear dependence between the so-called soft and hard photon fluxes in GRS 1915+105; the origin of class-variability could be hidden in this feature. Such a situation is absent in Cyg X-1 in general, but may partially arise only during its flaring phases (compare Fig. 3.24 with Fig. 3.26). Therefore, a reason behind the reported observation of a few variable classes in Cyg X-1 seems to be inherent in its tendency of mostly remaining in SSs.

But, in both Cyg X-1 & GRS 1915+105, the sub-Keplerian halo which arose from the companion winds dominates over a weak Keplerian flow and the disk is very small in size. This means that the viscosity of the disk matter somehow remains close to the threshold (α_c), even if the accumulation radius X_a is uncertain or not required. As a consequence, an ephemeral Kepleian disk is formed and broken in short time scales. But, this formation is likely to happen quite regularly in GRS 1915+105 and sporadically in Cyg X-1.

Nevertheless, all our attempts to detect a time delay in both Cyg X-1 & GRS 1915+105 with long-term data and also with the short-term data chunks in the former have gone in vain. Our results open up a possibility that there is a subtle *missing link* between the transient and variability sources. Cyg X-1 appears to be either persistently transient or transiently class-variable. But it marginally misses something what we recognize as *outburst*s, and smaller *flare*s are observed instead (Ghosh & Chakrabarti 2018; GBC19). On the other hand, GRS 1915+105 could be persistently class-variable, but its fleeting patterns of variability, which are observed only with brief data chunks of $\mathscr{O}[1000s]$, cannot be expected to be seen in the weekly running-mean lightcurves of our observation. However, such a possibility of large-scale pattern replication even in the long-term lightcurves cannot be ruled out if the data are binned in a proper manner.

3.5.7 Long-term RXTE/ASM Observation of Cyg X-3

Like Cyg X-1, Cyg X-3 is also known to be a wind-fed HMXRB and flares are observed more regularly in Cyg X-3. So, we can expect its Keplerian disk to be similar to that of Cyg X-1. However, the presence of well-collimated regular jets in it is an indicative of a stable accretion disk. Cyg X-3 has also been given the variable star designation V1521 Cygnus because of the variations in emission at various wavelengths. Therefore, it is imperative to see whether Cyg X-3 also behaves like Cyg X-1 or not.

Figure 3.31 shows long-term (> 13 yr) observation of Cyg X-3 by RXTE/ASM in terms of its lightcurves (the time interval is the same as in Cyg X-1 and GRS 1915+105) in both low energy (soft) and high energy (hard) levels and the four parameters, HR1, HR2, CE and Θ. All curves are plotted with weekly running-mean data for a quick look of the source behaviour. Hard and soft photon fluxes are plotted in (a) and (b) respectively. Both fluxes seem to evolve simultaneously. This instantaneous response was also observed in Cyg X-1 (Fig. 3.23) and GRS 1915+105 (Fig. 3.29). But, the hard flux in Cyg X-3 is comparable to the soft fluxes in

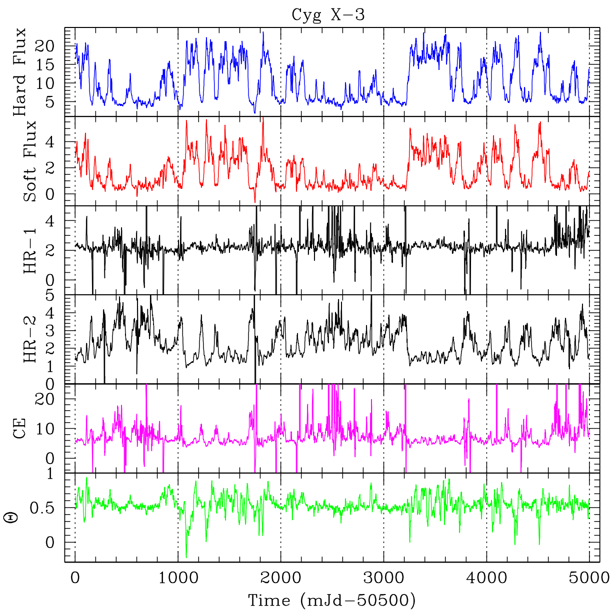

Figure 3.31: Both fluxes ($counts.cm^{-2}.s^{-1}$) seem to evolve simultaneously like those in Cyg X-1 and GRS 1915+105. However, HR1, HR2 and CE vary quite differently. HR1, HR2$<$ 2.5 & CE$<$ 4 in Cyg X-1 while HR1, HR2$<$ 3.5 & CE$<$ 8 in GRS 1915+105. Here, we see that both HR1 & CE become too high to be included (HR1$>$ 6 & CE$>$ 20) sometimes while HR2 (mostly $<$ 5) varies almost similarly as in other two objects. Θ is mostly positive ($\Theta_{HS} \sim 0.5$).

the former two objects while the soft flux is significantly smaller than those noticed in them. Furthermore, Fig. 3.31 shows a notably different behaviour in HR1, HR2 and CE respectively. We observed that HR1, HR2$<$ 2.5 & CE$<$ 4 in Cyg X-1 while HR1, HR2$<$ 3.5 & CE$<$ 8 in GRS 1915+105. However, for Cyg X-3, even though HR2 (mostly $<$ 5) varies almost similarly as in other two objects, both HR1 & CE are too high (HR1$>$ 6 & CE$>$ 20) in several regions. We have excluded those data points from the plots. This means that the soft flux, in spite of its very low counts, plays a crucial role behind this unusually high CE. Thus, the Keplerian flow in Cyg X-3 is likely to be totally different as compared to Cyg X-1 or GRS 1915+105. Unexpected behaviour of Θ with the response of the fluxes in some regions (e.g., before $1000d$ from MJD 50500) indicates that Cyg X-3 can be quite different from the former two objects.

Using the untruncated lightcurves and Θ-curve of Fig. 3.31 but with daily average data and $0.1d$-bin data. Similar CC-profiles have been obtained by us. Fig. 3.32A shows CC(Hard, Soft) curve while CC(DPI, Hard) and CC(DPI, Soft) curves are drawn in Fig. 3.32B separately, where equally weak peaks (between $-25d$ & $-30d$) are comparable. Rebinning with a few longer time intervals revealed that this timescale would be $-27d$. A roughly sinusoidal feature in both apparently hints at a periodic modulation of the fluxes with the DPI. There is also a weaker periodic variation between $+25d$ & $+30d$. On the other hand, CC(DPI, Hard) curve shows an additional peak at $0d$, which is comparable to the corresponding peak seen in Fig. 3.30 for GRS 1915+105. But, the the response of the hard flux to the DPI is much stronger than that of the soft flux in both Cyg X-1 and GRS 1915+105. In Cyg X-3, both respond to the DPI comparably except at $\tau_r = 0d$. Each of these features is of a kind and indicate a weak but complex Keplerian accretion flow in Cyg X-3, even though the symmetry about the peak

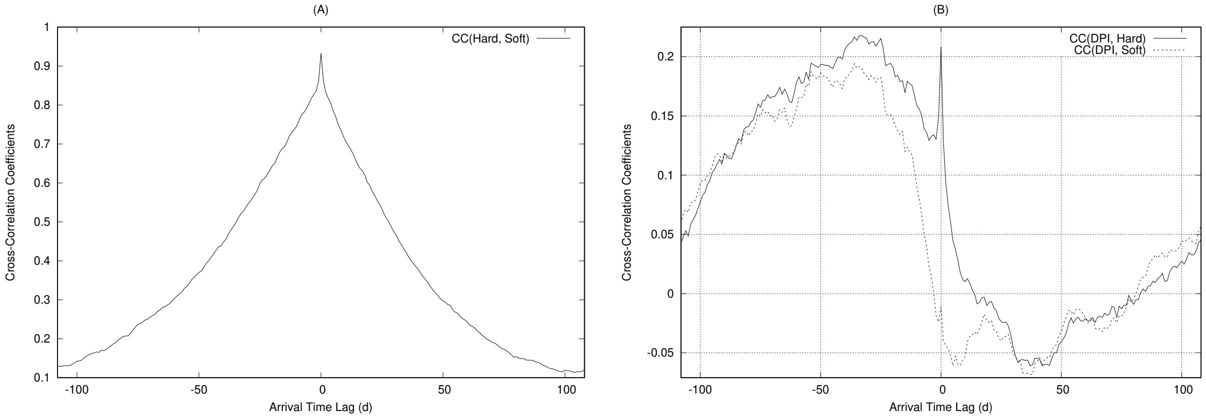

Figure 3.32: CC(Hard, Soft) curve is shown in (A). CC(DPI, Hard) and CC(DPI, Soft) curves are drawn in (B), where equally weak peaks (between $-25d$ & $-30d$) in (B) are comparable. There is also a weak periodic variation between $+25d$ & $+30d$. On the other hand, CC(DPI, Hard) curve shows an additional peak at $0d$, which is comparable to the corresponding peak seen in Fig. 3.30 for GRS 1915+105. All these features indicate a weak but complex Keplerian accretion flow in Cyg X-3. The symmetry about the peak at $0d$ in (A), however, hints at a fine tuning.

at $0d$ in Fig. 3.32A hints at a fine tuning.

For both the Cygnus sources, there may not be any accumulation radius X_a, where matter needs to pile up for making a prospective disk. Otherwise, X_a is not far from both inner and outer edges ($r_{in} \sim X_s$ and r_{out}) so that the Keplerian flow is confined in a narrow inner region. The DPI (Θ) is mostly positive when both objects are in the HS with an average saturation at $\Theta_{HS} \approx \Theta_{av} \sim 0.5$ which is comparable to the highest value of Θ ($\Theta_{hi} \sim 0.5$) attained during the HS→*harder state* transition prior to an OB-II type outburst for which X_a must be far away. This means that such a spectral hardening is not required for the Cygnus sources for resulting in a flare or a similar softer transition. For GRS 1915+105, however, $0.5 \geq \Theta_{HS} \rightarrow 1$ is mostly observed in its HS (Fig. 3.29f).

Unlike Cyg X-1 and GRS 1915+105, the nature of the compact object (whether a BH or a NS) in Cyg X–3 has never been concluded decisively. Moreover, its compact mass, even with a BH, has still remained uncertain. Although Zdziarski et al. (2013) favour a low-mass BH ($2.4^{+2.1}_{-1.1}$ $M_\odot$) on the basis of orbital kinematics using infrared and X-ray emission lines but their estimate keeps the possibility of a NS open. On the other hand, based on X-ray spectral modelling, the mass of the BH could be as high as 30 $M_\odot$ (Hjalmarsdotter et al. 2008). Using infrared spectroscopy, Koljonen & Maccarone (2017) have placed intermediate limits of $\leq (5-10)\ M_{\odot}$ on the possible mass of the compact object (BH/NS). Therefore, it is difficult to compare the photon character in Cyg X-3 with that of Cyg X-1 or GRS 1915+105 as the mass of the compact object would decide the temperature at the inner edge of the disk. Manifestly, there are a few discrepancies in Cyg X-3. First, hard photons behave like the soft photons of Cyg X-1 or GRS 1915+105, whereas soft photons appear to be strangely low in count rate. Second, the CC(DPI, Hard) curve is almost coupled throughout with the CC(DPI, Soft) curve. This could lead to a possibility that there is no thin line for its photons to be identified as 'soft' or 'hard'. Only a low-mass BH could justify these two features. But, the most interesting observation is that the DPI simultaneously shows two peaks at $0d$ and $\sim -27d$, which are significant as both are equally weak. This requires further investigation. Nevertheless, $\tau_r = 0(\pm 0.1)d$ may be concluded in Cyg X-3 indicating a small Keplerian disk, which cannot be like the ephemeral disk formed during the flaring phases in Cyg X-1. All these characteristics hint that Cyg X-3 is different from Cyg X-1.

Chapter 4

Influence of Accretion Disk Size on Orbital Modulations in XRBs

Both temporal and spectral variations of X-ray fluxes from stellar mass BHBs are observed from spectral state transitions in different energy levels. Sometimes these give rise to quasi-periodic oscillations (QPOs). In addition, weaker modulations of photon fluxes could also carry orbital informations such as the periodicity, T. Brocksopp et al. (1999) reported such an orbital modulation in Cyg X-1 at its well-known $T = 5.6\ d$. Wen et al. (1999) used RXTE/ASM data (for 2 yr) of Cyg X-1 in its HS and detected this orbital period from Lomb-Scargle periodograms (LSPs) of both lightcurves and HRs. However, such a feature did not appear in the SS. On the other hand, Boroson and Vrtilek (2010) found similar orbital variability also in the SS of Cyg X-1 by extracting LSPs from long-term RXTE/ASM lightcurves. It was concluded that the orbital variability in the SS could be detected only with the longer span of data. Wen et al. (1999) pointed out that absorption of X-rays by the stellar wind from the companion star could reproduce the observed X-ray orbital modulations in the HS. Wen et al. (2006) analyzed long-term ($\sim 8\ yr$) RXTE/ASM data again and showed periodic modulation in LSPs for a large number of X-ray sources. Their systematic analysis reveals that the detection of such orbital modulations is more likely in HMXRBs than in LMXRBs.

However, this is not the only cause of a periodic modulation observed in long-term X-ray data. Cataclysmic XRBs show superhumps with a periodicity comparable to the orbital period if the mass ratio, $q = \frac{M_\star}{M_\bullet} < 0.3$ (Patterson et al. 2005). Boyd, Smale and Dolan (2001) found X-ray modulation in LMC X-3 at the known orbital period of $1.7d$. Smith et al. (2002b) found orbital modulations of $12.73(\pm 0.05)d$ and $18.45(\pm 0.1)d$ in 1E 1740.7-2942 and GRS 1758-258 respectively; however, their estimate could drift for GRS 1758-258 (Obst et al.

2013). Kudryavtsev et al. (2004) obtained known orbital periodicites of several XRBs (e.g. H 1705-25, GRO J1655-40, 4U 1543-47, etc.) from the *Mir* satellite data as well. They could not identify the cause of such a modulation but ruled out eclipsing effects. All these reports motivated us to find a possible reason behind such an effect. The results are mostly based on the observation in Ghosh & Chakrabarti (2016).

4.1 Quasi-Orbital Period (QOP): Tidal Effect

A similar periodic modulation can also arise if the XRB orbit has small but non-zero eccentricity. This is possible because an exact circular orbit cannot be supposed to be easily achievable. Such a binary orbit is characterized by the *quasi-orbital period* (QOP). The tidal force F_t exerted by the primary on the companion would be inversely proportional to the cube of the distance between the two components. If semi-major axis and eccentricity are a and e respectively, then

$$F_{t,a} \propto \frac{1}{[a(1+e)]^3} \tag{4.1}$$

and

$$F_{t,p} \propto \frac{1}{[a(1-e)]^3} \tag{4.2}$$

would be the net tidal force at apastron (marked by subscript ‘t,a’) and periastron (marked by subscript ‘t,p’) respectively (Bradt 2008). In our context, where we consider the passage of the companion around a BH, we use the terms *aponigrumcavum* and *perinigrumcavum* (ANC and PNC in short) to represent apastron and periastron respectively (*nigrum cavum* being ‘black hole’ in Latin) (Ghosh & Chakrabarti 2016). Supply of matter from the companion could be assumed to be proportional to this tidal effect and that will have a periodic variation in the flow rate, $\dot{m}$. This means that there will be an enhancement at PNC and diminution at ANC in succession during each QOP (∼T). Ratio of any of the component rates (i.e. $\dot{m}_{disk}$ & $\dot{m}_{halo}$) at ANC and PNC would be

$$\frac{\dot{m}_{ANC}}{\dot{m}_{PNC}} = \frac{\mathscr{F}_{ANC}}{\mathscr{F}_{PNC}} = \frac{(1-e)^3}{(1+e)^3}, \tag{4.3}$$

where, $\mathscr{F}$ represents radiation fluxs at respective locations (i.e. ANC & PNC). The first equality holds for a Keplerian disk if e is small enough so that the Roche lobe remains filled at both ANC and PNC. In this case, the modulation of the Keplerian rate will propagate in viscous timescales and enhance soft X-rays which act as seed photons. This will, in turn, increase the Comptonized X-rays or the hard flux. We should therefore expect a modulation of X-ray photon flux at QOP in all the compact XRBs for which $e \neq 0$.

When observed for a long time, $t = nT$, the successive enhancement and diminution respectively at PNC and ANC should give rise to a peak, ideally at the orbital time period T, in the

Table 4.1: Some known orbital parameters in 6 XRBs under consideration (Ghosh & Chakrabarti 2016)

X-Ray Binary	$M_\bullet(M_\odot)$	$M_\star(M_\odot)$	Inclination(i°)	Period(T)
Cyg X-1	14.8 ± 1^a	19.2 ± 1.9^a	27.1 ± 0.8^a	$5.6\ d^b$
Cyg X-3	$2.4^{+2.1c}_{-1.1}$	$10.3^{+3.9c}_{-2.8}$	$34 - 54^c$	$4.8\ h^{c,d}$
H 1705-25	6 ± 2^e	0.3^f	$48 - 51^g$	$12.5\ h^e$
XTE J1650-500	$2.7 - 7.3^{h,i}$	-	50 ± 3^h	$7.63\ h^h$
GRS 1758-258	$\geq 3^j$	0.65^j	-	$\sim 6\ h^j$
1E 1740.7-2942	-	$1 - 9^k$	-	$< 20\ h^k$

[a]Orosz et al. (2011), [b]Brocksopp et al. (1999), [c]Zdziarski et al. (2013), [d]Davidsen & Ostriker (1974), [e]Johannsen et al. (2009), [f]Orosz & Baily (1997), [g]Martin et al. (1995), [h]Orosz et al. (2004), [i]Shaposhnikov & Titarchuk (2009), [j]Kuznetsov et al. (1999), [k]Chen et al. (1994).

Fourier spectrum of a long-term lightcurve. We show that several XRBs having a BH exhibit such a modulation at QOP which is exactly or nearly the same as T (if known already). The total modulation clearly depends on several factors, such as, $M_\bullet$, $M_\star$, size of the companion, mass loss due to winds, probable eclipsing or reflection by the atmosphere of winds from the companion, superhumping, etc. Any of these may not be known with certainty because of a little theoretical progress in these directions. However, the modulation due to tidal force variation can be quantified by the RMS power of the peak in the Fourier spectra (i.e. power density spectra, PDS). But, the large Keplerian disk of a LMXRB and the small disk of a HMXRB must influence such a modulation differently because the flow is highly viscous in the former while almost inviscid stellar winds predominantly control the overall accretion flow in the latter. So, the RMS value will be affected (Ghosh & Chakrabarti 2016). We produce Fourier spectra of long-term lightcurves via PDS and LSPs that the modulation at QOPs is real.

4.2 Long-term Observation of 6 XRBs by *Swift*/BAT

In order to see the difference of behaviour in the the tidal modulation of photon flux at the QOP due to the nature of overall accretion in two basic categories of XRBs, we consider two persistent HMXRBs, viz. Cyg X-1 & Cyg X-3, and four LMXRBs, viz. XTE J1650-500, H 1705-25, 1E 1740.7-2942 & GRS 1758-258. The last two sources are persistent LMXRBs. All six sources are either known to be non-eclipsing or partially eclipsing (Cyg X-3) or else, the inclination angles in them are not low. Therefore, we can rule out the possibility of a modulation due to eclipsing effects. Some of their orbital parameters known from available reports in the literature are

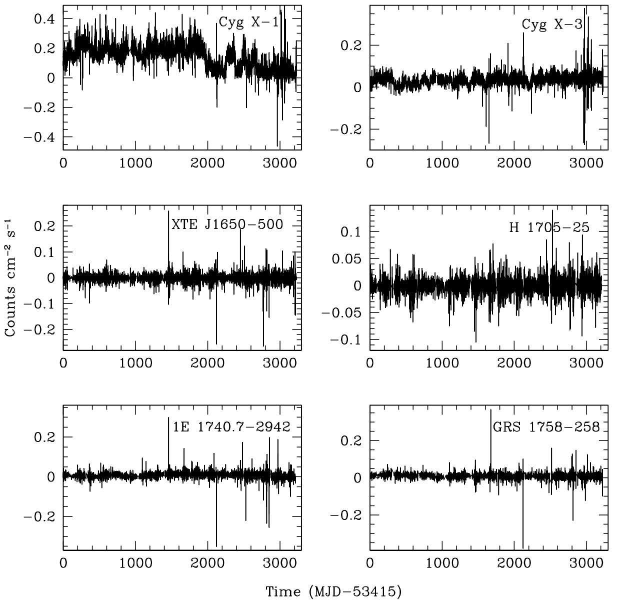

Figure 4.1: *Swift*/BAT ($15 - 50$ *keV*) orbital lightcurves of six XRBs under consideration are drawn. Due to background subtraction effects, count rates are negative almost regularly. However, we have not used these data directly. A crude *out-layer detection* method is utilized to obtain modified lightcurves, where a *robust scaling* is followed by subtracting the running average (dynamic mean) from the actual data shown here (Ghosh & Chakrabarti 2016).

given in Table 4.1 with references. Almost all of the observational results mentioned before are based on RXTE/ASM data, i.e. in the low energy range ($1.5 - 12$ *keV*). Therefore, we use long-term (> 8 *yr* since MJD 53415) orbital lightcurves of *Swift*/BAT data in order to find the features of our interest in its high energy range of $15 - 50$ *keV*. The large area of the detector in Swift/BAT is an added advantage in giving rise to more reliable results in our context.

Figure 4.1 shows *Swift*/BAT $15 - 50$ *keV* orbital lightcurves for $> 3000d$ of six XRBs under consideration. Due to background subtraction effects, count rates are negative almost regularly. However, we do not use these data directly. A crude *out-layer detection* method is incorporated to modify the actual data via a *robust scaling* in which the fluctuations around the dynamic mean data are taken into account. These reduced data are interpolated at $0.05d$ interval. Figure 4.2 shows the PDS extracted from the modified lightcurves. The QOP timescale is written in each box from the standard Lorentzian fitting of the peak appeared in each spectrum. The bumps at $\sim 10^{-6} Hz$ in the PDS of Cyg X-1, 1E 1740.7-2942 & GRS 1758-258, and at $\sim 10^{-5} Hz$ in the PDS of Cyg X-3, XTE J1650-500 & H 1705-25 are due to the adopted data reduction procedure followed by the removal of low-frequency noise while producing the PDS. The peaks are fitted with the Lorentzian model. The prominent peak of Cyg X-3 is not due to its partial eclipse since eclipsing is significant only in a low energy level, and not in *Swift*/BAT high energy range. All the results obtained from the PDS are summarized in Table 4.2.

4.2.1 Estimation of unknown QOPs

The periodicities of two persistent LMXRBs, viz. GRS 1758-258 and 1E 1740.7-2942, are not yet known correctly. Reported numbers of $T < 1d$ in both are given in Table 4.1. On the other

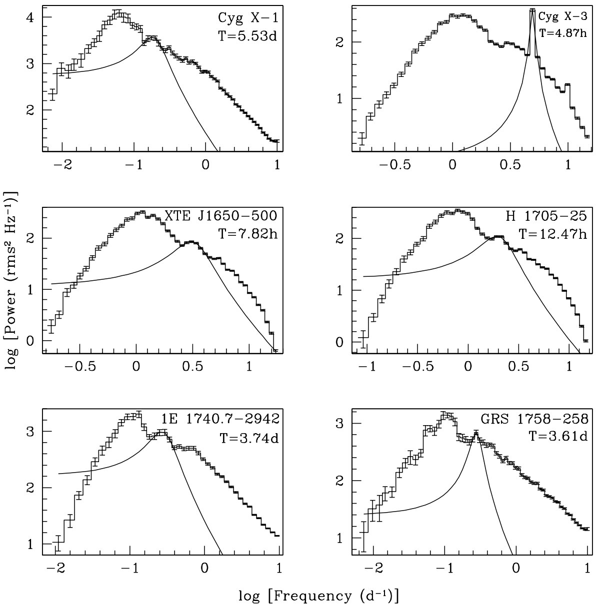

Figure 4.2: PDS of the modified lightcurves extracted from the actual lightcurves of Fig. 4.1. The QOPs are marked in the boxes. The Lorentzian model is used to fit the peaks. The bumps at $\sim 10^{-6} Hz$ in the PDS of Cyg X-1, 1E 1740.7-2942 & GRS 1758-258, and at $\sim 10^{-5} Hz$ in the PDS of Cyg X-3, XTE J1650-500 & H 1705-25 have arisen due to the data reduction procedure adopted and also for the removal of low-frequency noise from the PDS (Ghosh & Chakrabarti 2016).

hand, Smith et al. (2002b) found several days to a few weeks for the same. However, the QOPs in these two sources are around $3d - 4d$ as seen in our analysis. However, one estimate can be a super-orbital period of the other. Nevertheless, if the period of a binary system with an elliptical orbit is not known otherwise, that can be predicted, with reasonable accuracy for a HMXRB while with lesser rigor for a LMXRB, by our simple method as a spin-off.

4.2.2 Influence of Accretion Disk Size: Viscous Smearing

RMS power of the peak, which is fitted with the standard Lorentzian model, directly follows from the area of the peak above the background curve in the spectrum. The RMS-values (in %) along with the statistical significance (in units of standard deviation σ of Gaussian distribution) are given in Table 4.2. For HMXRBs, viz. Cyg X-1 and Cyg X-3, the RMS values are found to be 6.72% and 5.30% respectively. However, for the rest four sources (LMXRBs), these are approximately constrained within a range of $2\% - 4\%$.

Since the RMS power of such a peak is a measure of its strength, our results imply that a lack of viscosity in the predominant wind accretion and small Keplerian disks (even with reasonable viscosity) in both Cygnus sources leave the modulations at their QOPs to be carried almost intact toward the inner region. On the other hand, stronger viscous processes of the large disks in LMXRBs will smear out the periodic modulation to a great level and weaken the peak strength or RMS power. We have seen in §3.4 that the long time lags in 1E 1740.7-2942 and GRS 1758-258 of about $25d$ and $60d$ respectively (Smith, Heindl & Swank 2002a) should indicate large disks, and in particular, a larger disk in the latter. The RMS-values in these two LMXRBs are found to be respectively about 4% and 2.5% (from Table 4.2) from

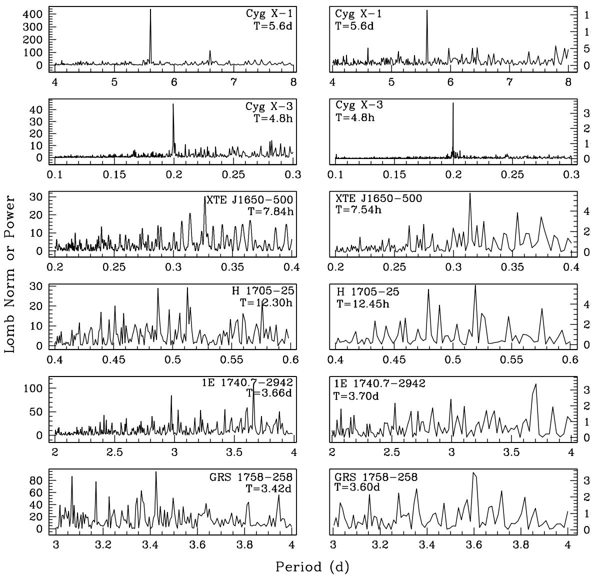

Figure 4.3: *(Left)* LSPs extracted from RXTE/ASM ($1.5-12$ keV) long-term ($5000d$ since MJD 50450) modified data are shown. *(Right)* *Swift*/BAT ($15-50$ keV) modified data result in these LSPs. QOPs are marked in the boxes. Sharp peaks in Cyg X-1 & Cyg X-3 indicate strong orbital modulations escaping viscous effects. Noisy peaks in 4 LMXRBs are imprints of viscous smearing (Ghosh & Chakrabarti 2016).

our present analysis. Compared to 1E 1740.7-2942, lower RMS in GRS 1758-258 indicates a stronger viscous smearing, which is very much consistent with its larger disk. Therefore, an inverse proportionality relation exists between the RMS power and the disk size.

Table 4.2: Estimates on QOPs in LSPs and PDS (Ghosh & Chakrabarti 2016)

X-Ray Binary (BH)	T(LSP) (RXTE)	T(LSP) (*Swift*)	T(PDS) (*Swift*)	RMS (%)	Stat. Sig.
Cyg X-1	$5.60d$	$5.60d$	$5.53^{+0.70}_{-0.56}d$	6.72	3.3σ
Cyg X-3	$4.80h$	$4.80h$	$4.87^{+0.23}_{-0.21}h$	5.30	1.6σ
H 1705-25	$12.30h$	$12.45h$	$12.47^{+1.09}_{-0.92}h$	3.15	1.6σ
XTE J1650-500	$7.84h$	$7.54h$	$7.82^{+0.83}_{-0.68}h$	3.21	2.6σ
GRS 1758-258	$3.42d$	$3.60d$	$3.61^{+0.21}_{-0.19}d$	2.49	2.0σ
1E 1740.7-2942	$3.66d$	$3.69d$	$3.74^{+0.72}_{-0.52}d$	4.10	1.3σ

4.3 Periodograms with RXTE/ASM and *Swift*/BAT data

In order to have an additional check on the QOPs, we have computed LSPs for all six XRBs. In addition to the modified lightcurves of Swift/BAT ($15-50$ keV), similarly modified lightcurves obtained from RXTE/ASM ($1.5-12$ keV) sum-band data for about $5000d$ (since MJD 50450) are used. Figure 4.3 shows these LSPs drawn on the left column for RXTE/ASM data and on the right column for Swift/BAT data. Though several distinct peaks are seen in many of them, we see evidence of periodicities having values similar to what we obtained through PDS with Swift data. The periods marked in each box are obtained from the strongest peaks. Interestingly, the periods obtained from both RXTE and Swift data are in the same ball-park.

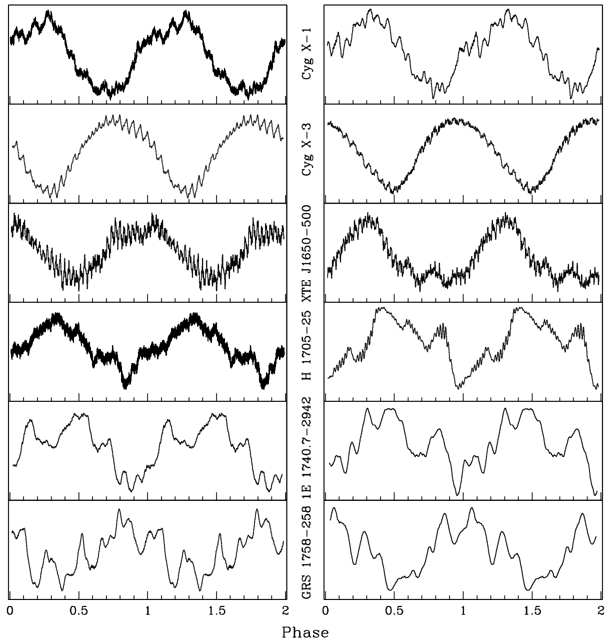

Figure 4.4: Phase diagrams corresponding to the QOPs marked in the LSPs of Fig. 4.3 with (left) RXTE/ASM and (right) *Swift*/BAT data. Vertical axis is not labelled due to its irrelevance through arbitrary scaling procedure adopted. As expected from their sharp peaks in Fig. 4.3, phase curves of Cygnus systems are more regular than the rest. Moreover, Cyg X-3 shows almost ideal sinusoidal phase curves having uniform wiggles which could hint at the spin of the companion.

Distinct and sharp peaks at $\sim 5.6\ d$ and $\sim 4.8\ h$ observed for Cyg X-1 and Cyg X-3, respectively, are also a testimony of very small Keplerian disks in them. General sinusoidal behaviour in phase diagrams corresponding to the QOPs marked in the LSPs of Fig. 4.3 is depicted in Fig. 4.4. The left column represents RXTE/ASM data and the right column is for *Swift*/BAT data. Sinusoidal peaks appear at slightly different phases in some of the cases, possibly because there are energy dependent factors (e.g. X-ray eclipsing, scattering) present apart from the tidal effects. The possible presence of superhumps with a slightly different period may have caused the more complex phase diagrams in the lower three panels.

Chapter 5

Summary

Spectral properties of all types of XRBs cannot be properly understood unless those are studied for a long period of time ($\sim$ few years to decades) in a proper manner, instead of fitting short-term data chunks ($\mathscr{O}[1000s]$) of different satellites at irregular intervals with various models and arranging them on a truncated time line for an incomplete timing analysis. However, as RXTE/ASM recorded X-ray data ($1.5 - 12\ keV$) continuously for a long time till 2013 with reasonably good time bin ($\sim 1h$) and time resolution ($125\mu s$), a careful usage of RXTE/ASM data has been proved to be most suitable for the purpose and our attempts have become fruitful in extracting many new exciting results (Ghosh & Chakrabarti 2016, 2018, 2019; GBC19) discussed in the Thesis.

We have used mainly the tri-band ($1.5 - 3$, $3 - 5$ & $5 - 12$ keV) X-ray data and defined a *dynamic photon index* (DPI, designated by Θ) in its upper two bands (i.e. between $3 - 12\ keV$) in order to study all types of XRBs systematically for a long time (Ghosh & Chakrabarti 2018, 2019). The DPI maps the usual power law photon index (Γ) on a linear scale of hard energy spectrum. Spectral state transition is determined by the threshold at $\Gamma \sim 2$, below which the HS and above which the SS are observed. On the other hand, this spectral threshold is replaced by $\Theta \sim 0$, above which the HS and below which the intermediate states and the SS prevail. Furthermore, it *alone* carries all the information supplied by the Comptonizing efficiency (CE), the hardness ratios (HRs) and Γ at one go. But, the most important property of the DPI is its limited range of values within $\pm\frac{\pi}{2} = \pm 1.57$ arisen from its definition. This gives rise to a *universality* such that all XRBs can be accomodated and compared with one another within its common quantitative domain with qualitative implications. It must be noted that once an XRB is studied with the DPI, a resulting observation will not retain any trace of the RXTE/ASM data. Thus, the DPI appears to be generic as it has advantageous symmetric limits unlike HR1 or HR2 (having limits arbitrarily far away from their axes). Furthermore, one can define such an index in connection with other satellites (e.g. XMM-Newton) which record soft (black body) and hard (Comptonized or power law) photons simultaneously and the new procedures of timing analysis (Chapter 2) employed by us can also be undertaken for some other goals of study. In particular, if an outburst sets in today, its possible fate can be predicted in terms of its duration, spectral evolution, disk hysteresis, etc. with any satellite data (1–18 keV, say) of only the next couple of weeks.

The methods of analysis have revolved around RXTE/ASM data with soft ($1.5-3$ keV) and hard ($3-12$ keV) photons while our findings are interpreted quite easily by the TCAF paradigm. The spectral and timing properties due to the accretion in all types of XRBs cannot be explained universally without an addition of a more generic and nearly inviscid sub-Keplerian advective flow having low angular momentum to the standard Keplerian disk component carrying high viscosity and high angular momentum (Chakarabarti 1995; CT95). In addition, a hot electron component is also required (Zdziarski 1988; Haardt et al. 1994; Zhang et al. 2009) in order to account for the hard Comptonized photons. In TCAF solution (Chakrabarti 1995; CT95), this hot component is created by the radiatively inefficient sub-Keplerian flow. It slows down close to the black hole due to the centrifugal force and puffs up by resulting heat. This so-called CENtrifugal pressure supported BOundary Layer, or CENBOL, behaves as the Compton cloud and reprocesses low energy (soft) photons into high energy (hard) photons. General success of such model indicates that the Compton cloud is also produced by the companion and understanding of hard X-rays do not require any external source of electrons. However, the sub-Keplerian flow, arising out of companion winds, is also expected to be modulated and this flow would arrive in almost free-fall time scale if viscosity is low enough so that it does not become a Keplerian disk. However, as CT95 and Chakrabarti (1997) found, that would only modulate the optical depth of the ‘Compton cloud’ and change spectral slopes without changing the photon flux significantly. Our detailed analysis of actual satellite data reveals that there is a distinct time lag between the DPI and the photon fluxes in LMXRBs, which accrete predominantly through the Roche Lobe overflow, while HMXRBs, which accrete primarily winds of the companion, do not show such a lag.

In Chapter 3, we have studied several transient LMXRBs, viz. GX 339-4, H 1743-322, XTE J1550-564, XTE J1650-500, GRO J1655-40 & 4U 1543-47 exhibiting either frequent outbursts (in the former two) or sporadic outbursts (in the latter ones) and observed that they indeed possess two radiative components (soft & hard), which are separated by a timescale (relative arrival time delay, $\tau_r = t_{soft} - t_{hard}$ via Θ), and *also temporally* for long, mimic both multicolour blackbody distribution and power law emission tail originated respectively from the Keplerian disk flow and the sub-Keplerian halo flow obeying the TCAF solution. These two flows are connected in a nonlinear way since the power law photon flux is a result of the degree of intercepted soft photons as well as its optical depth determined by the varying properties of the Compton cloud (Chakrabarti 1997). Our findings using observational data (Ghosh & Chakrabarti 2018, 2019; GBC19) have directly established the veracity of the TCAF paradigm in the first place by a systematic usage of continuous X-ray data. The DPI appears as a typical well-like curve during the course of an outburst and it scans the outburst at all instants indicating all stages of spectral transition. Moreover, only with the single parameter Θ in hand, a generic investigation of eighteen outbursts in the aforesaid six transient low-mass XRBs (LMXRBs) has shown that all types of outbursts can be divided into two basic classes: normal (i.e. canonical) and anomalous. The normal outbursts (OBs) are further grouped into two categories: OB-I ($\tau_r \sim 0d$) & OB-II ($\tau_r \gg 0d$), based on several distinct features of difference in spectral transition properties and temporal evolution of accretion flow, in terms of the lag in two different timescales attributed to two flow components ($\tau = t_{disk} - t_{halo} \sim \tau_r \geq 0$), the dependence of outburst duration on τ, the disk size, the Compton cloud size, and the hysteresis property, etc. We have first computed those time lags by the DPI and estimated the lengthscales of the disks assuming a proportionality between them. Then we have shown how the size and the formation of the disks determine both spectral and temporal properties of different outbursts.

The lengthscale of the Keplerian flow or the size of the disk is determined by the stretch between the CENBOL (at $r_{in} > 3\ r_g$) and the *accumulation radius*, $\mathscr{O}[100\ r_g] > X_a > r_{in}$, where Keplerian matter is piled up due to a lack of viscosity in pre-outburst quiescent phase because of a thermal-viscous instability before being ushered in during outbursts by viscosity higher than its critical value (Chakrabarti 1990, 1996). However, X_a may be different for each outburst (CDN19; Ghosh & Chakrabarti 2018, 2019; GBC19). As the accumulation radius may be different in different outbursts in the same LMXRB, the time lags are also variable giving rise to varying disks for the same source. In a given outburst of a LMXRB, if the disk is large, at the end of the peak outburst, the disk culminates in HIMS before the HS is achieved. In smaller disks, the disk quite possibly gets accreted as soon as the peak outburst is over, and the HS may occur directly. Different outbursts have different disk sizes for LMXRBs mainly because the outer edge of the disk depends on the leftover viscosity after the previous event. Thus a LMXRB may have smaller disks in some outbursts. In addition, we have shown how and why the successive outbursts of H 1743-322 are different from those in GX 339-4 (Ghosh 2018; Ghosh & Chakrabarti 2018, 2019). In particular, we have identified several anomalous outbursts carrying both disintegrating and waxing disks in the former while normal outbursts are observed in the latter object.

But in an HMXRB, there is no Keplerian disk from the outer edge since the injected matter is sub-Keplerian. So the time lags are expected to be always short or negligible. We have shown in §3.4 how a Keplerian flow appears to be decipherable in the standard HMXRB, Cyg X-1, using its data for a long time ($\sim 13\ yr$) by the same yardstick, DPI (Θ) (Ghosh & Chakrabarti 2018). However, the responses of soft and hard photon fluxes are instantaneous with $\tau_r = 0d \pm 2.4h$ not only in the entire time span but also discretely in its six flaring phases resembling OB-I type outbursts. These show negligible hysteresis of a very small disk formed close to the black hole, when estimated by DPI. When GBC19 used the ($2.5 - 25$ keV) RXTE/PCA long-term ($\sim 530d$) spectral data chunks comprising the two most important flares picked out from those six and extracted two mass accretion rates with continuous TCAF-fitting of the spectra in order to find τ directly. They obtained $\tau = 0d^{+4.42}_{-1.43}h = \tau_r$. Both findings imply that a small Keplerian disk very close to the black hole in Cyg X-1 is formed due to a slow redistribution of the low angular momentum of its stellar wind, giving rise to sporadic soft or intermediate spectral states in the form of irregular flares. These results also corroborate simultaneously, with a greater rigour, earlier findings (Smith, Heindl & Swank 2002a) obtained from long-term ($\sim 5\ yr$) RXTE/ASM and RXTE/PCA data.

Therefore, the long-term timing analysis of RXTE/ASM data with the DPI (Ghosh & Chakrabarti 2018, 2019) has pioneered a new outlook towards understanding XRBs quite accurately. A similar treatment with the well-known class-variable source (LMXRB), GRS 1915+105, has resulted in similar conclusion (Ghosh & Chakrabarti 2018) which actually explains its similarity with Cyg X-1 as found by Reig, Papadakis & Kylafis (2002). However, another HMXRB, Cyg X-3, has been observed to behave quite differently, despite its partial resemblance with Cyg X-1 in terms of otherwise segregated flow components of radiation with respect to DPI. The response of Θ with the two fluxes is very weak showing an asymmetric correlation profile (Ghosh 2018) contrary to the symmetric one seen in Cyg X-1. However, like Cyg X-1, $\tau_r = 0d \pm 2.4h$ is also observed in Cyg X-3 indicating a weak but well-tuned and complex accretion disk. We have concluded, in general, that LMXRBs indeed have larger accretion disks than those in HMXRBs and their observational properties are dictated by the Keplerian disk properties. Sometimes, LMXRBs form small disks which may be compared with that formed in a HMXRB.

In accreting XRBs, X-ray flux modulations in orbital scales are common phenomena. So far, these orbital modulations are attributed to eclipsing effects, effects from wind reflections and sumperhumping. From an well-established theoretical argument of dependence of tidal effects on eccentricity we have proposed that the mass transfer and the orbital modulation would also be affected for those binaries which have non-zero eccentricity. Smaller distance during a periastron passage would enhance mass accretion rates and larger distance during an apastron passage would reduce it. Stellar companion of a black hole orbiting in an eccentric orbit will experience modulating tidal force with a periodicity same as that of the orbital period. This would modulate accretion rates and thus the seed photon flux which are inverse Comptonized to produce harder X-rays are expected to be modulated. In Chapter 4, we have incorporated this issue by analyzing Swift/BAT ($15 - 50\ keV$) data and RXTE/ASM ($1.5 - 12\ keV$) sum-band data. We have found this periodicity from the peaks appeared in Fourier spectra of the modified lightcurves for six XRBs. Large Keplerian disks formed in LMXRBs give rise to viscous smearing over such orbital modulations and, consequently, the Lorentzian peaks in power density spectra at the orbital periods are weak and result in lower RMS value. On the contrary, in HMXRBs like the Cygnus systems, small Keplerian disks, in dearth of significant viscosity, spare the orbital modulations of the outer edge to be evident even at the inner edge. As a consequence, peaks with higher RMS value are observed.

Throughout the Thesis, our generalized methods of analysis have consistently produced interesting results in all types of XRBs with BHs.

References

[1] Bradt H. 2008, Astrophysical Processes, 1st edn. Cambridge University Press, Cambridge

[2] Belloni T., Klein-Wolt M., Mendez M. et al., 2000, A&A, 355, 271

[3] Bondi H. 1952, MNRAS, 112, 195

[4] Boroson B. & Vrtilek S. D. 2010, ApJ, 710, 197

[5] Boyd P. T., Smale A. P., Dolan J. F. 2001, ApJ, 555, 822

[6] Brocksopp C., Fender R.P., Larionov V., et al. 1999, MNRAS, 309, 1063

[7] Brocksopp C., Tarasov A. E., Lyuty V. M., Roche P. 1999, A&A, 343, 861

[8] Capitanio F., Belloni T., Del Santo M., & Ubertini P. 2009, MNRAS, 398, 1194

[9] Castro-Tirado A. J., Alberto J., Brandt S., et al. 1994, ApJS, 92, 469

[10] Chakrabarti S. K. 1989, ApJ, 347, 365

[11] Chakrabarti S. K. 1990, MNRAS, 243, 610

[12] Chakrabarti S. K. 1995, in Bohringer H., Morfil G. E., Trumper J., eds., Seventeenth Texas Symposium on Relativistic Astrophysics and Cosmology, Vol. 759, p. 546, New York Academy of Sciences, New York

[13] Chakrabarti S. K. 1996, ApJ, 464, 664

[14] Chakrabarti S. K. 1997, ApJ, 484, 313

[15] Chakrabarti S. K., Debnath D., Nagarkoti S. 2019, ASR, 63, 3749 (CDN19)

[16] Chakrabarti S. K. & Manickam S. G. 2000, ApJ, 531, L41

[17] Chakrabarti S. K. & Titarchuk L. G. 1995, ApJ, 455, 623 (CT95)

[18] Chen W., Gehrels N., Leventhal M. 1994, ApJ, 426, 586

[19] Davidsen A. & Ostriker J. P. 1974, ApJ, 189, 331

[20] Debnath D., Chakrabarti S. K., Mondal S. 2014, MNRAS, 440, L121

[21] Debnath D., Mondal S., Chakrabarti S. K. 2015, MNRAS, 447, 1984

[22] Frank J., King A., Raine D. 2002, Accretion Power in Astrophysics, Cambridge University Press, New York

[23] Ghosh A. 2018, in Mukhopadhyay B. & Sasmal S., eds., Exploring the Universe: From Near Space to Extra-Galactic. Astrophysics and Space Science Proceedings, Vol. 53, p. 311, Springer, Cham, Switzerland

[24] Ghosh A. & Chakrabarti S. K. 2016, Ap&SS, 361:310

[25] Ghosh A. & Chakrabarti S. K. 2018, MNRAS, 479, 1210

[26] Ghosh A. & Chakrabarti S. K. 2019, MNRAS, 485, 4045

[27] Ghosh A., Banerjee I., Chakrabarti S. K. 2019, MNRAS, 484, 5802 (GBC19)

[28] Giri K. & Chakrabarti S. K. 2013, MNRAS, 430, 2836

[29] Greiner J., Morgan, E. H., Remillard, R. A. 1996, ApJ, 473, 107

[30] Grinberg V., Leutenegger M. A., Hell N., et al. 2015, A&A, 576, A117

[31] Haardt F. & Maraschi L. 1993, ApJ, 413, 507

[32] Haardt F., Maraschi L., Ghisellini G. 1994, ApJ, 432, L95

[33] Harlaftis E. T. & Greiner J. 2004, A&A, 414, 13

[34] Hjalmarsdotter L., Zdziarski A. A., Larsson S., Beckmann V., McCollough M., Hannikainen D. C., Vilhu O. 2008, MNRAS, 384, 278

[35] Jana A., Debnath D., Chakrabarti S. K., Mondal S., Molla A. A. 2016, ApJ, 819, 107

[36] Johannsen T., Psaltis D., McClintock J. E. 2009, ApJ, 691, 997

[37] Koljonen K. I. I. & Maccarone T. 2017, MNRAS, 472, 2181

[38] Kudryavtsev M. I., Svertilov S. I., Bogomolov V. V. 2004, astro-ph/0404188

[39] Kuznetsov S. I., Gilfanov M. R., Churazov E. M. et al. 1999, Astron. Lett. 25, 351

[40] Martin A. C., Casares J., Charles P. A., van der Hooft F., van Paradijs J. 1995, MNRAS, 274, L46

[41] Meyer F. & Meyer-Hofmeister E. 1994, A&A, 288, 175

[42] Meyer F., Liu B. F., Meyer-Hofmeister E. 2000, A&A, 354, L67

[43] Mineshige S. 1996, PASJ, 48, 93

[44] Mondal S., Chakrabarti S. K., Nagarkoti S., Arévalo P. 2017, ApJ, 850, 47

[45] Mondal S., Debnath D., Chakrabarti S. K. 2014, ApJ, 786, 4

[46] Molla A. A., Chakrabarti S. K., Debnath D., Mondal S. 2017, ApJ, 834, 88

[47] Molla A. A., Debnath D., Chakrabarti S. K., Mondal S., Jana A. 2016, MNRAS, 460, 3163

[48] Morgan E. H., Remillard R. A., Greiner J. 1997, ApJ, 482, 993

[49] Naik S., Rao A. R., Chakrabarti S. K. 2002, JApA, 23, 213

[50] Narayan R. & Yi I. 1994, ApJ, 428, 13

[51] Obst M., Pottschmidt K., Lohfink A. et al. 2013, AAS HEAD meeting, vol. 13, p. 126.54

[52] Orosz J. A. & Baily C. D. 1997, ApJ, 477, 876

[53] Orosz J. A., McClintock J. E., Remillard R. A., Corbel S. 2004, ApJ, 616, 376

[54] Orosz J. A., McClintock J. E., Aufdenberg J. P. et al. 2011, ApJ, 742:84, 1

[55] Paczyński B. & Wiita P. J. 1980, A&A, 88, 23

[56] Pal P. S. & Chakrabarti S. K. 2015, ASR, 56, 1784

[57] Pal P. S., Chakrabarti S. K., Nandi, A. 2013, ASR, 52, 740

[58] Patterson J., Kemp J., Harvey D. A. et al. 2005, Publ. Astron. Soc. Pac. 117, 1204

[59] Poutanen J., Veledina A., Zdziarski A. A. 2018, A&A, 614, A79

[60] Rao A. R., Naik S., Vadawale S. V., Chakrabarti S. K. 2000, A&A, 360, L25

[61] Reig P., Papadakis I., Kylafis N. D. 2002, A&A, 383, 202

[62] Roy A. & Chakrabarti S. K. 2017, MNRAS, 472, 4689

[63] Shakura N. I. & Sunyaev R. A. 1973, A& A, 24, 337

[64] Shaposhnikov N. & Titarchuk L. G. 2009, ApJ, 699, 453

[65] Smith D. M., Heindl W. A., Swank J. H. 2002a, ApJ, 569, 362

[66] Smith D. M., Heindl W. A., Swank J. H. 2002b, ApJ, 578, L129

[67] Sunyaev R. A. & Titarchuk L. G. 1980, A&A, 86, 121

[68] Sunyaev R. A. & Titarchuk L. G. 1985, A&A, 143, 374

[69] Taam R. E., Liu B. F., Meyer F., Meyer-Hofmeister E. 2008, ApJ, 688, 527

[70] Wen L., Cui W., Levine A. M., Bradt H. V. 1999, ApJ, 525, 968

[71] Wen L., Levine A. M., Corbet R. H. D., Bradt H. V. 2006, A&A Suppl. Ser. 163, 372

[72] Zdziarski A. A. 1988, MNRAS, 233, 739

[73] Zdziarski A. A., Mikołajewska J., Belczyński K. 2013, MNRAS, 429, L104

[74] Zhang S., Chen Y. P., Wang J. M., Torres D. F. & Li T. P. 2009, A&A, 502, 231

[75] Zhou J. N., Liu Q. Z., Chen Y. P., Li J., Qu J. L., Zhang S., Gao H. Q., Zhang Z. 2013, MNRAS, 431, 2285